

SMC Bulletin

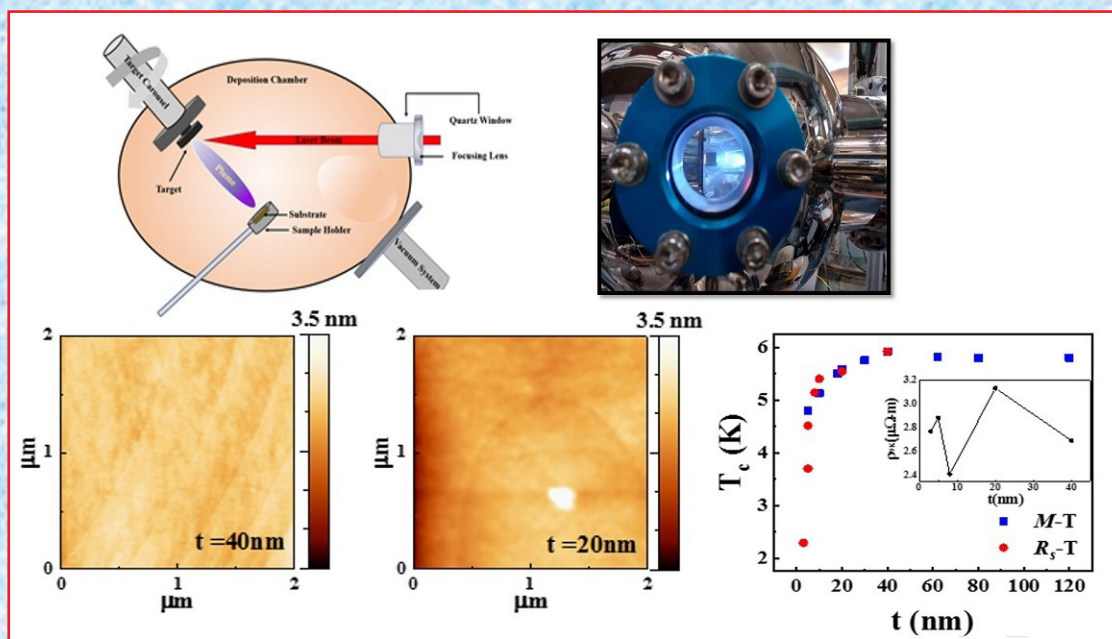
ISSN 2394-5087

A Publication of the Society for Materials Chemistry

Volume 11

No. 3

December 2020



Special Issue on
Thin Films: Growth, Properties and Applications



Society for Materials Chemistry

Society for Materials Chemistry was mooted in 2007 with following aims and objectives:

- (a) to help the advancement, dissemination and application of the knowledge in the field of materials chemistry,
- (b) to promote active interaction among all material scientists, bodies, institutions and industries interested in achieving the advancement, dissemination and application of the knowledge of materials chemistry,
- (c) to disseminate information in the field of materials chemistry by publication of bulletins, reports, newsletters, journals.
- (d) to provide a common platform to young researchers and active scientists by arranging seminars, lectures, workshops, conferences on current research topics in the area of materials chemistry,
- (e) to provide financial and other assistance to needy deserving researchers for participation to present their work in symposia, conference, etc.
- (f) to provide an incentive by way of cash awards to researchers for best thesis, best paper published in journal/national/international conferences for the advancement of materials chemistry,
- (g) to undertake and execute all other acts as mentioned in the constitution of SMC.

Executive Committee

President

Dr. V. K. Jain

UM-DAE Centre for Excellence in Basic Sciences, University of Mumbai, Kalina Campus, Mumbai-400098
jainvk@cbs.ac.in

Vice-Presidents

Dr. A. K. Tyagi

Bhabha Atomic Research Centre Trombay, Mumbai, 400 085
aktyagi@barc.gov.in

Prof. G. Mugesh

Indian Institute of Science Bangalore - 560 012
mugesh@iisc.ac.in

Secretary

Dr. R. K. Vatsa

Bhabha Atomic Research Centre Trombay, Mumbai, 400 085
rkvatsa@barc.gov.in

Treasurer

Shri R. K. Mishra

Bhabha Atomic Research Centre Trombay, Mumbai, 400 085
rkmishra@barc.gov.in

Dr. S. Kannan

Bhabha Atomic Research Centre Trombay, Mumbai-400085

Prof. Sri Sivakumar

Indian Institute of Technology Kanpur, 208016

Dr. Rajesh Ganeshan

Indira Gandhi Centre for Atomic Research Kalpakkam,, 603102

Dr. Ranjan Mittal

Bhabha Atomic Research Centre Trombay, Mumbai-400085

Dr. Neeraj Agarwal

UM-DAE Centre for Excellence in Basic Sciences, University of Mumbai, Kalina Campus, Mumbai-400098

Dr. (Smt.) Aparna A. Banerjee

Bhabha Atomic Research Centre Trombay, Mumbai-400085

Dr. (Smt.) Vinita Grover Gupta

Bhabha Atomic Research Centre Trombay, Mumbai-400085

Shri. R. Manimaran

Bhabha Atomic Research Centre Trombay, Mumbai-400085

Dr. Deepak Tyagi

Bhabha Atomic Research Centre Trombay, Mumbai-400085

Dr. (Smt.) Daisy Joseph

Bhabha Atomic Research Centre Trombay, Mumbai-400085

Co-opted Members

Dr. P. A. Hassan

Bhabha Atomic Research Centre Trombay, Mumbai, 400 085

Dr. Sandeep Nigam

Bhabha Atomic Research Centre Trombay, Mumbai, 400 085

Dr. V. Sudarsan

Bhabha Atomic Research Centre Trombay, Mumbai-400085

Contact address

Society for Materials Chemistry

C/o Chemistry Division

Bhabha Atomic Research Centre, Trombay, Mumbai, 400 085, India

Tel: +91-22-25592001, E-mail: socmatchem@gmail.com

SMC Bulletin

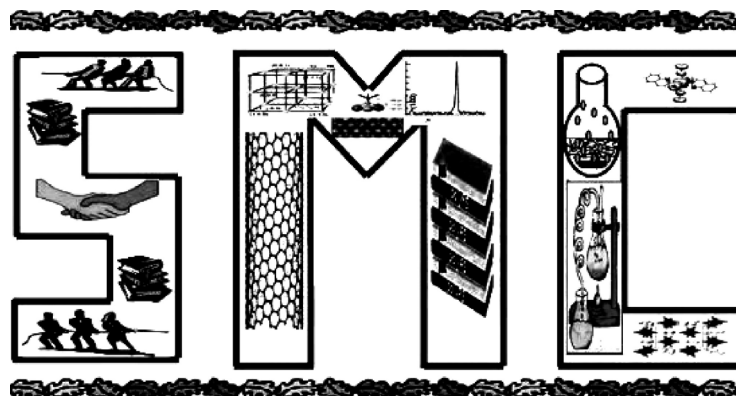
A Publication of the Society for Materials Chemistry

Volume 11

No. 3

December 2020

Special Issue on
Thin Films: Growth, Properties and Applications



SOCIETY FOR MATERIALS CHEMISTRY

SMC Bulletin

Vol. 11

No. 3

December 2020

Guest Editor

Dr. Sangita Bose

School of Physical Sciences
UM-DAE Centre for Excellence in Basic Sciences
University of Mumbai, Kalina Campus
Santacruz (E), Mumbai-400098
e-mail: sangita@cbs.ac.in

Editorial Board

Dr. Arvind Kumar Tripathi Chemistry Division Bhabha Atomic Research Centre Trombay, Mumbai, 400 085 e-mail: catal@barc.gov.in	
Dr. Manidipa Basu Chemistry Division Bhabha Atomic Research Centre Trombay, Mumbai, 400 085 e-mail: deepa@barc.gov.in	Dr. Rajesh Ganesan Materials Chemistry Division Indira Gandhi Centre for Atomic Research Kalpakkam, 603102 e-mail: rajesh@igcar.gov.in
Dr. G. Kedarnath Chemistry Division Bhabha Atomic Research Centre Trombay, Mumbai, 400 085 e-mail: deepa@barc.gov.in	Dr. Sandeep Nigam Chemistry Division Bhabha Atomic Research Centre Trombay, Mumbai, 400 085 e-mail: snigam@barc.gov.in
Dr. Rajesh V. Pai Fuel Chemistry Division Bhabha Atomic Research Centre Trombay, Mumbai, 400 085 e-mail: rajeshvp@barc.gov.in	Dr. Vivek Polshettiwar Department of Chemical Sciences, Tata Institute of Fundamental Research, Colaba, Mumbai 400005 e-mail: vivekpol@tifr.res.in

Published by

Society for Materials Chemistry
C/o. Chemistry Division
Bhabha Atomic Research Centre, Trombay, Mumbai, 400 085
E-mail: socmatchem@gmail.com,
Tel: +91-22-25592001

Please note that the authors of the paper are alone responsible for the technical contents of papers and references cited therein. Front cover shows topography and variation of T_c as a function of thickness of α -Re,Zr superconducting thin films (bottom) deposited using a Pulsed laser deposition system (top).

Guest Editorial



Dr. Sangita Bose

Thin films have found numerous applications in our everyday lives as protecting or passivating layers, catalysts, sensors, micro-electronic, opto-electronic and energy harvesting devices, etc. Most of these applications are driven by the exciting properties which emerge due to the dimensional constraints in thin films. Thin film technology is thus based on developing new methods of their growth and fabrication, careful characterization of their structural, morphological, chemical and physical properties and finally developing methods to integrate them into devices for applications. In the past couple of decades with the development of new technologies, it has not only been possible to push the boundaries with respect to thin film growth it has also been possible to measure the properties of extremely thin films down to even a monolayer which has led to many exciting novel properties.

In this special issue on thin films, we bring together articles covering the areas of growth, properties and applications of thin films. There are articles which discuss the recent advancements in the emerging properties of thin films along with their novel methods of growth which range from graphene thin films, superconducting thin films and nano-crystalline diamond thin films. In addition, applications based on carbon based thin films as corrosion resistant coatings and as field effect transistors have also been reviewed.

It has been my great pleasure to act as a guest editor for this special issue on "Thin Films: Growth, Properties and Applications". My sincere thanks to Dr. V. K. Jain, President, SMC and all executive committee members for giving me this opportunity. I also thank all the authors for their contribution to the current issue of the bulletin. We hope the readers enjoy reading the articles in this issue and find them informative.

From the desks of the President and Secretary



Dr. V. K. Jain
President



Dr. R. K. Vatsa
Hon. Secretary

Dear Esteemed SMC Members and colleagues,

Very warm greetings from the Executive Council of the Society for Materials Chemistry (SMC)!

It has been a strong and consistent endeavor of the editorial team of the SMC bulletin to bring to you thematic issues based on current research areas which have contemporary interest for the wider scientific community. The topics for the past few thematic issues have been multidisciplinary thereby bridging the gap between the disciplines of chemistry, physics, biology, and engineering. This issue of the SMC bulletin is also in the same direction and is based on “Thin Films: Growth, Properties and Applications”.

The articles in this issue deal with different aspects of thin films - from growth to some of their interesting physical and chemical properties and finally predicting and showing their applications in devices. Thin films of quantum materials like graphene, NV centers in nano-crystalline diamond or superconductors have shown promise for their rich novel properties dealing with quantum phenomena which have been known to be closely related to the growth techniques. Three articles in this issue attempt to bring out the current excitements in growth and associated properties of these materials. This issue also has an article on graphene coatings developed by electrophoretic deposition technique which interestingly shows resistance to corrosion thereby showing their applications in anti-corrosion devices. Finally, an article in this issue covers the quantum transport in carbon nano-tubes where their application in thin film devices of field effect transistors has been studied through simulations.

We would like to thank Dr. Sangita Bose who agreed to guest edit this issue and put in efforts to bring out this special issue in a timely manner. We also acknowledge the efforts of all the authors for submitting their informative articles in time. We also thank all the members of SMC for their continued support and cooperation in the growth of the Society for Materials Chemistry.

CONTENTS

Feature Articles		Page No.
1.	Recent advancements on graphene thin films <i>Monika Moun and Goutam Sheet</i>	121
2.	A Short Review on Corrosion Resistant Graphene Coating developed by Electrophoretic deposition technique <i>Swarnima Singh, Laxmidhar Besra, Bimal Prasad Singh, Sriparna Chatterjee</i>	130
3.	A Journey from Carbon Atom to Nanocrystalline Diamond <i>Jitendra Nuwad, Dheeraj Jain and V. Sudarsan</i>	138
4.	Growth and Characterization of amorphous Molybdenum Germanium (a-MoGe) and amorphous Rhenium Zirconium (a-Re₆Zr) superconducting thin films using Pulsed Laser Deposition (PLD) technique <i>Somak Basistha, Vivas Bagwe, John Jesudasan, Gorakhnath Chaurasiya, Soumyajit Mandal, Surajit Dutta, Pratap Raychaudhuri</i>	150
5.	Quantum transport under the influence of transverse magnetic field in coaxially-gated carbon nanotube field effect transistor <i>Tapender Singh and Padmnabh Rai</i>	160

Recent advancements on graphene thin films

Monika Moun and Goutam Sheet*

*Department of Physical Sciences, Indian Institute of Science Education and Research (IISER) Mohali,
Sector 81, S. A. S. Nagar, Manauli, PO: 140306, India
Email: goutam@iisermohali.ac.in*

Abstract

The premium electrical, mechanical and optical properties of atomically thin graphene have revolutionized the emerging field of 2D materials based devices. The large area uniform growth of high-quality graphene films is indispensable to fully harness its potential for the industrial applications. The interest in this field has grown rapidly, owing to the ability of 2D materials to be transferred onto another substrates of choice without affecting their fundamental properties. In this review article, an attempt is made to provide the description of the recent work on graphene thin films. The article includes synthesis routes for its industrial scale growth, electronic and opto-electronic properties of the transferred films, turbostratic graphene layers, wrinkle formation in graphene thin films followed by the challenges that need to be overcome for better utilization of graphene for fabricating state of the art electronic devices.

Key Words: Graphene films, synthesis process, transfer techniques, electrical properties, turbostratic, wrinkles.

1. Introduction

Graphene, the first ever discovered 2D layered material has garnered significant research attention all over the world due to its superior electrical, optical, mechanical and thermal properties[1-3]. It has found potential applications in the various fields including field effect transistors[4], flexible wearable devices [5], supercapacitors[6], sensors [7], display for organic light emitting diodes (OLEDs)[8], touch screen and biological applications such as DNA sequencing etc. [9]. Practical device requirements such as CMOS devices, transparent devices have led to the fast growing research thrust in the field of graphene thin films with high demand of wafer scale high quality uniform thin films with controlled thickness. Since, reliable high quality production in scalable fashion is needed for industrial purpose, it is of utmost important to find the cost effective growth techniques of 2D graphene. In general, polycrystalline metallic foils or films are considered over single crystals for graphene growth due to massive growth limitation on the latter. However, in terms of preserving structural integrity, mechanical exfoliation route in which layers are extracted directly from the bulk highly oriented pyrolytic graphite crystal using a scotch tape, has been the best method so far[4]. The pristine graphene layers obtained by this method have low defect density and are used as the standard measuring samples for the comparative studies of graphene films synthesized via other routes. Low yield and non-uniform layers with uncontrolled thickness make this method inappropriate for industrial purpose. Several

synthesis routes have been discovered in last couple of years for example, chemical vapor deposition (CVD) and epitaxial growth of graphene for massive growth, which will be discussed in this review article. Besides their ability of large area growth of 2D materials, the synthesis processes have their own limitation on growth substrates. There is a need to transfer graphene films from grown to the target substrates as per their industrial applications. Graphene's electrical and optical properties are strongly affected by its surroundings, including the substrate and any contamination involved in the transfer process. The present article will also focus on the transfer methods for graphene and challenges involved. One important consequence of largescale synthesis and transfer process is the wrinkling phenomenon. The wrinkle formation in graphene films and their effect on the electronic properties of graphene based devices will also be discussed. The review article is structured as follows: Different synthesis routes for large scale growth including top-down and bottom-up approach, transfer techniques adopted so far, the electrical and optoelectronic properties of the transferred graphene films, turbo stratic graphene films, wrinkle formation in graphene layers followed by the challenges and author's perspective.

2. Synthesis methods for thin film growth of graphene

Synthesis methods for graphene growth can be broadly categorized as top-down approach and bottom-up approach.

2.1. Top-down approach

The top-down approach includes the extraction of single or few layers graphene from the bulk crystal. Mechanical exfoliation method, commonly known as scotch tape method was the first top-down approach to get mono or few layers graphene flakes discovered by Novoselov *et al*[4]. Its low yield and non-uniform graphene flakes lead to the discovery of other routes. Chemical exfoliation method has come up as an alternate to mechanical exfoliation method[10]. Liquid exfoliation method consists of chemical dispersion of graphite crystal followed by ultrasonication, in a liquid medium [11,12]. Most preferred solvents are organic solvents such as N,N-dimethylformamide (DMF) and N-methyl-2-pyrrolidone (NMP). Another strategy of chemical exfoliation method includes reduction of graphene oxide [13,14]. Graphene oxide is synthesized by chemical oxidation process of graphite followed by exfoliation via ultrasonication. Unlikely to the scotch tape method, chemical exfoliation method can give comparatively higher yield, 100 % in some cases and thus, can serve as potential route for mass production of graphene sheets [14,15]. Electrochemical exfoliation is another route considered as a fast, environment friendly method to produce high yield of graphene sheets[16]. It involves the intercalation of ionic species under an electro chemical bias which can facilitate exfoliation by ultrasonication[17]. However, chemical exfoliation method has some advantages over mechanical exfoliation route, it displays many disadvantages such as slow yield from technology point of view, non-uniform and non-homogeneous graphene layer which make these methods inappropriate for industrial sectors.

2.2. Bottom-up approach

The bottom-up approach comprises of the methods of graphene synthesis by molecular growth. Various methods of graphene synthesis will be discussed next.

2.2.1. Chemical vapor deposition

Chemical vapor deposition (CVD) has shown its potential to grow uniform large scale polycrystalline films on metallic films and foils such as nickel and copper [18, 19]. Few-layer graphene were grown by Yu *et al.* on polycrystalline Ni foils[20]. The nickel foils were first annealed in hydrogen and then exposed to a methane under argon and hydrogen gas environment at high temperature of 1000 °C. Similar approach was adapted by Li *et al.* to synthesize large-scale single layer graphene on copper films[21]. The thickness of the synthesized graphene layers was observed to be dependent on the cooling rate. Various precursors with low temperature have been used by researchers to grow large area

monolayer and few layers graphene films. Further, Bae and collaborators demonstrated a modified CVD method that used large flexible rolled copper foils inside the furnace to enable large scale uniform homogeneous graphene growth called “roll to roll” method[22]. Despite the fact that CVD method can produce uniform large area graphene films, the synthesized layers consist of defects and grain boundaries which may limit their extensive use in modern device applications.

2.2.2. Graphene growth on crystalline substrates

Growth of graphene layers has also been shown on crystalline substrates such as silicon carbide (SiC)[23, 24]. Silicon carbide is a known material applicable in high-power devices. Graphene growth with controlled number of layers has been demonstrated on the SiC wafer by sublimation of Si atoms[25]. However, the high quality of graphene layer can be achieved by this method with hundreds of micrometer sized crystallites, high cost of the SiC wafers and high temperature limit the applicability of this method in industries. Growth of SiC on industry compatible Si wafers can be an efficient way to harness the advantage of growing graphene on SiC, but this approach requires further development.

2.2.3. Other growth methods

Graphene growth can be achieved on arbitrary surfaces and at low temperatures using plasma enhanced CVD technique (PECVD)[26] and molecular beam epitaxy (MBE)[27] but the latter is not compatible to industrial applications due to high cost. The issues to be resolved in uniform large area growth of graphene are high temperature during synthesis, uniformity of the synthesized film and prevention of unwanted doping from the underneath substrate etc.

3. Transfer techniques of the graphene layer onto another substrates

For practical applications, graphene layer onto different substrates is generally required as per the application e.g. transparent substrates are necessary for optoelectronic applications, flexible for wearable electronics etc. The growth processes have their own limitation on the choice of substrates. In general, large area graphene films are grown on metallic films. Absence of dangling bonds in 2D materials makes it easier to transfer the 2D layer onto desirable substrates. The most common transfer technique is the use of polymers such as poly-methyl-meth-acrylate (PMMA). PMMA is spin coated on the graphene/metal sample followed by the chemical etching of the metallic film/foil. For graphene grown on nickel and cobalt, FeCl₃ solution is used as the metal etchant[28, 29]. For Fe

substrate, HCl has been used as the etchant[30]. PMMA/graphene membrane is then transferred onto the desired substrate. Thus, graphene film is finally obtained after removal of the PMMA in acetone. Apart from PMMA, poly (bisphenol A carbonate) (PC)[31] and polyisobutylene (PIB)[32] have also been used as supporting polymer layers. PC can be easily removed using organic solvents such as chloroform and further annealing is also not required. PIB layer has been used as the self-release layer between PDMS sheet and graphene film as investigated by Song *et al*[32]. Polymers like PMMA can induce doping in the graphene layer [33]. To remove unwanted doping and clean transfer, pentacene ($C_{22}H_{14}$) thin film served as the suitable replacer of PMMA as demonstrated by Kim *et al*[34]. They successfully transferred the graphene layer to 6 inch silicon wafer. After transfer, pentacene was removed by thermal evaporation and tetrahydrofuran (THF). High temperature annealing after graphene is transferred onto the target substrate is considered as an effective way for polymer residues removal, but this is not applicable to flexible plastic substrates. The conventional wet transfer techniques involve the use of etchants to remove underneath metal substrates, which have many disadvantages, such as high cost, metal particles contamination and environmental pollution etc. which restrict the production of graphene films in scalable fashion. For polymer free transfer, Polydimethylsiloxane (PDMS) stamp, thermal tape and graphite holder are also used known as the dry transfer methods [28, 36, 37] One reliable and efficient technique for large scale growth and transfer of graphene films is the “Roll-to-roll” method[22]. 30 inch graphene film was synthesized and transferred by two rollers and thermal release tape using this method.

Unlikely to the polymer assisted transfer process, Wang *et al.* demonstrated the “clean-lifting transfer” technique wherein polymer layer is not used [38]. This method uses an electrostatic generator to induce the charges on the target substrate. The electrostatic forces enable the graphene film to be attracted towards the transfer substrate by the electrostatic force. This technique is free from polymer residues and thus, clean transfer of graphene film is obtained. For the transfer process of graphene/SiC samples, the metal/polymer layer has also been utilized, for example, Au/polyimide and Pd/polyimide layers have been used to successfully transfer graphene from SiC [39, 40]. The polyimide and the metal layer were removed by oxygen plasma reactive ion etching and metal etchant, respectively. This way, large area graphene film can be transferred layer by layer. But the Raman spectra results showed that transferred layer contained more defects than the synthesized one. Tanabe *et al.* used the polymer poly(vinyl alcohol) (PVA) for transfer process to get doping free graphene, called the “Etch-free” technique as the PVA layer was dissolved by water [41]. This method is environment friendly for epitaxially grown graphene layers but some issues need to be concerned such as defects and residues. Figure 1. represents transfer techniques, clean lifting transfer and roll to roll transfer adopted by different groups. The transferred graphene films may contain polymer residues and cracks. Good adhesion of graphene with the substrate minimizes the cracks, therefore, choice of substrate on which film is transferred is also important. However, all the above discussed methods have made it possible to transfer graphene grown on one substrate to another. The further development in the transfer techniques will

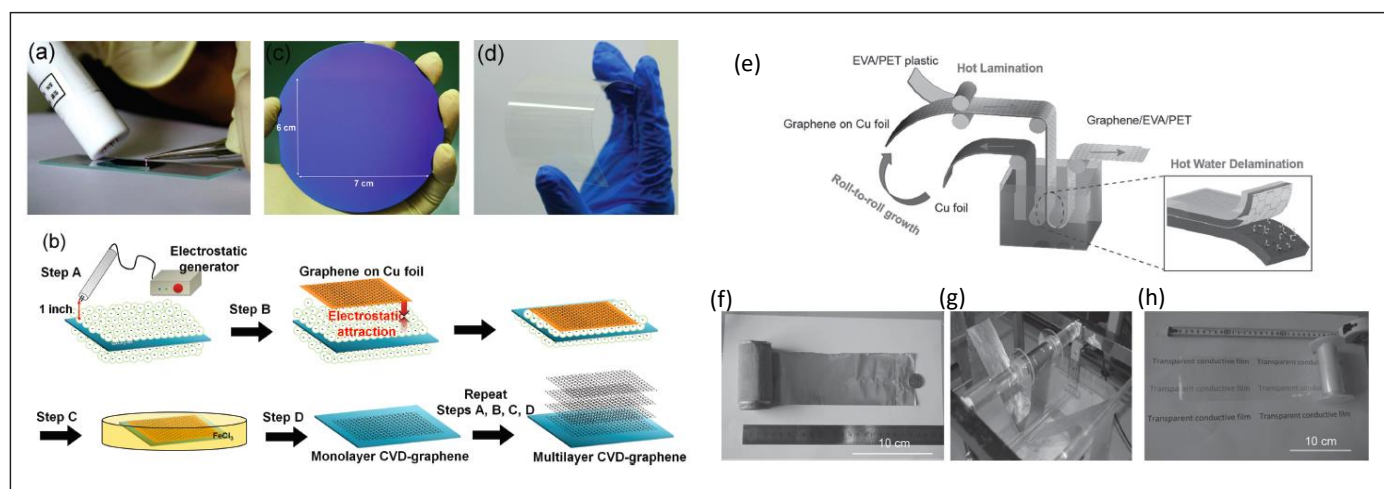


Fig. 1: Transfer techniques (a-d) Clean lifting transfer of graphene film from copper foil to SiO₂/Si and flexible PET substrate using electrostatic generator[38], Reprinted with permission, 2013, Wiley online library (e-h) Roll to roll transfer of graphene grown on copper foil to flexible EVA/PET plastic[35], Reprinted with permission, 2015, Wiley online library.

promote the future application of graphene grown on metal substrates and epitaxially grown on crystalline substrates.

4. Electronic properties of as-synthesized and transferred graphene films

Electrical properties of graphene film are greatly influenced by the environment. The transfer process of graphene films from the grown substrate to another substrate involves chemicals and polymers whose residues can't be removed completely causing alteration in the properties of the graphene film. Physisorbed and chemisorbed molecules on the surfaces of graphene film may induce doping or scattering sites in the film and thus altering its electrical and thermal properties. Prior reports have indicated that PMMA can be a potential source for p-type doping in graphene. For example, Pirkle *et al.* showed that residual PMMA layer on graphene film can cause p-type doping in graphene field effect transistors (GFETs) resulting in increased charge scattering and thus low field effect mobility of $1413 \text{ cm}^2\text{V}^{-1}\text{s}^{-1}$ [42]. Very high mobility of $4050 \text{ cm}^2\text{V}^{-1}\text{s}^{-1}$ has also been reported in large area transferred graphene FET device [43]. But for most cases, field effect mobility for transferred CVD graphene based electronic devices ranges from $200 - 3000 \text{ cm}^2\text{V}^{-1}\text{s}^{-1}$ at room temperature [44, 45].

The reported wide range of mobility depends on the growth processes, transfer techniques and device fabrication steps. Annealing of the transferred graphene film at high temperatures in ultrahigh vacuum have shown reduction in the PMMA layer residues and improved device performance [42]. However, annealing cannot entirely remove the PMMA layer. Furthermore, high temperature annealing in graphene/SiO₂ can lead to reduced mobility due to strong interaction between graphene film and the underneath SiO₂ substrate which escalates the charged impurities effect at the interface. In addition, high temperature annealing is not suitable for every substrate such as flexible plastics used for graphene conducting electrodes. Apart from annealing in the furnace or oven, a current passage through the graphene film utilizing Joule heating effect has been reported to eliminate the chemical contamination on graphene film [46]. The effect of polymer (PMMA) concentration on the electrical properties of transferred graphene layer has also been investigated using X-ray photoelectron spectroscopy (XPS) and Raman spectroscopy. Unlikely to highly concentrated PMMA that leaves uneven and thick polymer layer, a low concentrated PMMA solution leaves less residue after acetone exposure [33]. Thus, less p-doping is observed in transferred graphene film with

higher mobility in FET devices. The electrical properties of graphene films (mobility) can further be improved by formamide exposure. Another study shows that the graphene film transferred using pentacene displayed excellent electrical performance with the field effect hole and electron mobilities, 8050 and $9940 \text{ cm}^2\text{V}^{-1}\text{s}^{-1}$, respectively, higher than that of PMMA assisted transferred graphene based FETs [34]. Figure 2. represents electronic performance of graphene based FET devices by various research groups. The electrical performance of the devices based on the transferred graphene films

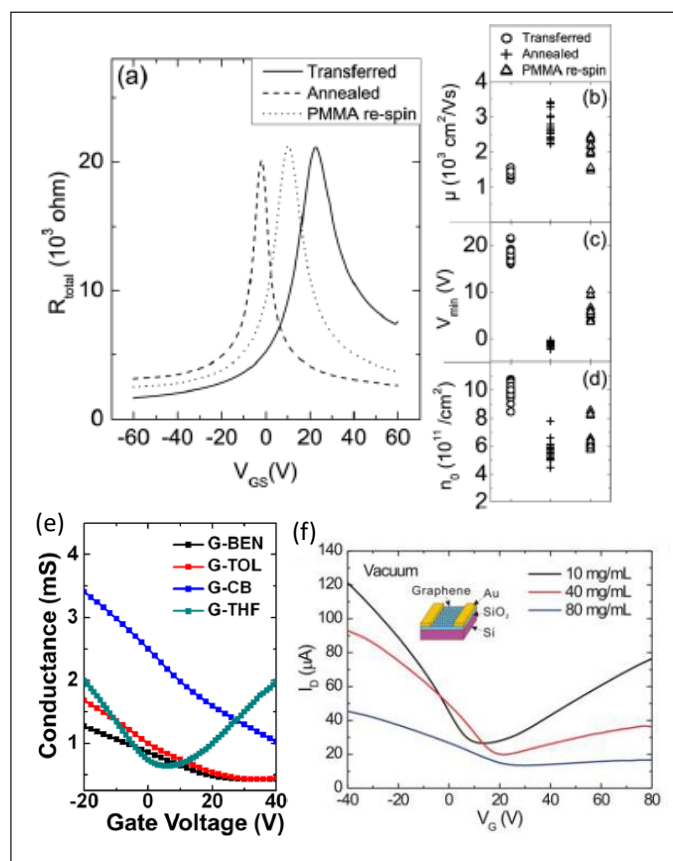


Fig. 2: Electrical characteristics of various FET devices based on transferred graphene films (a) Back-gated graphene FET measurements under vacuum carried out for transferred CVD graphene (solid curve), after ultrahigh vacuum annealing (dashed curve) and after re-spinning PMMA followed by its removal using acetone (dotted curve). Back gated FET device parameters on different devices: (b) field effect mobility, (c) minimum conductivity point (V_{min}), and (d) intrinsic carrier concentration [42] (a-d) Reproduced with permission, 2011, American Institute of Physics (e) Gate-dependent conductance of transferred graphene films using solutions: benzene (G-BEN), toluene (G-TOL), chlorobenzene (G-CB), and tetrahydrofuran (G-THF) [34], Reproduced with permission, 2015, American Chemical Society (f) Current-voltage characteristics in vacuum for the FET device as a function of the polymer PMMA solution concentration [33], Reproduced with permission, 2013, American Chemical Society.

depend on various factors including synthesis process, contamination during transfer process, the target substrate on which the film is transferred and the fabrication tools etc.

5. Large area transferred graphene films for opto-electronic devices

Graphene displays exotic optical properties like high optical transparency, in addition to flexibility, high mechanical strength and environmental stability. The emergence of graphene in the field of photonics has been shown in several applications ranging from photodetectors, organic light-emitting devices to touch screen panels, solar cells and ultrafast optical devices [47-49]. Most of these applications of graphene require transparent substrates and flexible in some applications. As the large area graphene films can't be grown directly on these substrates limited by synthesis protocol, therefore, transfer of graphene onto the desired foreign substrates is essential. Bae *et al.* used roll to roll method for synthesis and transfer process of graphene [22]. The graphene films were transferred onto flexible transparent polyethylene terephthalate (PET) substrate using thermal release tape. The transferred graphene films showed high optoelectronic performance with low sheet resistances and 97.4% optical transmittance for application in touch screen panel device. The graphene/PET device showed better performance as compared to commonly used ITO based flexible devices. Other optical device applications of graphene films include high performance, energy efficient, flexible, low cost, thin organic light emitting diodes (OLEDs) with high transparency [50, 51]. Graphene films can act as transparent electrodes which is an essential component of OLEDs as its electrical properties are preserved upon bending, even at large bending radius. Polat and collaborators demonstrated use of transferred multilayer graphene on paper as an electrically reconfigurable medium for display applications.

6. Turbostratic graphene films

The remarkable properties of graphene can be truly detected when there is no substrate underneath or it is suspended so that graphene film is not influenced by the substrate. Researchers have discovered a new kind of graphene layers called turbostratic graphene films which consist of the randomly oriented graphene layers with the adjacent layers at an angle [52, 53]. The layers are decoupled with large interlayer distance, therefore behaving like a suspended single graphene layer as observed from Raman signatures [54]. Theoretical calculations show that stacked graphite layers with angular disorder shows mass less Fermion behavior and electronic structure similar

to monolayer grapheme [55]. The properties of bilayer graphene with the different angles between the layers have been investigated experimentally by Kim *et al* [56]. They showed that FWHM and intensity of 2D peak highly depend on the rotation angles between the adjacent layers. Besides bilayer graphene, the resemblance of multi-layer graphene with the single layer one and decoupling among the layers has been observed on epitaxial graphene/SiC sample by Hass *et al* [57]. Turbostratic graphene films have also been grown on metallic films such as nickel thin films using physical vapor deposition technique[58]. The large area high quality graphene films were observed with the precise control over the temperature and amount of carbon to be deposited.

Furthermore, a modified CVD method has been adapted to grow large area turbostratic graphene films onto a polycrystalline nickel foil [60]. This work used a CVD setup in which naphthalene solution was drop casted on the foil connected to the current-carrying electrodes for Joule heating followed by immediate cooling. The synthesized graphite films behaved as monolayer graphene with high I_{2D}/I_G ratio maintaining high crystallinity. Figure 3. represents different stacking in AB stacked and turbostratic graphene along with the Raman spectra observed for the turbostratic graphene films grown on nickel films. The centimeter scale growth of turbostratic graphene using

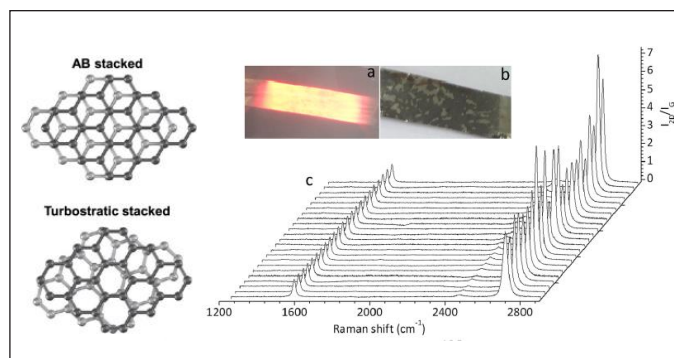


Fig. 3:Representation of stacking in AB stacked graphene and turbostratic graphene films[59], Reproduced with permission (a) Photograph of the Joule heated red hot Ni foil during graphene growth (b) Graphene/nickel film after cooling (c) Raman spectra at different points on graphene film showing high I_{2D}/I_G ratio[60] (a-c) Reproduced with permission, 2015, American Chemical Society.

PVD and CVD on nickel thin films or foils can open new opportunities for future applications such as data storage, flexible electronics and transmission technologies.

7. Wrinkles and their impact on device performance of graphene films

Wrinkling is a common phenomenon in large area 2D films. It can occur during growth process as the

underneath substrate and 2D film have different thermal coefficients, causing wrinkle formation while cooling. Another possibility includes the transfer process of 2D films onto arbitrary substrates. Next, we will discuss both possibilities in detail.

7.1. Wrinkle formation in synthesized graphene films

Graphene grown on metallic foils/films are more likely to have wrinkles owing to the huge difference in their thermal expansion coefficients with reverse polarity [61]. Apart from the thermal compression, the morphology of the underneath substrates also play crucial role in the wrinkle formation in graphene layer. Liu *et al.* showed that the wrinkle formation and their density are governed by the growth substrate, its thickness and the graphene layer transfer process involved [62]. With increase in the thickness of metallic substrate (nickel in this case), grain size of graphene film reduces, resulting in higher density of wrinkles on graphene. Besides metallic substrates, epitaxial growth of graphene on crystalline substrate such as SiC also leads to wrinkle formation due to thermal expansion coefficient difference of graphene and SiC during the cooling process [63].

7.2. Wrinkle formation in transferred graphene films

Graphene layer grown on one substrate is transferred to other substrates for desired applications and during the transfer process, it tends to form wrinkles. Calado *et al.* investigated the wrinkle formation in graphene during the wet transfer process called wedging transfer process onto a hydrophilic substrate [64]. Mechanically

exfoliated graphene flakes are transferred onto another substrate using a hydrophobic polymer and the substrate is “wedged off” by intercalation of water. The wrinkles are formed on and along the water drain channels. Wrinkles density can be controlled by choosing strongly hydrophobic substrates. In this case, the structure and electrical properties of graphene film was not altered by presence of wrinkles. Controlled fabrication of wrinkled structures on graphene has also been reported. Bao *et al.* and later Zhang *et al.* investigated wrinkles in graphene on pre-trenched substrates to get defined microscale wrinkles [65, 66]. The effect of wrinkles on electronic performance of graphene devices has been investigated in recent past. The wrinkles causes strain in the graphene film locally and thus induce lattice deformation [67]. Wrinkles have been considered as line defects in the graphene film and degradation in the device properties of the graphene films were reported attributed to electron-flexural phonon scattering [68-70]. Contrary to these, several reports suggest better electrical transport across the wrinkled film as compared to the flat graphene layer (as shown in figure 4), and therefore, wrinkles are termed as quasi-1D transport channels [71, 72]. More recently, wrinkles have been investigated to behave as highly conducting channels in the turbostratic graphene films [73]. The study utilizes the non-destructive conducting atomic Force Microscopy and Kelvin probe force microscopy to map the electrical properties and shows no significant change in the surface charge density as moving from wrinkled to flat portion and thus, suggesting the possibility of band gap alteration at the wrinkled area.

8. Summary and Outlook

Graphene is a unique 2D material with superior ideal fundamental properties. The desirable industrial scale growth of graphene films is limited by the substrate constraints. Evolution of some growth techniques, for example, roll to roll CVD method has shown promising synthesis route for centimetre scale graphene growth suitable for today’s technology. Turbostratic graphene can also be a potential alternate due to its resembling properties to that of monolayer graphene with no boundation of only one atomic layer. Development in the transfer process of graphene films from grown substrate to substrate of choice has made the state of the art device production more easier and efficient. In this article, we discussed the synthesis and transfer methods of large area graphene films grown on different substrates. Further, the electrical and optoelectronic performance of transferred devices has been reviewed. The transfer techniques have advanced in the last few years, however, there remains

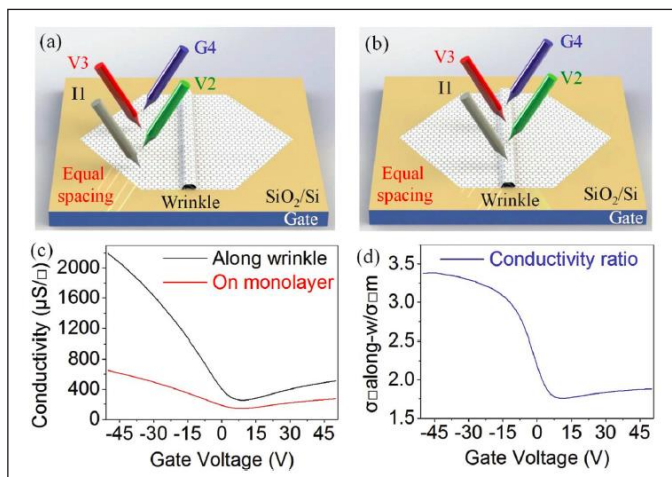


Fig. 4: Four-probe measurement on flat and wrinkled area with equal spacing. (a and b) Schematic illustration of measurements on flat and wrinkled graphene film, respectively. (c) Gate-tunable conductivity for both cases: (a) and (b). (d) Conductivity ratio of measurements along the graphene wrinkle and on the flat monolayer area [72].

some challenges regarding large area transfer. These include minimization of crack and wrinkles formation during synthesis and transfer process, less contamination to get rid of unintentional doping, uniformity in synthesized and transferred single as well as multi-layer graphene, uniform control on the thickness of the films. and low cost. Some transfer methods such as use of pentacene, roll to roll transfer and clean lifting transfer are the promising techniques for large area, contamination free layer transfer while maintaining high electrical performance of the transferred graphene based devices, but most of these techniques are not developed enough for their use in modern technical applications. Wrinkle formation in large area graphene films has shown both positive and negative impact on device performance of graphene films. As suggested by recent reports, it is believed that wrinkles can show huge potential in nanoscale devices where transport mediated by narrow channels are desirable. However, despite extensive interest and continuous experimental efforts by device researchers, far-reaching implementation of graphene based devices has yet to be demonstrated.

Acknowledgements

Monika Moun would like to acknowledge SERB for providing NPDF fellowship (PDF/2020/002122).

References

1. Castro Neto AH, Guinea F, Peres NMR, Novoselov KS, Geim AK. The electronic properties of graphene. *Rev Mod Phys.* **2009**; 81: 109-162.
2. Balandin AA, Ghosh S, Bao WZ, Calizo I, Teweldebrhan D, Miao F, Lau CN. Superior thermal conductivity of single-layer graphene. *Nano Lett.* **2008**; 8: 902-907.
3. Geim AK, and Novoselov KS. The rise of graphene. *Nature Mater.* **2007**; 6(183).
4. Novoselov KS, Geim AK, Morozov SV, Jiang D, Zhang Y, Dubonos SV, Grigorieva IV, and Firsov AA, Electric field effect in atomically thin carbon films. *Science.* **2004**; 306(666).
5. Kim H, Ahn J-H, Graphene for flexible and wearable device applications. *Carbon.* **2017**; 120: 244-257.
6. Tan YB and Lee J-M, Graphene for supercapacitor applications. *J. Mater. Chem. A.* **2013**; 1: 14814.
7. Choi W, Lahiri I, Seelaboyina R, Kang YS. Synthesis of Graphene and Its Applications: A Review *Critical Reviews in Solid State and Materials Sciences.* **2010**; 35: 52-71.
8. Bablich A, Kataria S and Lemme MC. Graphene and Two-Dimensional Materials for Optoelectronic Applications. *Electronics.* **2016**; 5(13).
9. Heerema SJ and Dekker C. Graphene nanodevices for DNA sequencing. *Nature Nanotechnology.* **2016**; 11: 127-136.
10. Amiria A, Naraghib M, Ahmadi G, Soleymanihaa M, Shanbedi M. A review on liquid-phase exfoliation for scalable production of pure graphene, wrinkled, crumpled and functionalized graphene and challenges. *FlatChem.* **2018**; 8: 40-71.
11. Hernandez Y, Nicolosi V, Lotya M, Blighe FM, Sun Z, De S, McGovern I, Holland B, Byrne M, Gun'Ko YK, High-yield production of graphene by liquid-phase exfoliation of graphite. *Nat. Nanotechnol.* **2008**; 3: 563-568.
12. Paton KR, Varrla E, Backes C, Smith RJ, Khan U, O'Neill A, Boland C, Lotya M, Istrate OM, King P, Scalable production of large quantities of defect-free few-layer graphene by shear exfoliation in liquids. *Nat. Mater.* **2014**; 13: 624.
13. Lomeda JR, Doyle CD, Kosynkin DV, Hwang WF, Tour JM, Diazonium Functionalization of Surfactant-Wrapped Chemically Converted Graphene Sheets. *J. Am. Chem. Soc.* **2008**; 130: 16201-16206.
14. Marcano DC, Kosynkin DV, Berlin JM, Sinitskii A, Sun Z, A. Slesarev, L.B. Alemany, W. Lu, J.M. Tour, Improved Synthesis of Graphene Oxide. *ACS Nano.* **2010**; 130: 4806-4814.
15. Sun Z, James DK, Tour JM. Improved Synthesis of Graphene Oxide. *J. Phys. Chem. Lett.* **2011**; 2: 2425-2432.
16. Abdelkader A, Cooper A, Dryfe R, Kinloch I. How to get between the sheets: a review of recent works on the electrochemical exfoliation of graphene materials from bulk graphite. *Nanoscale.* **2015**; 7: 6944-6956.
17. Su CY, Lu AY, Xu Y, Chen FR, Khlobystov AN, Li LJ. High-quality thin graphene films from fast electrochemical exfoliation. *ACS Nano.* **2011**; 5: 2332-2339.
18. Somani PR, Somani SP, and Umeno M. Planar nanographenes from camphor by CVD. *Chemical Physics Letters.* **2006**; 430(56).
19. Obraztsov AN, Obraztsova EA, Tyurnina AV, and Zolotukhin AA. Chemical vapor deposition of thin graphite films of nanometer thickness. *Carbon.* **2007**; 45: 2017.
20. Yu Q, Lian J, Siriponglert S, Li H, Chen YP, and Pei SS. Graphene segregated on Ni surfaces and transferred to insulators. *Appl. Phys. Lett.* **2008**; 93: 113103.
21. Li X, Cai W, An J, Kim S, Nah J, Yang D, Piner R, Velamakanni A, Jung I, Tutuc E, Banerjee SK, Colombo L, Ruoff RS, Large-area synthesis of high-quality and uniform graphene films on copper foils. *Science.* **2009**; 324: 1312-1314.
22. Bae S, Kim H, Lee Y, Xu X, Park JS, Zheng Y, Balakrishnan J, Lei T, Kim HR, Song YI, Kim YJ, Kim KS, Ozyilmaz B, Ahn JH, Hong BH and Iijima S. Roll-to-roll production of 30-inch graphene films for transparent electrodes. *Nat. Nanotechnol.* **2010**; 5(574).
23. Lin YM, Dimitrakopoulos C, Jenkins KA, Farmer DB, Chiu HY and Grill A. 100-GHz Transistors from Wafer-Scale Epitaxial Graphene. *Science.* **2010**; 327(662).
24. de Heer WA, Berger C, Wu X, First PN, Conrad EH, Li X, Li T, Sprinkle M, Hass J, Sadowski ML, Potemski M and Martinez G. Epitaxial Graphene. *Solid State Commun.* **2007**; 143(92).
25. Berger C, Song Z, Li T, Li X, Ogbazghi AY, Feng R, Dai Z, Marchenkov AN, Conrad EH, First PN and de Heer WA. Ultrathin epitaxial graphite: 2D electronic properties and a route toward graphene-based nanoelectronics. *J. Phys. Chem. B.* **2004**; 108: 19912-19916.

26. Woehrl N, Ochedowski O, Gottlieb S, Shibasaki K, and Schulz S. Plasma-enhanced chemical vapor deposition of graphene on copper substrates. *AIP Advances*. **2014**; 4: 047128.
27. Hackley J, Ali D, DiPasquale J, Demaree JD, Richardson CJK. Graphitic carbon growth on Si(111) using solid source molecular beam epitaxy. *Appl. Phys. Lett.* **2009**; 95:133114.
28. Kim KS, Zhao Y, Jang H, Lee SY, Kim JM, Kim KS, Ahn JH, Kim P, Choi JY, Hong BH. Large-scale pattern growth of graphene films for stretchable transparent electrodes. *Nature*. **2009**; 457(706).
29. Wang SM, Pei YH, Wang X, Wang H, Meng QN, Tian HW, Zheng XL, Zheng WT, Liu YC. Synthesis of graphene on a polycrystalline Co film by radio-frequency plasma-enhanced chemical vapour deposition, *J. Phys. D: Appl. Phys.* **2010**; 43: 455402.
30. An H, Lee WJ, Jung J. Graphene synthesis on Fe foil using thermal CVD. *Curr. Appl. Phys.* **2011**; 11: S81-S85.
31. Song J, Kam FY, Png RQ, Seah WL, Zhuo JM, Lim GK, Ho PK, Chua LL. A general method for transferring graphene onto soft surfaces. *Nat. Nanotechnol.* **2013**; 8: 356.
32. Lin YC, Jin C, Lee JC, Jen SF, Suenaga K, Chiu PW. Clean Transfer of Graphene for Isolation and Suspension. *ACS Nano*. **2011**; 5: 2362.
33. Suk JW, Lee WH, Lee J, Chou H, Piner RD, Hao Y, Akinwande D, Ruoff RS. Enhancement of the Electrical Properties of Graphene Grown by Chemical Vapor Deposition via Controlling the Effects of Polymer Residue. *Nano Lett.* **2013**; 13: 1462.
34. Kim HH, Kang B, Suk JW, Li N, Kim KS, Ruoff RS, Lee WH, Cho K. Clean Transfer of Wafer-Scale Graphene via Liquid Phase Removal of Polycyclic Aromatic Hydrocarbons. *ACS Nano*. **2015**; 9: 4726.
35. Chandrashekar BN, Deng B, Smitha AS, Chen Y, Tan C, Zhang H, Peng H and Zhongfan L. Clean Roll-to-Roll Green Transfer of CVD Graphene onto Plastic for a Transparent and Flexible Triboelectric Nanogenerator. *Adv. Mat.* **2015**; 27: 5210-5216.
36. Lin WH, Chen TH, Chang JK, Taur JI, Lo YY, Lee WL, Chang CS, Su WB, Wu CI. A Direct and Polymer-Free Method for Transferring Graphene Grown by Chemical Vapor Deposition to Any Substrate. *ACS Nano*. **2014**; 8: 1784.
37. Kim Y, Kim H, Kim TY, Rhyu SH, Choi DS, Park WK, Yang CM, Yoon DH, Yang WS. Influence of the transfer and chemical treatment of monolayer graphene grown for flexible transparent electrodes. *Carbon*. **2015**; 81: 458.
38. Wang DY, Huang IS, Ho PH, Li SS, Yeh YC, Wang DW, Chen WL, Lee YY, Chang YM, Chen CC, Liang CT, Chen CW. Clean-lifting transfer of large-area residual-free graphene films. *Adv. Mater.* **2013**; 25: 4521.
39. Unarunotai S, Murata Y, Chialvo CE, Kim HS, MacLaren S, Mason N, Petrov I, Rogers JA. Transfer of graphene layers grown on SiC wafers to other substrates and their integration into field effect transistors. *Appl. Phys. Lett.* **2009**; 95: 202101.
40. Unarunotai S, Koepke JC, Tsai CL, Du F, Chialvo CE, Murata Y, Haasch R, Petrov I, Mason N, Shim M, Lyding J, Rogers JA; Layer-by-Layer Transfer of Multiple, Large Area Sheets of Graphene Grown in Multilayer Stacks on a Single SiC Wafer. *ACS Nano*. **2010**; 4: 5591.
41. Tanabe S, Furukawa K, Hibino H. Etchant-free and damageless transfer of monolayer and bilayer graphene grown on SiC. *Jpn. J. Appl. Phys.* **2014**; 53: 115101.
42. Pirkle A, Chan J, Venugopal A, Hinojos D, Magnuson CW, McDonnell S, Colombo L, Vogel EM, Ruoff RS, and Wallace RM. The effect of chemical residues on the physical and electrical properties of chemical vapor deposited graphene transferred to SiO₂. *Appl. Phys. Lett.* **2011**; 99: 122108.
43. Li X, Cai W, An J, Kim S, Nah J, Yang D, Piner R, Velamakanni A, Jung I, Tutuc E, Banerjee SK, Colombo L and Ruoff RS. Large-area synthesis of high-quality and uniform graphene films on copper foils. *Science*. **2009**; 324: 1312.
44. Levendorf MP, Ruiz-Vargas CS, Garg S and Park J. Transfer-Free Batch Fabrication of Single Layer Graphene Transistors. *Nano Lett.* **2009**; 9: 4479.
45. Lee Y, Bae S, Jang H, Jang S, Zhu SE, Sim SH, Song YI, Hong BH and Ahn JH. Wafer-scale synthesis and transfer of graphene films. *Nano Lett.* **2010**; 10: 490.
46. Mosera J, Barreiro A, and Bachtold A. Current-induced cleaning of graphene. *Appl. Phys. Lett.* **2007**; 91: 163513.
47. Bonaccorso F, Sun Z, Hasan T and Ferrari AC. Graphene photonics and optoelectronics. *Nature Photonics*. **2010**; 4: 611-621.
48. Jariwal D, Sangwan VK, Lauhon LJ, Marks TJ and Hersam MC. Carbon nanomaterials for electronics, optoelectronics, photovoltaics, and sensing. *Chem. Soc. Rev.* **2013**; 42: 2824.
49. Wan X, Long G, Huang L and Chen Y. Graphene-A Promising Material for Organic Photovoltaic Cells. *Adv. Mater.* **2011**; 23: 5342.
50. Huang X, Zeng Z, Fan Z, Zhang LJH. Graphene-Based Electrodes. *Adv. Mater.* **2012**; 24: 5979.
51. Wang X, Zhi LJ, Tsao N, Tomovic Z, Li JL and Mullen K. Transparent Carbon Films as Electrodes in Organic Solar Cells. *Angew. Chem.* **2008**; 47: 2990.
52. Shibuta Y, Elliott JA. Interaction Between Two Graphene Sheets With a Turbostratic Orientational Relationship. *Chem. Phys. Lett.* **2011**; 512: 146-150.
53. Malard LM, Pimenta MA, Dresselhaus G, Dresselhaus MS, Raman Spectroscopy in Graphene. *Phys. Rep.* **2009**; 473: 51-87.
54. Cancado LG, Jorio A, Pimenta MA. Measuring the Absolute Raman Cross Section of Nanographites as a Function of Laser Energy and Crystallite Size. *Phys. Rev. B: Condens. Matter Mater. Phys.* **2007**; 76: 64304.
55. Latil S, Meunier V, Henrard L, Massless Fermions in Multilayer Graphitic Systems With Misoriented Layers: Ab Initio Calculations and Experimental Fingerprints. *Phys. Rev. B: Condens. Matter Mater. Phys.* **2007**; 76: 201402.
56. Kim K, Coh S, Tan LZ, Regan W, Yuk JM, Chatterjee E, Crommie MF, Cohen ML, Louie SG, Zettl A. Raman Spectroscopy Study of Rotated Double-Layer Graphene: Misorientation- Angle Dependence of Electronic

- Structure. Phys. Rev. Lett. **2012**; 108: 246103.
57. Hass J, de Heer WA, Conrad EH, The Growth and Morphology of Epitaxial Multilayer Graphene J. Phys.: Condens. Matter **2008**; 20: 323202.
 58. Garlow JA, Barrett LK, Wu L, Kisslinger K, Zhu Y and Pulecio JF. Large-Area Growth of Turbostratic Graphene on Ni(111) via Physical Vapor Deposition. J. Phys.: Condens. Matter **2016**; 6: 19804.
 59. Shimatani M, Yamada N, Fukushima S, Okuda S, Ogawa S, Ikuta T and Maehashi K. High-responsivity turbostratic stacked graphene photodetectors using enhanced photo-gating. Applied Physics Express. **2019**; 12: 122010.
 60. Mogera U, Dhanya R, Pujar R, Narayana C and Kulkarni GU. Highly Decoupled Graphene Multilayers: Turbostraticity at its Best. The Journal of Physical Chemistry Letters. **2015**; 6: 4437-4443.
 61. Obraztsov AN, Obraztsova EA, Tyurnina AV, Zolotukhin AA, Chemical vapor deposition of thin graphite films of nanometer thickness. Carbon. **2017**; 10: 2007.
 62. Liu N, Pan Z, Fu L, Zhang C, Dai B and Liu Z. The Origin of Wrinkles on Transferred Graphene. Nano Res. **2011**; 4: 996-1004.
 63. Vecchio C, Sonde S, Bongiorno C, Rambach M, Yakimova R, Raineri V and Giannazzo F. Nanoscale structural characterization of epitaxial graphene grown on off-axis 4H-SiC (0001). Nanoscale Research Letters. **2011**; 6: 269.
 64. Calado VE, Schneider GF, Theulings AMMG, Dekker C, and Vandersypen LMK. Formation and control of wrinkles in graphene by the wedging transfer method. Appl. Phys. Lett. **2012**; 101: 103116.
 65. Bao W, Miao F, Chen Z, Zhang H, Jang W, Dames C and Lau CN, Controlled ripple texturing of suspended graphene and ultrathin graphene membranes. Nature Nanotechnology. **2009**; 4: 562-566.
 66. Bai KK, Zhou Y, Zheng H, Meng L, Peng H, Liu Z, Nie JC, and He L, Creating One-Dimensional Nanoscale Periodic Ripples in a Continuous Mosaic Graphene Monolayer. Phys. Rev. Lett. **2014**; 113: 086102.
 67. Pereira VM and Castro Neto AH. Strain Engineering of Graphene's Electronic Structure. Phys. Rev. Lett. **2009**; 103: 046801.
 68. Clark KW, Zhang XG, Vlassioug IV, He G, Feenstra RM, and Li AP. Spatially Resolved Mapping of Electrical Conductivity across Individual Domain (Grain) Boundaries in Graphene. ACS Nano. **2013**; 7: 7956-7966.
 69. Willke P, Schneider MA, and Wenderoth M. Electronic Transport Properties of 1D-Defects in Graphene and Other 2D-Systems. Ann. Phys. (Berlin) **2017**; 529: 1700003.
 70. Vasi B, Zurutuza A, Gaji R. Spatial variation of wear and electrical properties across wrinkles in chemical vapour deposition graphene. Carbon. **2016**; 102: 304-310.
 71. Zhu W, Low T, Perebeinos V, Bol AA, Zhu Y, Yan H, Tersoff J, and Avouris P. Structure and Electronic Transport in Graphene Wrinkles. Nano Letters. **2012**; 12: 3431-3436.
 72. Ma RS, Ma J, Yan J, Wu L, Guo W, Wang S, Huan Q, Bao L, Pantelides ST, Gao HJ. Wrinkle-induced highly conductive channels in graphene on SiO₂/Si substrates. Nanoscale. **2020**; 12: 12038.
 73. Moun M, Vasdev A, Pujar R, Madhuri KP, Mogera U, John NS, Kulkarni GU, Sheet G. Enhanced electrical transport through wrinkles in turbostratic graphene films. arXiv2105.00308 [cond-mat.mes-hall] (2021).



Dr. Monika Moun is a post-doctoral fellow in the department of Physical Sciences, IISER-Mohali. She joined the spIN group at IISER Mohali in June, 2020. She obtained her PhD degree from Physics department, Indian Institute of Technology Delhi in 2020. She completed her M.Sc. degree from university of Delhi in 2013. Her principal research interest includes the fabrication of nanoscale devices and experimental investigation of the electrical transport in 2D layered materials



Dr. Goutam Sheet is an associate professor in the department of Physical Sciences, IISER Mohali. He obtained his PhD degree from Tata Institute of Fundamental Research in 2007. He attended Northwestern University and Argonne National Laboratories for postdoctoral research before joining IISER Mohali in May, 2012. His principal research interest includes the experimental investigation of the topologically non-trivial systems (like topological insulators, topological superconductors, Weyl semimetals, Dirac semimetals etc.) using scanning probe microscopy and transport spectroscopy at ultra-low temperatures and high magnetic fields.

A Short Review on Corrosion Resistant Graphene Coating Developed by Electrophoretic Deposition Technique

Swarnima Singh^{1,2}, Laxmidhar Besra¹, Bimal Prasad Singh¹, Sriparna Chatterjee¹

¹Materials Chemistry Department, CSIR-Institute of Minerals and Materials Technology, Bhubaneswar - 751013, India

²Indian Institute of Technology Delhi, Hauz Khas, New Delhi - 110016, India

Corresponding author Email: s_swarnima301@yahoo.in

Abstract

Graphene, an allotrope of carbon consisting of a single layer of atoms arranged in a two-dimensional honeycomb lattice, provides a clear, nanocrystalline coating that can render protection to the substrates from weathering, chemical attack, and UV rays while repelling water, dirt, and other contaminants. The physical deposition process of graphene on the different substrates is quite expensive and difficult to scale up to the commercial level. Therefore, a soft chemical technique like electrophoretic deposition (EPD) could be a versatile technique to coat substrates with graphene for anti-corrosion applications. The advancement in the field of graphene coatings fabricated using the EPD technique is reviewed, and it includes both fabrication and corrosion behavior.

Key Words: Electrophoretic Deposition, Graphene, Coating, Corrosion

1. Introduction

In the past decades, graphene has attracted researcher's attention due to its two-dimensional honeycomb lattice geometry, which is made of sp² hybridized carbon networks [1-2]. It has unique properties such as good chemical inactivity, exceptional thermal and chemical stability, high electrical conductivity, good thermal stability [1-2], and impermeable to molecules yet as small as helium leads to the generation of the barrier layer to protect metals from oxidation and corrosion particularly in the harsh marine environment [3]. Further, graphene forms a natural diffusion barrier providing a physical separation between the protected metal and reactants [3]. Apart from these, graphene is thermally as well as chemically stable in ambient air up to 400 °C. Graphene has a wide range of applications in the field of transistors, memory devices, photovoltaic devices, electron acceptors, electrochemical sensors, and fluorescence sensors [1-3].

Numerous techniques were adopted for fabricating graphene coatings such as chemical vapor deposition (CVD), Sol-gel, thermal oxidation, physical vapor deposition (PVD), plasma spraying, anodizing, plasma electrolytic oxidation (PEO), electrodeposition, electrophoretic deposition (EPD) [3-8]. However, each method has its own merits and demerits. Amongst these coating techniques, EPD is a straightforward and versatile surface treatment method to synthesis graphene-based coatings on different metals and their alloys [9]. Besides, EPD is acquiescent to scaling-up to large dimensions as well as cost-effective, better control over stoichiometry, dimensions, deposition rate, thickness, excellent uniformity [3, 9]. In EPD, charged

particles in suspension travel toward an electrode of opposite charge due to the influence of an electric field and then deposit to form a compact film [10]. In the last ten years, the number of publications that have been increased will emphasize the scope of graphene reinforced polymer coatings via EPD. Researchers have fabricated various polymers such as Polymeric isocyanate crosslinked with hydroxy-functional acrylic adhesive (PIHA) [3], chitosan (CS) [11], poly diallyl dimethyl ammonium chloride [12], polyethyleneimine [13], polyaniline [14], polypyrrole [15], polyethyleneimine [16] in graphene oxide for different fields such as supercapacitors, solar-cells, drug-eluting, orthopedic, anti-corrosive coatings via EPD. Interestingly, Graphene Nanoplatetes (GNPs) as reinforcement in Hydroxyapatite (HA) showed significant enhancement in corrosion resistant up to 87 % compared to pure HA coating fabricated using plasma spraying. Because, randomly oriented wrinkles in the GNPs and their hydrophobic nature effectively hindered the SBF infiltration into the coating and resisted their movement towards the underlying substrate [7].

This review aims to summarize pertinent preceding work and explain the application of the EPD technique in the development of graphene coatings. The corrosion mechanisms of graphene based coatings grown via the EPD technique are also discussed.

2. Electrophoretic deposition (EPD) process

EPD techniques can be applied to deposit particles with surface charges in a stable colloidal suspension. This process includes a working and counter electrode which

is connected to a power source that generates an electric field [17]. The generation of this electric field may be of two types i.e., direct electric current (DC-EPD) and a modulated electric current. Further, the modulated electric current has two types, first alternating current (AC) and pulsed direct current (pulsed-DC). When the positively charged particles are deposited onto the cathode side, then it is known as a cathodic electrophoretic deposition and deposition of the negatively charged particles onto the anodic side, is called anodic electrophoretic deposition. In EPD coatings, the choice of the working electrode is quite flexible in terms of nature, shape, and scale [17]. The electrophoretic deposition process has several advantages such as cheaper deposit coatings, ease in instrument handling, etc. [17]. The EPD coatings can be controlled by manipulating EPD parameters, which are classified in two different ways: (1) suspension characteristics and (2) electric field. The suitable suspension preparation for EPD coatings requires various parameters needs to be manipulated such as particle type, particle concentration in suspension, particle net charge i.e., zeta potential, charging agents, and suspension medium. Further, the electric field includes several parameters such as applied voltage, deposition time, type of electrodes, the distance between two electrodes, and electrode area [17].

In case of electrophoretic deposition of graphene, generally graphene oxide (GO) or reduced graphene oxide is used. Dispersion and stability of graphite flakes is much more complex compared to graphene oxide [18]. So, researchers have developed the path for exfoliation of graphite layer to synthesis graphene or graphene oxide. Dispersion of graphene oxide (GO) and reduced graphene oxide (RGO) in an aqueous solution is easy and stable due to oxygen-containing functional groups. Generally, GO, and RGO is used as a precursor for fabricating graphene coatings for many applications [18].

2.1. Kinetics of electrophoretic deposition

A study of the kinetics of the EPD process is essential to (i) control and manipulate deposition rate and (ii) attain flexibility in micro-structural alteration. Hamaker *et al.* noticed that the weight deposition during EPD is linearly dependent on the proportion of charge flowed. They also anticipated the rate of deposition is proportional to the suspension concentration, deposition time, surface area of deposit, and electric field [19]. EPD can be operated via constant current or voltage by varying suspension concentration with deposition time. Sarkar *et al.* explained the concept of EPD kinetics via schematic graph (shown in Figure 1) of weight deposition versus deposition time for four probable deposition situations [20]. Curve A

signifies constant current and constant concentration of suspension, curve B implies constant current and reduction in concentration suspension, curve C shows the constant voltage and constant concentration in suspension, and lastly curve D implies the constant voltage and reduction in suspension concentration. Curve A indicates that the rate of deposition is constant with time, whereas in curve B, C, and D implies the rate of deposition decreases asymptotically with deposition time. The rate of deposition is highest in curve A in comparison to curves B, C, and D as shown in Figure 1. During constant current i.e., curve A or B, and constant voltage i.e., curve C or D, the implies reduction in the concentration of suspension, when the final yield is reduced and rate of EPD deposition also. Two important points can be concluded from curve A and curve C, yet the concentration of suspension remains constant during a deposition in both curves. Hence, the difference of curve A from curve C is not due to a reduction in concentration suspension, but is due to a reduction in particle velocity with respect to deposition time. This reduction in particle velocity while EPD operated at constant voltage is attributed due to the deposition mass is acting as a shielding effect and higher electrical resistance than the suspension from where deposition occurred [21].

3. Electrophoretic deposition of Graphene coatings

EPD techniques are possible for different solid particles having certain surface charges in a stable colloidal suspension. Since dispersion and stability of graphite flakes is much more difficult compared to graphene oxide. So, researchers have developed the path for exfoliation of graphite layer to synthesis graphene or graphene oxide. Hence, dispersion of graphene oxide (GO) and reduced graphene oxide (RGO) in an aqueous solution is easy and stable due to oxygen-containing functional groups. Generally, GO, and RGO was used as a precursor for fabricating graphene coatings for a wide range of applications. Table 1 represents a review of EPD parameters such as voltage, current and time, suspension medium, substrates used for fabricating graphene coatings for different applications. Generally, RGO is mostly reduced from GO in various ways, such as chemical reduction [22], electrochemical reduction during the EPD process [23-24], and lastly, post reduction after the EPD process. As tabulated in Table 1, that various solvents were used for dispersion of GO, RGO, or modified graphene flakes for fabricating EPD coatings, includes distilled water, isopropyl alcohol, ethanol, dimethylformamide (DMF), N-Methyl-2-pyrrolidone (NMP), acetone, ethanol, etc. Mostly, aqueous solutions are extensively used

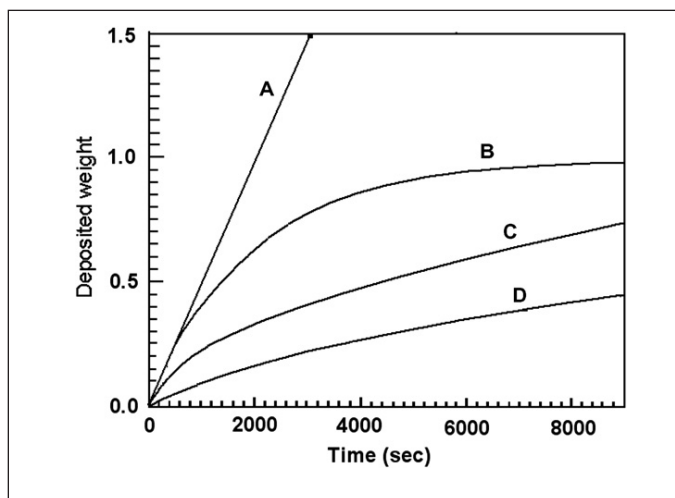


Fig. 1: Schematic of EPD kinetics [Ref: 21]

as a suspension medium for graphene EPD coatings compared to organic solutions. The aqueous solutions have unique advantages such as lower voltage is required for EPD coatings, faster kinetics, higher temperature applicable, low cost as well as environment friendly also. However, aqueous suspensions have certain demerits, such as problems in deposition efficiency and uniformity of the coating. This could be due to the occurrence of electrochemical reactions during EPD process, such as the electrolysis of water, oxidation of the metal electrodes, etc. Mostly, GO, and RGO particles are negatively charged in nature, so in the case of GO and RGO, anodic deposition happens. However, in the EPD process, few metal ions were incorporated into the suspension will adding some salts, namely, LiClO_4 , $\text{Mg}(\text{NO}_3)_2$, $\text{La}(\text{NO}_3)_3$, $\text{Y}(\text{NO}_3)_3$, MgCl_2 , AlCl_3 . Hence, with adding these salts, adsorption of metal ions will occur on the surface, and graphene particles will become positively charged. Furthermore, it was noticed that the addition of Mg salts might destroy the stability of the electrolyte and impact the tribological performance of the EPD based graphene coatings. To overcome this problem, the incorporation of polymers has been introduced as it can transform the surface charge of the graphene flakes owing to their abundant positively charged functional groups.

3.1. Applications of Graphene coating anti-corrosive material

Electrophoretically deposited graphene coatings are exploited as supercapacitors, sensors, mechanical enhancement agents, microextraction, dye pollutants removal, food toxin detection, etc [25-49]. However, focus on the area of anticorrosive coatings remains pivotal since last ten years and it is established that graphene is one of the

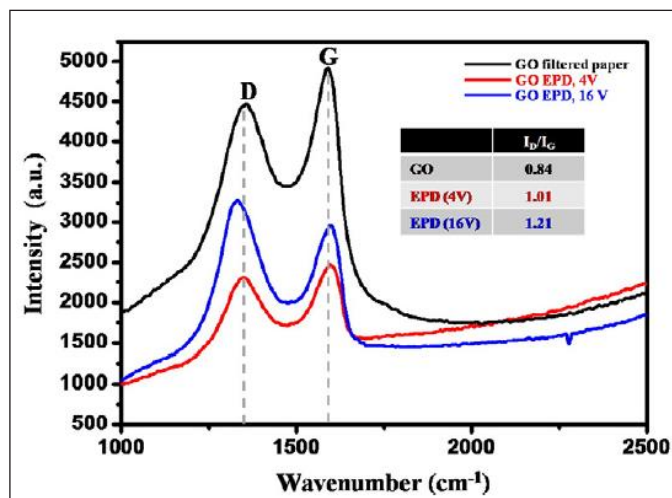


Fig. 2: Raman spectra for GO paper by the filtration of the aqueous GO suspension and EPD GO at 4 V and 16 V [Ref: 1].

most suitable materials for anti-corrosion application. The coating of graphene onto the metal substrate can enhance the corrosion resistance by: (i) filling up of the gaps and crevices with graphene, (ii) chemical inertness of graphene showed great potential by acting as a natural diffusion barrier, and (iii) wrinkling of parallelly oriented graphene sheets, which inhibited the solutions from penetrating the coatings and improve their corrosion resistance [7].

The graphene coating is mainly characterized by Raman spectroscopy. Figure 2 displays the Raman spectra of GO filter paper and EPD based GO coating at 4 V and 16 V. The Raman spectra show two peaks at 1350 cm^{-1} and 1600 cm^{-1} , resembles D and G bands, respectively. The presence of defects was identified by calculating I_D/I_G ratio. The I_D/I_G ratio of GO filtered paper is 0.84, whereas it increased to 1.01 after GO EPD coating fabricated at 4 V, further increased to 1.21 at GO EPD coating prepared at 16 V. Hence increment in I_D/I_G ratio was attributed due to the formation of graphene domains due to the elimination of oxygen functional groups from the GO. However, defects were formed due to the interfacial electrochemical reactions, such as gas generation from the reduction of GO and the water electrolysis too. To evaluate the anti-corrosion behaviour of EPD based GO coatings, usually potentiodynamic polarization experiments are done in 3.5 wt. % NaCl solution along with salt spray test.

Figure 3(a) shows the potentiodynamic polarization plot of the bare mild carbon steel as well as EPD based GO coatings having different deposition mass. It has been evident in Figure 3(a) that corrosion current density of bare as well as EPD coated samples was almost the same. The corrosion potential was slightly shifted in the negative

Table 1: Overview of graphene coatings fabrication using EPD technique

S. No	Graphene precursor	Substrate	Suspension medium	Parameter	Application	Ref.
1.	GO nanowalls	graphite rod	aqueous $Mg(NO_3)_2$ solution	30 V, 10 min	Single- DNA electrochemical biosensing	[25]
2.	GO	Au	Aqueous $LiClO_4$ suspension	-1.2 V, 5-60 sec	supercapacitor	[23]
3.	GO	Si wafer	Ultrapure water	20-45 V, 1 h	Solid lubricant for MEMS/ NEMS devices	[26]
4.	Graphene	Carbon cloth	Water	6 V, 10 h	Solid-state supercapacitor	[27]
5.	rGO	ITO glass	Aqueous $Mg(NO_3)_2$ solution	70 V, 2 min	Food toxin detection	[28]
6.	GO	Carbon fibers	Water	5 V, 1 min	Sizing agent	[29]
7.	GO	Graphite rod	Distilled water	30 V, 10 min	Electrode for electrochemical detection	[30]
8.	GO	Ag	NMP suspension	3 V	Gas sensing	[31]
9.	GO	Carbon steel	Water	4 V, 10 s	Anti-corrosion	[1]
11.	RGO	SS	DI water	3 V, 5 min	Supercapacitor	[22]
12.	GO	Carbon felt	Water	1.5 mA/cm ² , 10 min	Dye pollutants removal	[32]
14.	GO	Glass fibers	Water	10 V, 5 min	Fibre/matrix bond	[33]
15.	GO	Carbon fibers	IPA	160 V, 1 min	Mechanical strength enhancement	[34]
16.	GO	Carbon fibers	Aqueous NaOH solution	20 V, 20 min	Interfacial strength enhancement	[35]
17.	RGO	Carbon fibers	NH_3HCO_3 solution	15 V	Electromagnetic interference shielding	[36]
18.	GO	Steel	DI water	3-4 V, 4-10 min	Corrosion protection coating	[37]
19.	GO	Carbon steel	Aqueous $CaCl_2$ solution	2.3 V, 90 min	Anticorrosive coating	[38]
20.	GO	Copper	DI water	10 V, 1 s	Corrosion prevention	[39]
21.	GO	Micro-crystalline diamond	Ethanol	15 V, 20 min	Tribological enhancement coating	[40]
22.	GO	Carbon fiber	Water	15 V, 30-150 min	In-tube solid-phase microextraction	[41]
23.	GO	Copper	DI water	5 V, 10 s	Anti-corrosive coating	[42]
24.	GO	Carbon fiber	Isopropyl alcohol	160 V, 1 min	Interfacial strength	[43]
25.	GO	Carbon fiber	NH_4HCO_3	15-18V, 20-80 min	Electromagnetic interference shielding	[44]
26.	GO	Carbon fiber	DI water	15 V, 40 min	Interference shielding	[45]
27.	GO	Carbon fiber	DI water	20 V, 10 min	Mechanical	[46]
28.	GO	Carbon fiber	Ethanol	10-30 V, 5 min	Flexural	[47]
29.	Graphene	Carbon fiber	Water	6 - 35 V 30 min	Mechanical	[48]
30.	GO	Carbon fiber	Water	10 min	Interfacial strength	[49]

direction due to the application of GO. Even at higher deposition mass, GO does not show a significant change in corrosion current density. This situation may occur when GO over mild carbon steel does not act as oxidation

barrier. The presence of defects in EPD coatings acts as a corrosion initiation site [1]. However, the main reason for the reduction in corrosion resistance of EPD based GO coatings is poor adhesion strength and the dissociation

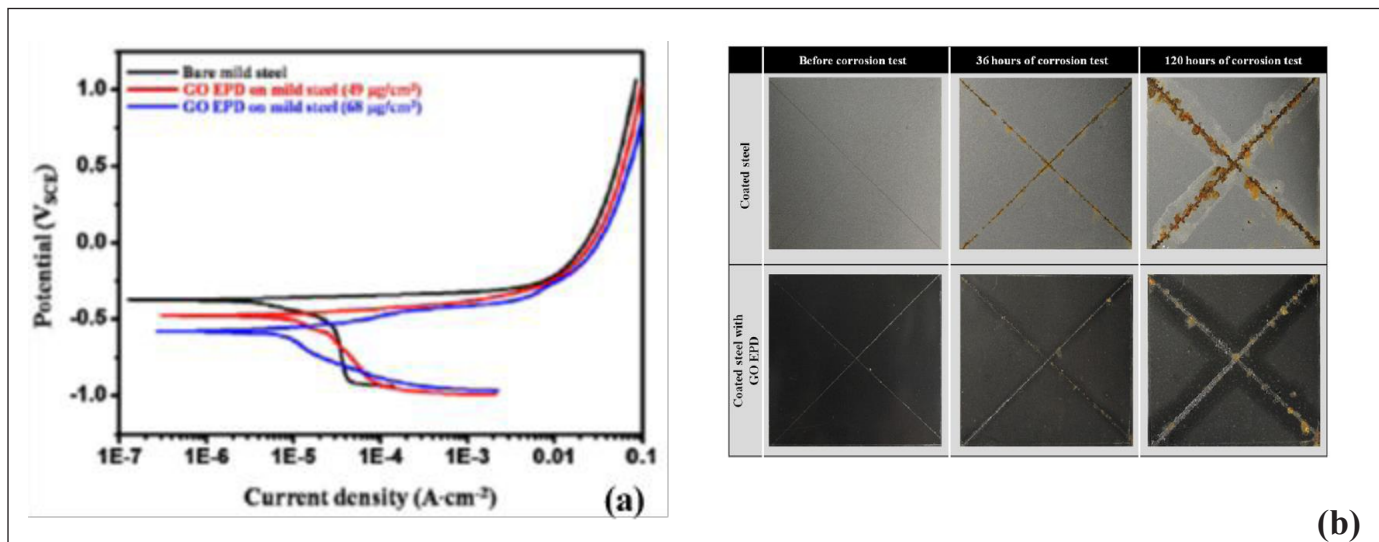


Fig. 3: (a) Potentiodynamic polarization curve of bare mild carbon steel and EPD GO coating with varying thickness in 3.5 wt. % NaCl solution and (b) Optical surface images of bare mild carbon steel as well as EPD GO coatings before and after the cyclic corrosion test [Ref: 1].

of hydrophilic GO by the ionic electrolyte. Few portions of the corrosive electrolyte may penetrate through the organic top coating and samples may get corroded in the chamber of cyclic corrosion test. Figure 3(b) shows optical images of mild carbon steel with an organic top coating and GO-EPD-coated with an organic top coating having a cut mark. It is seen in Figure 3(b) that corrosion resistance was improved after EPD based GO coating compared to the bare substrate.

Since cut parts acted as the anodic site for the corrosion, and the corresponding cathodic site formed around the anodic site. The reduction reaction of dissolved oxygen occurred at the cathodic sites. In EPD coating, access of oxygen and water onto the steel was restricted via GO and the cathodic reaction was reduced due to the shortage of cathodic corrosion reactants. Hence, the anti-corrosion behavior of the organic-coated mild steel with GO EPD was enhanced [1]. Kiran et al. synthesized EPD based GO coating over the copper substrate at 10 V for 1 second and GO was partially reduced with sodium borohydride (NaBH₄) solution during EPD process itself [39]. Further, the corrosion behavior of EPD based GO coatings was studied in 3.5 wt. % NaCl solution. Figure 4(a) displays the open circuit potential of EPD GO coatings and reduced GO coating by NaBH₄. Both the GO coatings shift towards positive potential direction compared to bare copper, indicating an increase in corrosion resistance. Further, Figure 4(b) shows the polarization plot of EPD GO coatings and reduced GO coating by NaBH₄. The corrosion current density of EPD GO coating shows 12.44 µA/cm², which further reduced to 7.01 µA/cm² after reduction of GO with

NaBH₄ compared to bare copper i.e., 15.37 µA/cm². Hence, corrosion potential follows similar trends as discussed in OCP. So, it could be concluded that corrosion resistance of EPD GO coatings was increased twice compared to bare copper [39].

3.2. Prospect

Figure 5 summarizes the magnificent outcome of the previous study reported on EPD based GO coatings with improved corrosion resistance [3, 11, 19, 37-39, 42]. The reason behind the reduction in corrosion current density was assigned to the reduction in the number of pores and cracks present in the coating. The available literatures suggest usage of polymer along with GO to enhance the corrosion resistance of graphene coatings. However, the graphene material still needs research attention with respect to the presence of defects states. The future improvement of graphene coatings is thoroughly linked to the reduction of defects in coating. Therefore, one of the main focus should be to minimize the amount of graphene domain boundaries, since boundaries are mostly populated with defects. Along with that, substrate's surface treatment may also minimize the introduction of impurities in the carbon framework which will in turn improve the coating quality. At the end, emphasis should be put more on the production of large area coating in order to meet the market demand.

4. Conclusion

The current review highlights anti-corrosion behaviour of Graphene coating deposited by electrophoretic

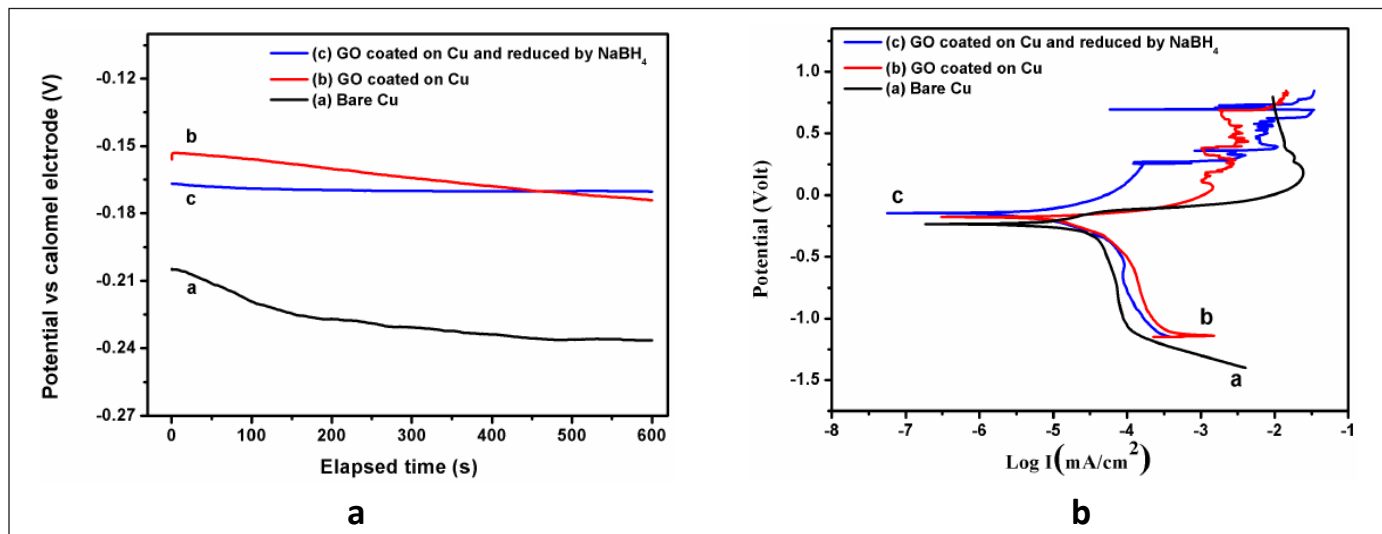


Fig. 4: (a) Open circuit potential (OCP) and (b) Tafel polarization plot of bare Cu, GO coated on Cu and GO coated on Cu and reduced by NaBH_4 [Ref: 39].

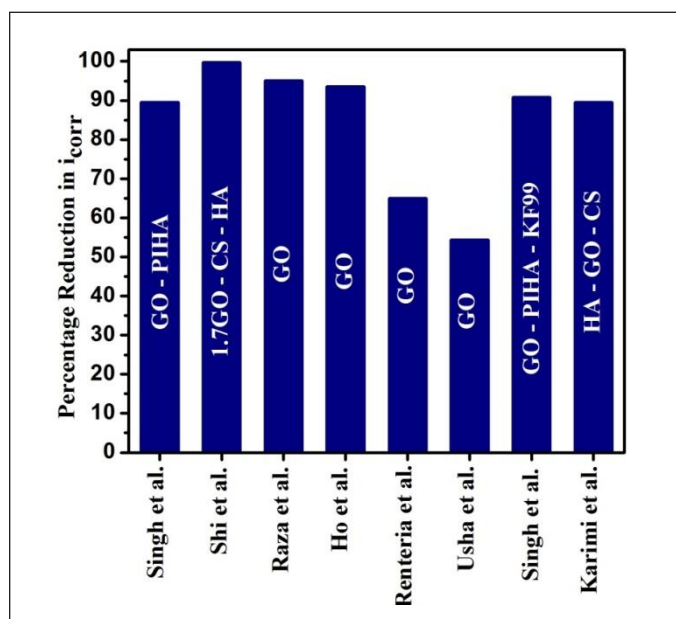


Fig. 5: Literature results showing the percentage reduction in corrosion current density on the corrosion property of EPD based GO coatings.

deposition technique. The electrophoretic deposition process along with process parameters of graphene coating are discussed. It is observed that the limitation of graphene based coating arises from defect formation in coating, which lead to inadequate anti-corrosion strength, especially in long-term exposure in corrosive environment. Few suggestions are made in order to establish graphene as the practical, industry-scale anti-corrosive coating material.

References

- Ji H. P, Jong M. P, *Surface & Coatings Technology* **2014**; (254) 167-174
- Lichun M, Yingying Z, Peifeng F, Guojun S, Yudong H, Hu L, Jiaoxia Z, Jincheng F, Hua H, Zhanhu G, *Composites Part B*, **2019**; (176) 107078
- Bimal P. S, Sasmita N, Kamala K. N, Bikash K. J, Sarama B, Laxmidhar B, *Carbon*, **2013**; (61) 47-56
- Yuehua H, Qunyang L, Ji Z, Yizhou Q, Hongtao W, Pei Z, Yonggang M, *Surface and Coatings Technology*, **2020**; 383 (15) 125276
- Lu F, Qing-Q. H, Ming J. Z, Ji P. Z, Ji M. H, *Electrochemistry Communications*, **2019**; (109) 106609
- Tianlu L, Li L, Jia Q, Fei C, *Progress in Organic Coatings*, **2020**; (144) 105632
- Swarnima S, Krishna K. P, Aminul I, Anup K. K, *Ceramics International*, **2020**; 46, 9 (15) 13539-13548
- Shuping W, Xiangzi D, Tingting C, Songjun L, *Carbohydrate Polymers*; **2018**
- Xiaoming Z, Monica E, Enrico M, *Electrochimica Acta*, **2013**; (102) 252- 258
- Chavez V. A, M. Shaffer S. P, Boccaccini A. R, *The Journal of Physical Chemistry B* **2013**; (117) 1502-1515
- Karimi N, Kharaziha M, Raeissi K, *Materials Science & Engineering C*, **2019**; (98) 140-152
- Yang J, Yan X, Chen J, Ma H, Sun D, Xue Q, *RSC Advance*, **2012**; 2(25):9665.
- Kim S, Oh J S, Kim M G, Jang W, Wang M, Kim Y, Seo H W, Kim Y C, Lee J H, Lee Y K, Nam J D. *ACS Applied Material Interfaces*, **2014**; 6(20):17647-53.
- Tong Z, Yang Y, Wang J, Zhao J, Su B L, Li Y. *Journal of Material Chemistry*, **2014**; 2(13): 4642-51.
- Sookhakian M, Amin Y M, Baradaran S, Tajabadi M T, Golsheikh A M, Basirun W J, *Thin Solid Films*, **2014**; 552:204-11.
- Wang Q, Vasilescu A, Wang Q, Coffinier Y, Li M, Boukherroub R, Szunerits S, *ACS Applied Material Interfaces*,

- 2017; 9(14):12823-31.
17. Mani D, Derrick W. H. F, Aldo R. B, Milo S. P. S, *Progress in Materials Science*, **2016**; (82) 83-117.
 18. Yifei M, Jiemin H, Mei W, Xuyuan C, Suotang J, *Journal of Materiomics*, **2018**;(4) 108-120.
 19. Hamaker H C, *Transactions of the Faraday Society*, **1940**; (36) 279-83.
 20. Sarkar P, De D, Rho H. *Journal of Material Science*,**2004**; (39) 819-23.
 21. Laxmidhar B, Meilin L, *Progress in Materials Science*, 2007; (52) 1-61.
 22. Wang M, Duong L D, Mai N T, Kim S, Kim Y, Seo H, Kim Y C, Jang W J, Lee Y K, Suhr J W, Nam J D, *ACS Applied Material Interfaces*,**2015**; 7(2):1348-54.
 23. Kaixuan S, Yiqing S, Chun L, Wenjing Y, Gaoquan S, *Scientific Reports*,**2012**; (2) 247.
 24. An S J, Zhu Y, Lee S H, Stoller M D, Emilsson T, Park S, Velamakanni A, An J, Ruoff R S, *Journal of the Physical Chemistry Letter*,**2010**; 1(8):1259-63.
 25. Omid A, Elham G, Reza R, *ACS nano*, **2012**; (6) 4: 2904-2916.
 26. Hongyu L, Yong F. B, Junyan Z, Zhongyue C, Aimin L, *ACS Applied Material Interfaces*,**2013**; (5) 6369-6375.
 27. Wang S, Pei B, Zhao X, Dryfe R, *Nanomaterial Energy*,**2013**; 2(4):530-6.
 28. Srivastava S, Kumar V, Ali M A, Solanki P R, Srivastava A, Sumana G, Saxena P S, Joshi A G, Malhotra B D, *Nanoscale*, **2013**; 5(7):3043-51.
 29. Wonoh L, Jea U k L, Hwa J. C, Joon H. B, *RSC Advance*,**2013**; (3) 25609.
 30. Omid A, Elham G, Reza R, Mohammad A, *Carbon*, **2014**.
 31. Lucia S, Viera M, Pietro L, Manna P, Musto A, Borriello G, De L, Michele, *Sensors and Actuators B*,**2014**.
 32. Thi X. H. L, Mikhael B, Stella L, Nihal O, Mehmet A. O, Marc C, *Carbon*, **2015**; (94) 1003-1011.
 33. Haroon M, Manoj T, Nicola P, Alessandro P, *Composites Science and Technology*, **2016**; (126) 149-157.
 34. Caifeng W, Jun L, Shaofan S, Xiaoyu L, Feng Z, Bo J, Yudong H, *Composites Science and Technology*, **2016**.
 35. Jianjun J, Xuming Y, Chumeng X, Yang S, Chao D, Fa L, Jianjun W, *Journal of The Electrochemical Society*, **2016**; 163 (5) 133-139.
 36. Juan C, Jiaming W, Heyi G, Dan Z, Cong L, Xiufeng H, *Composites: Part A*,**2015**.
 37. Ching Y. H, Shih M. H, Sze T. L, Yaw J. C, *Applied Surface Science*, **2017**.
 38. Renteria J. A. Q, Ruiz L. F. C, Mendez J. R, *Carbon*, **2017**.
 39. Usha K, Sanjukta D, Bimal P. S, Laxmidhar B, *Coatings*, **2017** (7) 214.
 40. Sulin C, Bin S, Fanghong S, *Diamond & Related Materials*, **2017**; (76) 50-57.
 41. Juanjuan F, Xiuqin W, Yu T, Yanan B, Chuannan L, Min S, *Journal of Chromatography*
 42. Mohsin A. R, Asad A, Faizan A. G, Arslan A, Khawar Y, Abdul W, Muhammad R, Rafiq A, *Surface & Coatings Technology*, **2017**.
 43. Caifeng Wang, Jun Li, Shaofan Sun, Xiaoyu Li, Feng Zhao, Bo Jiang, Yudong Huang, *Composites Science and Technology* 135 (2016) 46-53
 44. Wu J, Chen J, Zhao Y, Liu W, Zhang W, *Composites Part B*, **2016**.
 45. Juan C, Dan Z, Heyi G, Jian W, *Construction and Building Materials*, **2015**; (84) 66-72.
 46. Jianjun J, Xuming Y, Chumeng X, Yang S, Linchao Z, Chao D, *Composites: Part A*, **2017**; (95) 248-256.
 47. Pui Y. H, Kin-tak L, Bronwyn F, Nishar H, Baohua J, Joong H. L, *Carbon*, **2019**; (152) 556-564.
 48. Pavan K. G, Sagar Y, Sohan K. G, Abhijeet A, Rajesh K. P, Bankim C. R, *Composites Part A*, **2019**; (122) 36-44.
 49. Tong S, Muxuan L, Shengtai Z, Mei L, Yang C, Huawei Z, *Applied Surface Science*, **2020**; (499) 143929. 50.

	<p>Dr. Swarnima Singh <i>Ph. D. (Metallurgical & Materials Engineering)</i> Research Expertise: <i>Coatings (corrosion resistant and wear resistant, biocompatible, mechanical behaviour); Thermal spraying, Biomaterials, Graphene.</i></p>
	<p>Dr. Laxmidhar Besra <i>Ph. D. (Metallurgical & Materials Engineering)</i> Research Expertise: <i>Coatings (corrosion resistant, erosion and wear resistant, biocompatible, thermal barrier, functionally graded, laminates; Solid Oxide Fuel Cells (SOFC); Colloidal Processing of Ceramics; Interfacial phenomena; Flocculation and Dewatering of industrial sludges.</i></p>
	<p>Dr. Bimal P Singh <i>Ph. D. (Petroleum Engineering)</i> Research Expertise: <i>Functional/Structural Nanostructured Composite Coatings, Transparent Conducting Composite Thin Films, Superhydrophobic Engineering Materials, New Generation Energy Storage Materials, Smart and Intelligent Materials, Dispersion of Nano Particulate Matter, Forming Process.</i></p>
	<p>Dr. Sriparna Chatterjee <i>Ph. D. (Chemistry)</i> Research Expertise: <i>Development of multifunctional Coating (Superhydrophobic/Superhydrophilic coating, Corrosion-resistant coating for metal surface, Protective coating for SOFC application, Antimicrobial coating, Heat insulating coating, Anti-reflecting coating); Nanofabrication of materials for GREEN energy application (Dye-sensitized solar cell, Solar H₂ generation, Oxygen reduction, Supercapacitor); Nanofabrication of materials for CLEAN environment application (CO₂ storage, Volatile Organic Compound and Waterborne organics removal)</i></p>

Journey from Carbon Atom to Nanocrystalline Diamond

Jitendra Nuwad^a, Dheeraj Jain^{a,*} and V. Sudarsan^{a,b}

^aChemistry Division, Bhabha Atomic Research Centre, Trombay, Mumbai-400085.

^bHomi Bhabha National Institute, Anushaktinagar, Mumbai-400094.

*Corresponding author Email: jaind@barc.gov.in

Abstract

A brief review of various allotropes of carbon is presented with special emphasis on nanocrystalline diamond (NCD). Two allotropes namely, diamond and graphite occur naturally, while many other forms are synthesized in laboratory. These newer forms include carbon nanotube, fullerenes, graphene, etc., which have widened the applications of carbon-based materials. One such phase is NCD, which exhibits interesting physico-chemical properties due to nano-metric crystallite size regime along with essential attributes of diamond. Structure and properties of NCD as well as various methods to synthesize it are summarized. Effect of different gases in CVD growth process of NCD has also been briefed.

Keywords: Carbon, Allotropes, Diamond, Graphite, Nanocrystalline diamond (NCD)

1. Introduction

The word *carbon* is derived from the Latin word 'carbo', which to the Romans meant charcoal (or ember). It is the fourth most abundant element present in the universe after hydrogen, helium and oxygen. In the form of solid, it is the most abundant element in the universe [1]. Diamond and graphite are two naturally occurring elementally pure forms of carbon, where the former is the hardest bulk material while the latter is quite soft so that it is used as a solid lubricant. Carbon's ability to form different types of chemical bonds has led to a complete branch of chemistry dedicated to its compounds. Nearly ten million compounds of carbon are known at present. Carbon also forms the basis of all life forms on the earth and human body itself consists around 12 % of it.

2. Polytypes of carbon

Carbon (atomic number = 6); a group IV element with ground state electronic configuration $1s^2 2s^2 2p^2$ is an abundant non-metallic tetravalent element. It can be found in diverse bonding configurations as shown in Fig. 1 below.

Pure carbon exists in several different structural configurations (allotropes), which differ in terms of relative arrangement of carbon atoms, although their smallest atomic constituent unit is same (carbon). A few allotropic forms of carbon are briefly discussed below.

2.1 Cubic Diamond

In diamond, each carbon atom is bonded to four other carbon atoms in a tetrahedrally coordinated (sp^3 hybridization) geometry by directional σ -bonds. The crystal structure can be viewed in terms of two interpenetrating face centered cubic (FCC) carbon lattices, which are

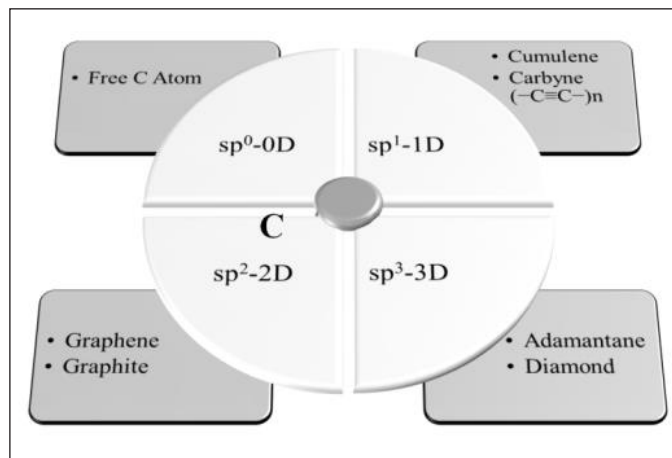


Fig. 1: Various bonding configurations of carbon atom and examples of corresponding materials

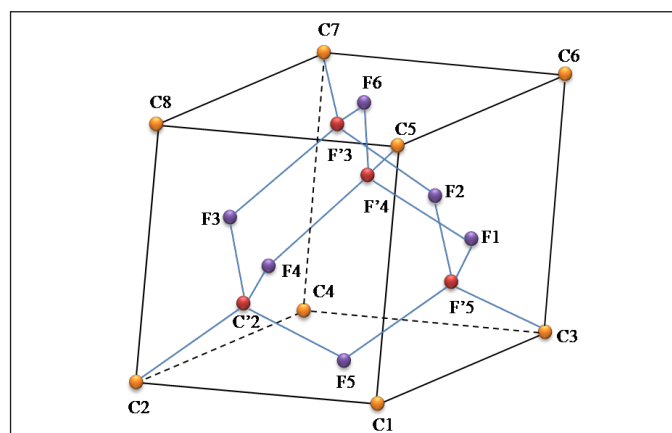


Fig.2: Schematic diagram of diamond crystal structure; •face centered carbon atom of first FCC lattice (F1 to F6); • corner carbon atom of first FCC lattice (C1 to C8); • carbon atom of second FCC lattice (C'2, F'3 to F'5)

displaced from each other along the body diagonal by one fourth of the length of diagonal. Unit cell of diamond is schematically shown in Fig. 2 where 'a' is the cube edge length. A primitive unit cell of diamond therefore has two carbon atoms.

Cubic diamond is a common polytype of carbon found in nature. In terms of layers of carbon atoms, diamond consists of parallel layers of six-membered hexagonal planes stacked in ...ABCABC... sequence. These rings remain in 'chair-conformation' and C-C bonds are staggered as shown in Fig. 3(a). Another conformation consists of carbon ring stacked in ...ABABAB... sequence with C-C bonds normal to these planes in eclipsed form as shown in Fig. 3(b). Staggered conformation is relatively more stable than the eclipsed conformation as a result of which, cubic polytype of diamond is the predominant structure obtained in both natural as well as lab synthesized diamonds.

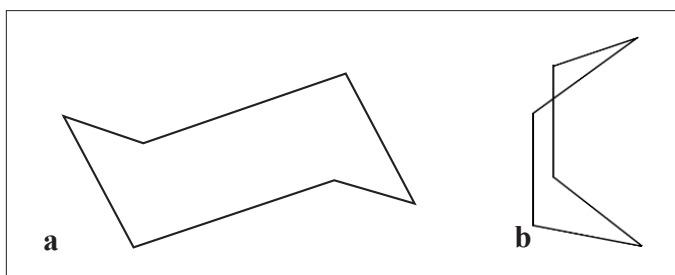


Fig. 3: (a) Staggered conformation (b) Eclipsed conformation

2.2 Hexagonal Diamond (Lonsdaleite)

In this polytype, carbon atoms are arranged in ...ABAB... sequence. This carbon allotrope is usually found at sites where meteorites impact the earth, indicating their formation under high pressure shock waves conditions. In laboratory, lonsdaleite form is produced by shock-wave treatment of graphite. Shock-waves generate high temperature and pressure conditions for short duration under which hexagonal graphite transforms to hexagonal diamond [2, 3]. Since hexagonal polytype of graphite is unstable in nature, lonsdaleite occurrence is rare. From structural perspective, building block of cubic diamond and lonsdaleite can be represented by diamondoid and wurtzoid, respectively [4], which is schematically shown in Fig. 4 for clarity.

2.3 Graphite

Graphite has a layered structure with hexagonal closed packed lattice as shown in Fig. 5. Here, carbon atoms occupy lattice site of a two dimensional honey-comb network where these layers are stacked over one another in ...ABAB... packing configuration. A unit cell of graphite consists of 4 carbon atoms; one each from top and bottom

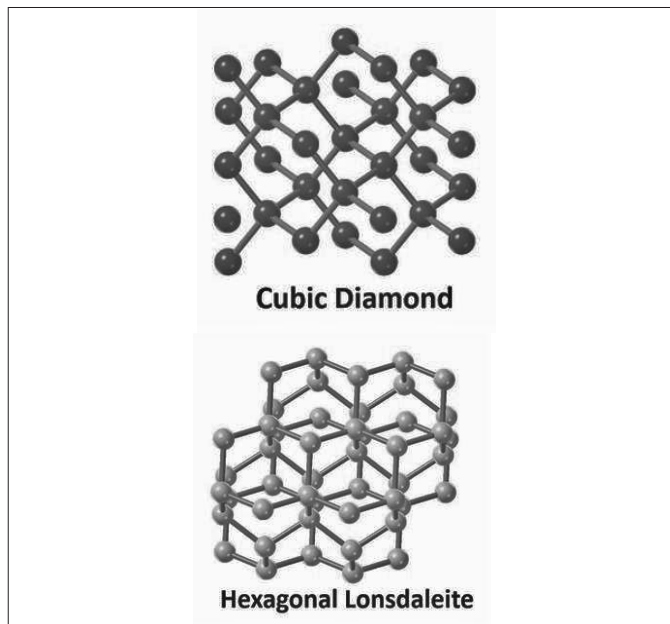


Fig. 4: Structure of (a) cubic diamond and (b) hexagonal diamond (lonsdaleite)[5]

layer while two from the middle layer, as shown in Fig. 5. The in-plane inter-atomic distance is 1.42\AA and the inter-layer distance may vary over 3.35\AA to 3.7\AA , depending on graphite polytype. Such variations result in loss of packing density in one direction and also loss of three dimensional ordering.

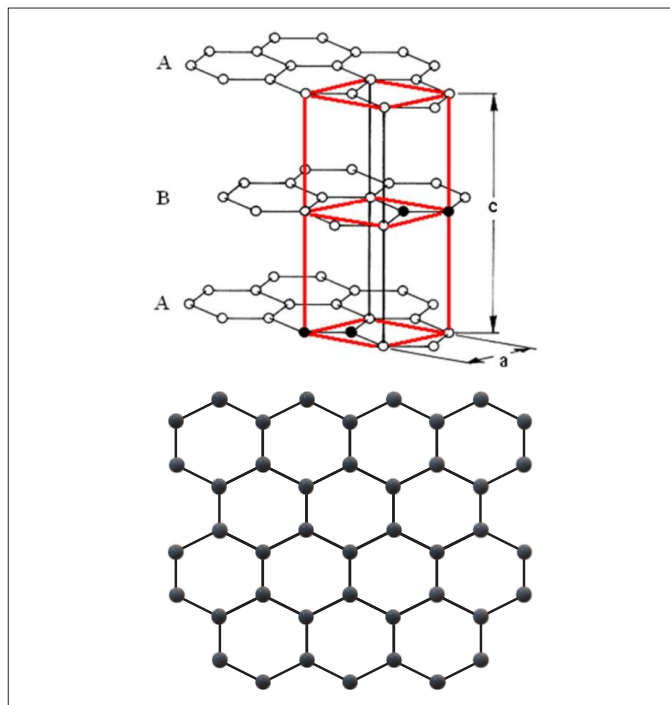


Fig. 5: Crystal structure of graphite with unit cell marked. Planer hexagonal framework of a single layer of carbon atoms in graphite is also shown

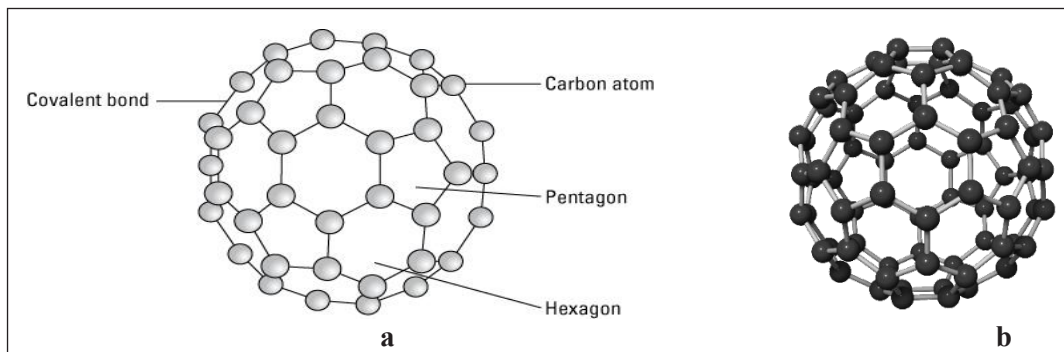


Fig. 6: Molecular structure of (a) C_{60} and (b) C_{70} fullerenes [6]

2.4 Fullerene (C_{60} and C_{70})

Molecular structures of C_{60} and C_{70} fullerene are made-up of 60 and 70 carbon atoms, respectively. Carbon atoms are bonded in cage-like structure forming spherical (C_{60}) and oval (C_{70}) shaped cages. In fullerenes, all the carbon atoms are trigonally bonded and form a spheroid. C_{60} molecule is made-up of 12 pentagons and 20 hexagons while C_{70} molecule consists of 12 pentagons and 25 hexagons. This has been shown schematically in Fig. 6. Fullerene molecules follow isolated pentagon rule (IPR) where all the carbon-pentagons are surrounded by carbon-hexagons.

2.5 Ta a-C and a-C

Tetrahedral amorphous carbon (Ta a-C); also known as hydrogenated amorphous carbon consists of complex network of sp^2 and sp^3 -hybridized carbon atoms. Fraction of sp^3 -bonded carbon usually exceeds 70% in this form and properties of such films are governed by fraction of sp^3 -sites. Domination of sp^3 -sites creates diamond-like structures. On the other hand, amorphous carbon (a-C) mainly consist of sp^2 -bonded carbon clusters interconnected by a random network of sp^3 -bonded atomic sites [7] as shown in Fig. 7.

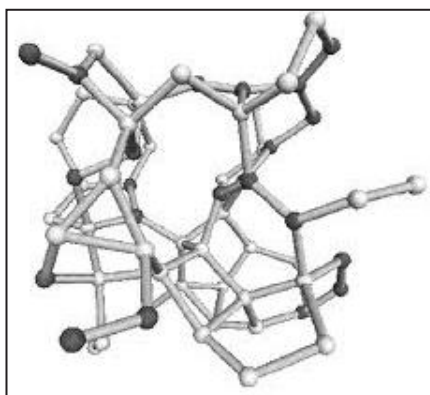


Fig. 7: Schematic structure of tetrahedral amorphous carbon (Ta a-C) showing a network of both, sp^2 -hybridized (black spheres) and sp^3 -hybridized (white spheres) carbon atoms [8]

2.6 Carbon nanotubes (CNT)

First discovered by Iijima [9], carbon nano tubes (CNT) consists of graphitic carbon atom sheets (also known as graphene) rolled in the form of cylindrical nanostructures having nanometer size tube diameters. CNT's are classified as single-walled nanotubes (SWNTs) and multiwalled nanotubes (MWNTs) in which a single graphene sheet or multiple layers of graphene sheets are rolled in the form of tubes, respectively. Figure 8 shows two configurations of CNT's rolled at different angles.

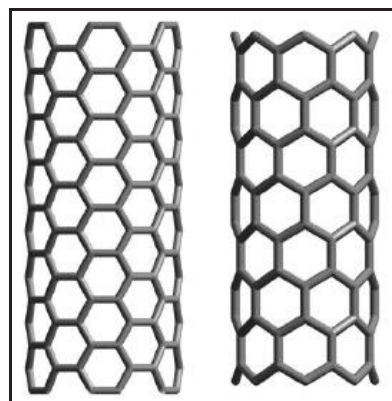


Fig. 8: Single walled carbon nano tube in armchair and zigzag configurations [10]

2.7 Carbon Black

Buseck *et al.*, defined carbon black as a light-absorbing refractory carbonaceous matter; principally composed of [11] amorphous carbon. It is usually produced upon incomplete combustion of heavy petroleum product such as coal tar. It is obtained in the form of fine powders having very large surface to volume ratio.

2.8 Carbon Onions

These are also known as zero dimensional carbon structures or onion-like carbon (OLC) or carbon nano-onions (CNOs). These nanometric spherical-shaped structures (diameters < 10 nm) consist of concentric

fullerene like shells resembling with layers of onion, as observed in high resolution electron microscopic analysis [12].

2.9 Glassy Carbon

Glassy carbon is a non-graphitizing carbon, which possesses the properties of glasses and ceramics. Non-graphitizing attribute indicates that it cannot be converted into crystalline graphite upon heat treatment even at higher temperatures. Structure of glassy carbon consists of ribbon-like morphology formed by sp^2 -hybridized carbon atoms as shown schematically in Fig. 9 [13]. Large fraction of micro voids is present in glassy carbon, which results in lower density ($\sim 1.5 \text{ g/cm}^3$) as compared to that of bulk graphite ($\sim 2.26 \text{ g/cm}^3$).

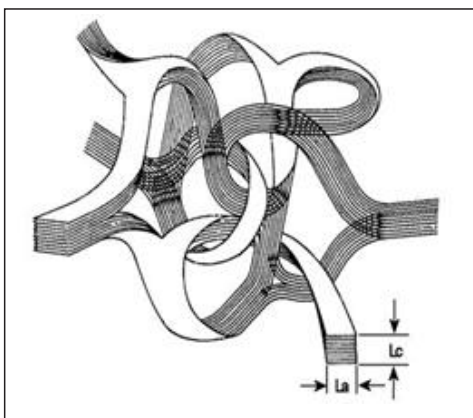


Fig. 9: Schematic morphology of glassy carbon

2.10 Carbon Soot

Carbon soot is defined as nanometer sized (diameter $< 100 \text{ nm}$) spherical particles, which are composed of concentric wrapped, graphene-like layers of carbon [11]. It also contains black carbon. Carbon soot is formed during incomplete gas-phase combustion of hydrocarbons, burning of coal, forest fires, etc.

3. Phase Diagram of Carbon

Figure 10 shows equilibrium temperature-pressure phase diagram of carbon reported by Bundy [14]. Stability region of two wellknown allotropes, namely, diamond and graphite can be noted. While graphite phase is more stable at lower pressure regions, diamond is the preferred phase at higher pressures. Strong network of covalent sp^3 C-C bonds can withstand enormously high pressures. Various pressure-temperature island regions are also indicated where diamond can be synthesized using different techniques such as chemical vapor deposition (CVD), high pressure high temperature (HPHT) method, catalytic HPHT method, shock wave method, etc.

3.1 Nanocrystalline Diamond and the Modified Phase Diagram

Equilibrium phase diagram of carbon provides information about relative stability of two main allotropes namely, diamond and graphite at different temperatures and pressures. At nano-scale however, this phase diagram is redrawn considering 'clusters size' as the third parameter apart from pressure and temperature. For carbon clusters consisting of hundreds to thousands of atoms, phase equilibrium line calculations have been reported by Vicelli *et al.*, [15, 16], wherein contribution from surface energy was added to the total energy due to high surface to volume ratio of these nanostructures. Barnard *et al.*, [17] showed that with increasing cluster size, various carbon nanostructures stabilize in the following sequence: fullerene, carbon-onions, bucky diamond, nanodiamonds and graphite. Theoretical studies have also indicated that contrary to bulk form, nano diamonds (5 - 10 nm) are thermodynamically more stable than graphite [18].

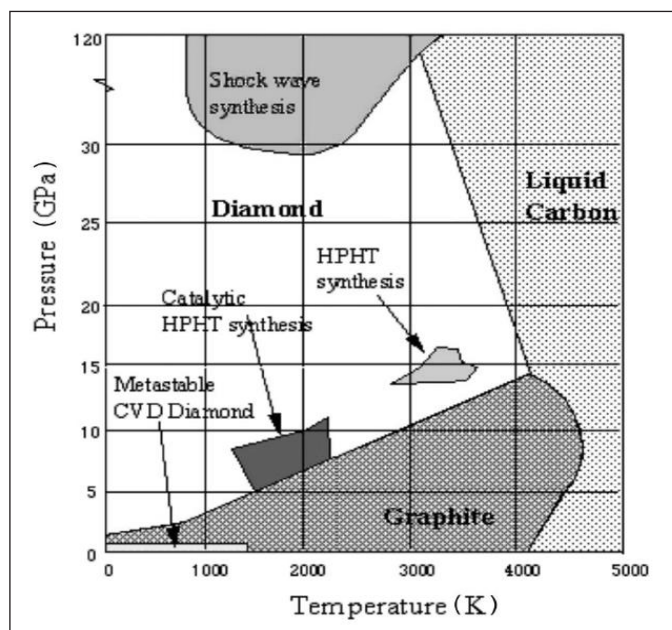


Fig. 10: Equilibrium pressure-temperature phase diagram of carbon [14]

4. Types of Diamond

Diamonds can be classified into two categories namely, (i) natural diamond and (ii) synthetic diamond. Synthetic diamond is further sub-divided in various categories as shown in Fig. 11.

4.1 Natural Diamond

Growth of naturally occurring diamonds takes place in geological conditions of very high pressure and high temperature under the earth. Their growth is influenced

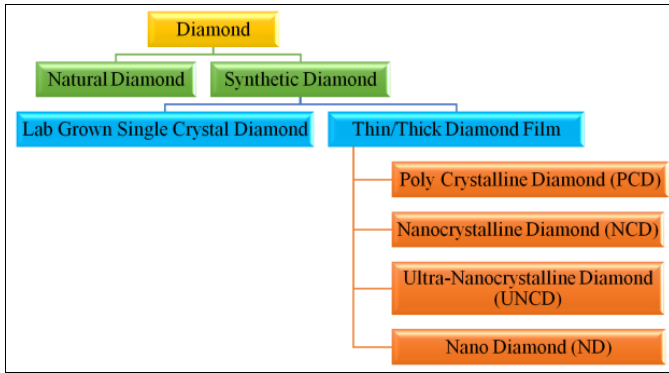


Fig. 11: Classification scheme of diamonds

by the local impurities around their growth environment. Natural diamonds are classified on the basis of (i) impurities present (N, B, etc.) in them and (ii) their light absorption characteristics. Nitrogen is a most common impurity in natural diamond and it is an n-type dopant. Depending upon concentration and type of nitrogen impurity centres, diamonds are further classified into Type I (a and b) and Type II (a and b) [19]. Type I diamonds are nitrogen doped diamonds in which nitrogen is found in aggregated and isolated forms. Type II diamonds are free from nitrogen with type IIa being the purest form having extremely low (or nil) concentrations of nitrogen and boron impurities. Type IIb diamonds contain boron impurities, which imparts their characteristic blue color.

4.2 Synthetic Diamond

These diamonds are synthesized in laboratory. Conditions used for diamond synthesis either resemble the geological conditions under which natural diamonds are formed or are entirely different to achieve its metastable growth. Diamonds can be synthesized in both, single crystals and polycrystalline forms. Single crystals of diamonds are obtained mainly by two methods namely, (i) High-Pressure High Temperature (HPHT) method and (ii) Shock wave method. Both methods involve temperature and / or pressure regimes where diamond is thermodynamically preferred phase over graphite. As a result, diamond phase is predominantly formed and product is obtained in the form of single crystals. Diamond can also be synthesized in the form of films / coatings / plates using simple gaseous precursors via chemical vapour deposition (CVD) route. These films / coatings / plates can be synthesized in the form of single crystals (homoepitaxial growth) as well as polycrystals (hetero-epitaxial growth). By careful control of synthesis parameters, polycrystalline diamonds can be obtained consisting of (i) bulk microcrystalline diamond grains with higher surface roughness of the film, (ii) nanocrystalline

diamond (NCD) grains with relatively smooth surfaces, (iii) ultra nanocrystalline diamonds (UNCD) having very small (< 10 nm) grains and (iv) nanodiamonds (ND), which consists of carbon clusters comprising of both graphitic (sp^2) and diamondoid (sp^3) C-C bonds. Table 1 presents the classification scheme of synthetic diamond on the basis of grain size.

Table 1: Classification of synthetic diamonds on the basis of grain size

Grain size	Type
Less than 10-20 nm	Ultra-Nano Crystalline Diamond (UNCD)
Few tens to hundreds of nm	Nano Crystalline Diamond (NCD)
Few μ m to tens of micron	Micro Crystalline Diamond (MCD)
1 mm or above	Single Crystal Diamond (SCD)

5. Nanocrystalline diamonds (NCD)

Nanocrystalline diamonds are quite hard owing to strong covalent bonds among carbon atoms. They also exhibit low friction coefficient due to absence highly smooth surface [20]. In powdered or film forms, these are used for ultra-smooth polishing of hard disks, coating to carbide drill tools, optical components, wear resistant coating, etc. [21-23]. Methods for synthesis of NCD films are described later in this article. Based on dimensionality, NCDs can be classified as follows:

5.1 Zero-dimensional (0D) structures

These refer to isolated diamond particles with size ranging over few tens of nanometers, which are produced by controlled detonation of explosives to create shock-wave conditions with pressure ranging over 20 GPa to 40 GPa and high temperatures (3000 K - 4000 K). Under these conditions, graphite partially converts into nano-sized diamonds (~20 nm). Adamantane molecule; which is a hydrogen-terminated cubic diamond (diamondoid) consisting of 10 carbon and 16 hydrogen atoms, also falls in this category [24].

5.2 One-dimensional (1D) structures

Diamond whiskers and diamond nanorods are typical examples in this category, which can be synthesized by reactive ion etching method [25].

5.3 Two-dimensional (2D) structures

Single crystal diamond nano-platelets have a two dimensional flat planer structure. CVD synthesis of such

2D nanostructures is reported on a polycrystalline diamond substrate coated with nickel [26].

5.4 Three-dimensional (3D) structures

These can be obtained in the form of powders / films consisting of nanocrystalline diamond grains. Sintered ultra-nanocrystalline diamond (UNCD) particles obtained by detonation route [15], carbide-derived diamond particles [27] and CVD films prepared in environments enriched with noble gases [28] are some of the examples of 3D diamond structures.

6. Relative comparison of diamond, CVD diamond, graphite and NCD

Diamond is a novel material that possesses several unique optical, thermal, mechanical and electronic properties. Properties of graphite are quite different from those of diamond, for which anisotropic structure of former is a major reason. Table 2 lists various properties of diamond, CVD diamond and nanocrystalline diamond (NCD) in comparison with those of graphite.

7. Natural diamond to Nanocrystalline diamond: A brief overview

Physico-chemical properties of natural diamonds are difficult to alter to suit variety of applications. Also, while

shaping of diamond is possible only to a certain extent due to its extreme hardness, obtaining large size natural diamonds is very difficult. These limitations impede effective utilization of natural diamonds for technological and industrial applications other than gemstones. Since many of the industrial applications require diamonds in the form of thin films, coatings and plates having tunable physico-chemical properties, advances in laboratory synthesis methods of diamond have made remarkable impact on diamond-based technologies. These methods include High Pressure- High-temperature (HPHT) method, Shock Wave synthesis, CVD method, etc. [29, 30]. Shock-wave and HPHT methods are cost-intensive and yield products in the form of fine powders (used in abrasive industry) and small single crystals (1-5 mm; used as gemstones), respectively. On the other hand, CVD synthesis of diamond has dramatically expanded the scope of diamond utilization since product can be obtained in the form of films, coatings, plates as well as bulk single crystals. These CVD diamonds find extensive applications as optical windows, host for radiation detection, bio-sensors, heat-sinks, etc. [31-34]. Properties of CVD grown microcrystalline diamond films are comparable to those of natural bulk diamond [35]. CVD grown polycrystalline diamond (PCD) films usually show higher surface roughness (except in the case of oriented films), which

Table 2: Properties of diamond, CVD diamond, NCD and graphite

Property	Diamond	CVD Diamond	NCD	Graphite
Hardness (GPa)	100	80 - 100	95	0.04 - 2.4
Density (g/cm ³)	3.51	3.51	2.75 - 3.4	2.09 - 2.23
C - C Bond length at RT (Å)	1.545	1.54	1.54	1.421
Lattice constant (RT) (Å)	3.567	3.567	3.566	a, b = 2.46, c = 6.708
Thermal expansion coefficient (1/K)	1.1 × 10 ⁻⁶	1.1 - 2 × 10 ⁻⁶	1.7 - 3 × 10 ⁻⁶	25 × 10 ⁻⁶ (in c direction)
Thermal conductivity at 20°C (W/cm K)	21	14 (to growth direction) 2 - 8 (⊥ to growth direction)	0.08 - 0.8	3.98 in a, b direction 0.022 in c direction
Refractive index	2.41 - 2.7	2.34 - 2.4	2.32 - 2.54	2.7
Optical transparency	UV to far IR	UV to far IR	UV to far IR (absorption in UV)	Opaque
Dielectric constant	5.7	5.6	3.4 - 2.4	37.9
Electron mobility (cm ² /Vs)	2200	1300 - 1500	-	20 × 10 ³ - 100
Hole mobility (cm ² /Vs)	1600	480	0.27	15 × 10 ³ - 90
Band gap (eV)	5.45	5.45	3.4 - 4.5eV	-0.04 eV
Resistivity (Ω cm)	10 ¹⁵ - 10 ¹⁶	10 ¹² - 10 ¹⁶	10 ⁻²	2.5×10 ⁻⁶ (to basal plane) 3.0×10 ⁻³ (⊥ to basal plane)
Optical absorption (cm ⁻¹)	< 0.04	< 0.01	-	-
Friction coefficient	0.2 - 0.6	0.05 - 0.15	≤ 0.1	0.2 - 0.6

causes additional scattering of light, higher friction, wear and reduction in optical transparency [36-38]. While surface roughness can be minimized by mechanical polishing and chemical etching (to some extent) of CVD diamond films, tailoring their bulk properties is achievable by controlling the synthesis parameters such as feed gas concentration, growth temperature and pressure, substrate treatment, etc. By variation of these growth parameters, one can tailor the morphology, grain size, phase purity, etc. of diamond films.

As compared to HPHT method, CVD route is relative cost effective and high-quality diamond films / plates can be reproducibly obtained. While growth of high quality thick diamond plates (thickness ~ 1 mm) requires continuous operation of CVD reactor for several hundreds of hours, nanocrystalline diamond (NCD) films can be synthesized in highly cost effective manner. NCD films also possess remarkable properties and can be employed in numerous applications. With increase in growth rate, while diamond film quality is adversely affected, they find numerous applications as wear-resistant coatings on machining tools, heat-sink applications, etc. [39]. NCD films can also be effectively utilized for such applications.

8. Growth of Nanocrystalline Diamond Films

As compared to microcrystalline / polycrystalline diamond (MCD / PCD), growth process of nanocrystalline diamond (NCD) films mainly differs in the re-nucleation / secondary nucleation process. This causes a reduction in surface roughness of NCD films. In the absence of re-nucleation process, columnar growth of PCD films takes place. Synthesis of NCD films without the re-nucleation process has also been reported by facilitating high nucleation density over the substrate so that full coverage can be obtained in a short duration [40]. With conditions enabling high nucleation density, growth duration should be kept lower so that NCD films are obtained without any formation of larger (sub-micron or micron sized) crystallites. NCD film can also be termed as thin (thickness ≤ 100 nm) polycrystalline diamond films [41].

Mechanical, thermal and chemical properties of NCD are comparable to those of PCD films. NCD films are usually composites consisting of nano-sized diamond and graphitic phases. As a result, it shows properties in between those of diamond and graphite. Both NCDs and UNCDs have nanometer sized grains along with smooth and uniform surfaces having lesser friction coefficients. Due to the presence of graphitic carbon, these films are electrically conductive too. These attributes make NCDs / UNCDs potential candidates for their use in optics, tribology, etc. [42, 43]. Nitrogen doping in NCD / UNCD

has further extended their applications into nano / micro-electrochemical systems (NEMS & MEMS), biotechnology and optical devices [44-46].

NCD films can be grown using different CVD methods such as Microwave Plasma CVD (MPCVD) [1], Hot filament CVD (HFCVD) [48], Direct Current Plasma CVD (DCCVD) [49], etc. Each method has a distinct way to activate the gaseous precursors for film deposition. These methods are currently being developed with the main objective of reducing the crystallite size of diamond particles from micrometer to nanometer range by controlling the gas-phase chemistry and growth parameters. Some of these approaches to obtain NCD / UNCD by CVD route are listed below.

- Use of argon (Ar)-rich plasma with different carbon sources such as methane [50] and fullerenes [51]
- Use of hydrogen deficient plasma, where H_2 is replaced by Ar, He and N_2 gas [52-54]
- Use of higher methane concentrations in the feed gas along with hydrogen [55] and use of lower microwave power [56]
- CVD growth under negative DC bias to the substrate (usually silicon) [57, 58]
- Addition of nitrogen (N_2) [59], oxygen (O_2) [60, 61] in CH_4/H_2 -based systems
- CVD growth under lower deposition pressure [62] and lower substrate temperature [63]

While CH_4-H_2 gas mixture is the most widely used precursor for CVD growth of diamond, various other products such as NCDs and UNCDs as well as different polymorphs of carbon (c.a., graphite) can be obtained by perturbing the diamond growth chemistry by addition of different gases (Ar, He, N_2 , O_2 , etc.) as well as varying the relative concentration of hydrogen apart from other factors like bias, growth pressure, temperature, microwave power, etc. A brief mention of CVD processes and role of various gases (CH_4 , H_2 , N_2 , O_2 , Ar, etc.) on CVD synthesis of diamond are briefly discussed now.

8.1 Types of CVD processes

Two processes namely, hot filament chemical vapour deposition (HFCVD) and microwave plasma chemical vapour deposition (MPCVD) are routinely used for synthesis of diamond films as well as many carbon-based materials. Gas-phase dissociation of carbonaceous molecules in presence of excess (atomic) hydrogen is common reaction in both these methods leading to metastable growth of diamond as well as diamond-

like phases at elevated temperatures and sub-ambient pressures. Fig. 12 (a) and (b) shows schematic diagram of HFCVD and MPCVD reactors, respectively.

In HFCVD method, feed gases (usually H_2 and CH_4) are thermally dissociated over a heated filament (2173 – 2773 K), which is kept above a pre-heated substrate (c.a., single crystal Silicon; 673 – 1373 K). Filament is usually made of electrically conducting refractory metals (W, Re, Ta, etc.) and is kept close to (2-5 mm) silicon substrate. At high temperature (~ 2773 K), a fraction of H_2 molecules dissociates to form atomic hydrogen. High temperature gas-phase chemistry of reactive hydrogen species with carbonaceous molecules (and their dissociation species) leads to deposition of diamond films. In presence of carbonaceous molecules, heated filament may form metal carbide(s), which have catalytic effect on dissociation of H_2 molecule. Carbide formation however deteriorates filament's mechanical strength limiting its use for repeated thermal cycles, which is a limitation of HFCVD method.

In MPCVD method, gas-phase plasma (a mixture of partially ionized gases, electrons, atomic & molecular ions, neutral atoms and molecules in their ground as well as excited state) is utilized to dissociate the precursor gases followed by CVD growth of diamond. Microwaves generated by a DC-powered magnetron head are made to enter in CVD chamber through a quartz window which separates CVD chamber from wave guide. To prevent damage to magnetron head, reflected microwave power is minimized by adjusting the metallic stub tuners and overall efficiency of CVD process is enhanced. Silicon substrate is placed over a molybdenum substrate holder and its

temperature is measured by two color optical pyrometer during film deposition. Suitable vacuum pump(s) coupled with pressure control valve(s) enable desired gas pressure inside the chamber while reactant gases (H_2 and CH_4 / C_2H_2 / C_3H_6O) are fed through precision mass flow controllers. Standing microwaves enter into the water-cooled stainless steel CVD chamber and generate plasma upon interaction with reactant gas molecules. Inside the plasma, reactive gaseous precursors, which are required for diamond growth, are generated mainly via electron impact dissociation mechanism. Electrons absorb energy from the oscillating electric field of microwaves and their temperature reaches up to 5273 K. Gas temperature, on the other hand remains lower (~ 1073 K) in low-pressure plasma. The most generally used frequencies for diamond thin film synthesis are 2.45 GHz and 915 MHz.

8.1.1 Role of Methane in CVD Synthesis of Diamond

Methane (CH_4) is the most widely used source of a carbon during CVD synthesis of diamond. Variation in methane concentration in the feed gas mixture alters gas-phase chemistry and thereby affects growth rate, morphology, quality and properties of diamond films [64, 65]. For example, enhancement in the nucleation density, nucleation rate and adhesion strength of nanocrystalline diamond coatings grown over titanium (Ti) substrate with increasing methane concentration has been reported [66]. Similarly, Yanget. al., have reported enhancement of sp^2 -carbon content from 2% to 25% in NCD films grown by CVD technique with increase in methane concentration from 1% to 100% [67]. Optimization of methane concentration is therefore essential for CVD synthesis of NCD / UNCD.

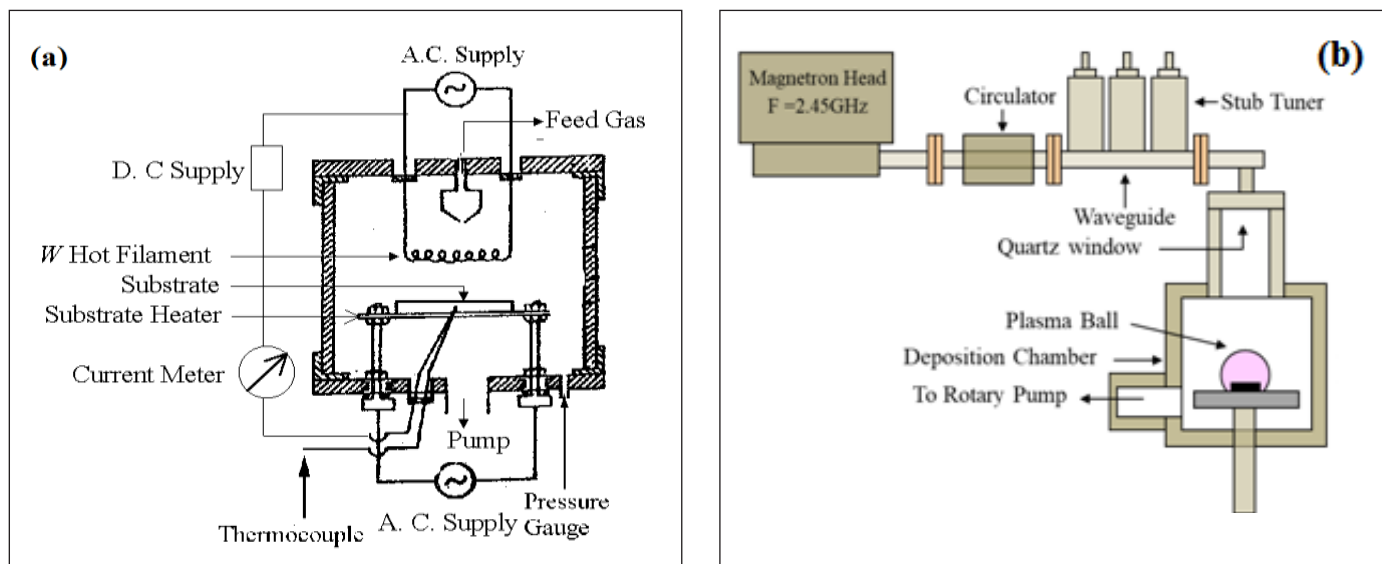


Fig. 12: Schematic diagram of (a) HFCVD and (b) MPCVD reactors

8.1.2 Role of Hydrogen in CVD Synthesis of Diamond

During CVD process, H₂ molecule dissociates into atomic hydrogen (H) and reacts with hydrocarbon molecules to produce a complex mixture of hydrocarbon species and carbon-containing radicals. Hydrogen atom also creates active sites on the growth surface via CH abstraction, which readily adsorb growth precursors (CH_x, C₂, etc.). Atomic hydrogen also preferentially etches the sp²-bonded sites and promotes sp³-bonded sites by attaching to them, thereby leading to polycrystalline diamond film growth. At lower hydrogen concentrations, etching of sp²-carbon is retarded, which promotes re-nucleation. As a result of this, formation of smaller particles induces the growth of NCD. A large increase in hydrocarbon fraction results in the growth of non-diamond phases and further higher concentrations lead to loss of diamond phase [68]. Role of hydrogen on CVD synthesis of diamond has been thoroughly investigated by several researchers [69-71]. Birrell *et al.*, studied the effect of hydrogen on the growth of UNCD films and showed that a threshold hydrogen concentration is essential to stabilize the growing surface of diamond nanocrystals [72].

8.1.3 Effect of Nitrogen gas addition in CVD Synthesis of Diamond

Natural diamonds with yellowish hue usually contain nitrogen impurities. Nitrogen incorporation in diamond lattice creates several defect centers and is known as poison for high-quality diamond films [73]. Addition of nitrogen gas during CVD process leads to increased film growth rate [74]. In small concentration (<1%), N₂ addition also stabilizes {100} facets in diamond crystals [75].

8.1.4 Effect of Oxygen Addition on CVD Synthesis of Diamond

Effect of oxygen addition on CVD synthesis of diamond has been studied with special emphasis on its influence on crystalline quality and film growth rate [76, 77]. Oxygen addition is known to improve the quality of CVD grown polycrystalline diamond films [78]. It also suppresses incorporation of hydrogen impurity in as-grown films [79]. Synthesis of NCD films has also been reported using MPCVD route by varying CH₄ (4% to 42%) in the presence of O₂ (0.1%) in a H₂/CH₄/O₂ plasma [80]. Other than pure oxygen gas, few oxygen containing compounds such as CH₃OH [81] or CO [82] are also known to impact the growth chemistry of high quality diamond films, grown at lower temperatures.

8.2 Doping in Diamond (Boron and Phosphorus)

Doped diamonds are unique in their properties and bring in additional application potential. Due to covalently

bonded carbon atoms network in a closed packed structure of diamond, larger dopant atoms have low mobility. Doping via diffusion route is therefore difficult in diamond. However, it can be accomplished to certain extent during the CVD growth itself by incorporating gaseous dopant precursor. Gaseous precursors containing boron and phosphorus are typically used along with H₂-CH₄ mixture to obtain p-type and n-type diamond, respectively. Post CVD growth, ion-implantation can be used to dope sub-surface layers of diamond. Both boron (acceptor; activation energy ~0.37 eV) and phosphorus (deep donor; activation energy ~0.52 eV) are substitutional impurities in diamond lattice. Heavily B-doped diamonds (5×10²⁰ /cm³) exhibit metallic conductivity [83] at ambient temperature. B-doped diamonds (BDD) have potential uses in electrochemical applications such as low capacitive currents, lesser fouling of electrodes, operation under extreme potential and corrosive environments, etc. [84-87]. It is important to note that un-doped nanocrystalline diamond (NCD) also exhibits higher conductivity than microcrystalline diamond (MCD), which is due to sizable π-bonding and sp²-hybridization. Phosphorus doped diamond (PDD) show the highest conductivity in n-type diamonds [88, 89]. These have also been found useful for electrochemical applications [90]. Phosphorus doping up to 10¹⁸-10²⁰ atoms / cm³ has been reported, which also depends upon its crystallographic orientation [91, 92]. Nitrogen and phosphorus co-doped nanocrystalline diamond have also been reported as good field emitters [93].

Table 3: Applications of CVD diamond films

Diamond Property	Application Area
Radiation hardness	Diamond-based radiation detectors for particulate radiation (alpha, beta, neutrons, heavy charged particles, etc.) Diamond-based beta-voltaics (nuclear batteries)
High thermal conductivity	Heat sink for semiconductor lasers, Electronic components, etc.
Transparency	Windows for IR lasers, optical lenses etc.
Absorption of UV light	UV sensors
Field emission of electrons	Flat-panel displays, electron guns, etc.
Surface chemistry	Bio-sensors, gas sensors, etc.
Biocompatibility	DNA tips
Hardness	AFM probe, anti-wear coating on cutting tools, etc.

9. Applications of CVD Diamond Films

Applications of CVD diamond films stem from their unique physico-chemical properties. Table-3 lists some of these applications based on diamonds' specific properties. By controlling CVD growth parameters, film quality can be tailored for a given application. It is for this reason, CVD synthesis of diamond is envisaged to bring-in more and more applications of diamond films.

10. Conclusions

Various allotrope of carbon have been briefly discussed. Structure and physico-chemical properties of diamond, graphite and nanocrystalline diamond (NCD) have been summarized and their synthesis routes have been discussed. CVD methods for synthesis of nanocrystalline diamond (NCD) films are covered and effects of various gas precursors on the growth process and quality of films have been highlighted. Potential of NCD film is limitless. Its applications have created niche in frontier technologies in industries and many more are yet to be explored.




Acknowledgements

Authors would like thank Dr. A.K. Tyagi, Associate Director, Chemistry Group and Head, Chemistry Division, BARC for constant encouragement and support during the development work of CVD diamond-based device.

References

- J.C. Sung, J. Lin, 'Diamond Nanotechnology: Synthesis and Applications', 1st Ed.; Jenny Stanford Publishing; 2009
- DuPont de Nemours and Co., Netherlands, Patent Release No.: 6506395 (1966).
- H. He, T. Sekine, T. Kobayashi. *Appl. Phys. Lett.* 2002; **81 (4): 610**.
- M. Abdulsattar. *Carbon Lett*, 2015; **16(3): 192**.
- D.G. McCulloch, S. Wong, T.B. Shiell, B. Haberl, B.A. Cook, X. Huang, R. Boehler, D.R. McKenzie, J.E. Bradby. *Small*. 2020; **16-50: 2004695**.
- Web source (<https://www.understandingnano.com/what-is-buckyball-c60.html>)
- P.K. Chu, L. Li. *Mater. Chem. Phys.* 2006; **96: 253**.
- N.A. Marks, D.R. McKenzie, B.A. Pailthorpe, M. Bernasconi, M. Parrinello. *Phys. Rev. Lett.*, 1996; **76: 768**.
- S. Iijima. *Nature*.1991; **354: 56-58**.
- B.P. Grady, 'Carbon nanotube composites', (<http://coecs.ou.edu/Brian.P.Grady/nanotube.html>).
- P.R. Buseck, K. Adachi, A. Gelencser, E. Tompa, M. Posfai. *Atmos. Chem. Phys. Discuss.* 2012; **12: 24821**.
- S. Tomita, T. Sakurai, H. Ohta. *J. Chem. Phys.* 2001; **114: 7477**.
- G.M. Jenkins, K. Kawamura. *Nature*. 1971; **231: 175**.
- F.P. Bundy. *J. Geo. Phys. Res.* 1980; **85(B12): 6930**.
- J.A. Vicelli, F.H. Ree. *J. Appl. Phys.* 2000; **88: 683**.
- J.A. Vicelli, S. Bastea, J.N. Glosli, F.H. Ree. *J. Chem. Phys.* 2001; **115: 2730**.
- A. Barnard, S. Russo, I.K. Snook. *Phys Rev. B.* 2003; **68: 073406**.
- P. Badziag, W.S. Verwoerd, W.P. Ellis, N.R. Greimer. *Nature*. 1990; **343: 244**.
- Chemistry and Physics of carbon, Vol 13, (Eds. G. Davies, P.L. Walker Jr., P.A. Thrower), Marcel Dekker, New York; 1977
- N. Kumar, K. Panda, S. Dash, C. Popov, J.P. Reithmaier, B.K. Panigrahi, A.K. Tyagi, B. Raj. *AIP Adv.* 2012; **2: 032164**.
- X.M. Meng, W.Z. Tang, L.F. Hei, C.M. Li, S.J. Askari, G.C. Chen, F.X. Lu. *Int. J. Ref. Metals Hard Mater.* 2008; **26 (5) 485**.
- A.R. Konicek, D.S. Grierson, P.U.P.A. Gilbert, W.G. Sawyer, A.V. Sumant, R.W. Carpick. *Phys. Rev. Lett.* 2008; **100: 235502**.
- W. Kulisch, C. Popov, 'Deposition, Characterization and Application of Nanocrystalline Diamond Films', In 'Functional Properties of Nanostructured Materials Nato Science Series, Springer, 2006; **223: 263-274**.
- Web source (<https://pubchem.ncbi.nlm.nih.gov/compound/Adamantane>).
- Y. Ando, Y. Nishibayashi, A. Sawabe. *Diam. Relat. Mater.* 2004; **13: 633**.
- H. Chen, L. Chang. *Diam. Relat. Mater.* 2004; **13: 545**.
- Y. Gogotsi, S. Welz, D.A. Ersoy, L.E. Rehn. *Nature*. 2001; **411: 283**.
- D.M. Guren. *Annu. Rev. Mater. Sci.* 1999; **29: 211**.
- H.P. Bovenkerk, F.P. Bundy, H.T. Hall, H.M. Strong, R.H. Wentorf Jr. *Nature*. 1959; **184(4693): 1094**.
- P.S. DeCarli, J.C. Jamieson. *Science*. 1961; **133(3467): 1821**.
- R.S. Sussmann, C.S.J. Pickles, J.R. Brandon, C.J.H. Wort, C.N. Dodge, A.C. Beale, A.J. Krehan, P. Dore, A. Nucara, P. Calvani. *Nuovo Cimento D*. 1998; **20(4): 503**.
- J.A. Dueñas, J. de la Torre Pérez, A. Martín Sánchez, I. Martel. *Appl. Radiat. Isotopes*.2014; **90: 177**.
- C.E. Nebel, B. Rezek, D. Shin, H. Uetsuka, N. Yang. *J. Phys. D Appl. Phys.* 2007; **40(20): 6443**.
- L. Wenzhuang, A. Guoping, L. Pin, S. Yuli, Z. Dan, Z. Dunwen. *Proc. Fourth Int. Conf. Smart Mater. Nanotech. Engg.* 2013; **8793: 129-133**.
- J. Philip, P. Hess, T. Feygelson, J.E. Butler, S. Chattopadhyay, K.H. Chen, L.C. Chen. *J. App. Phys.* 2003; **93(4): 2164**.
- I. P. Hayward, *Surf. Coat. Tech.*, 1991; **49: 554**.
- P.K. Ajikumar, K. Ganesan, N. Kumar, T.R. Ravindran, S. Kalavathi, M. Kamruddin. *Appl. Surf. Sci.* 2019; **469: 10**.
- V. Ligatchev, B. Gan. *Diam. Relat. Mater.* 2006; **15: 410-416**.
- Z. Yuan, Y. Guo, C. Li, L. Liu, B. Yang, H. Song, Z. Zhai, Z. Lu, H. Li, T. Staedler, N. Huang, X. Jiang. *Mater.Design.* 2020; **186: 108207**.
- A.V. Sumant, P. Gilbert, D.S. Grierson, A.R. Konicek, M. Abrecht, J.E. Butler, T. Feygelson, S.S. Rotter, R.W. Carpick. *Diam. Relat. Mater.* 2007; **16: 718-724**.
- O.A. Williams, M. Nesladek, M. Daenen, S. Michaelson, A. Hoffman, E. Osawa, K. Haenen, R.B. Jackman. *Diam. Relat. Mater.* 2008; **17(7-10): 1080**.

42. O.A. Williams, M. Nesladek. *Phys. Status Solidi A*. 2006; **203**: 3375.
43. V. Podgurskya, A. Bogatova, M. Yashina, M. Viljusa, A. P. Bolshakovbc, V. Sedovbc, O. Volobujevad, A. Mered. T. Raadikd, V. Ralchenkobc. *Diam. Relat. Mater.* 2019; **92**: 159.
44. M. Dipalo, J. Kusterer, K. Janischowsky, E. Kohn. *Phys. Status Solidi A*. 2006; **203**: 3036.
45. D. Majchrowicz, M. Kosowska, K.J. Sankaran, P.Struk, M. Wąsowicz, M. Sobaszek, K. Haenen, M. Jędrzejewska-Szczerska. *Materials (Basel)*. 2018; **11(1)**: 109.
46. K.J. Sankaran, DucQuang Hoang, S. Kunuku, S. Korneychuk, S. Turner, P. Pobedinskas, S. Drijkoningen, M. K. Van Bael, Jan D' Haen, J. Verbeeck, Keh-ChyangLeou, I-Nan Lin & Ken Haenen. *Sci. Rep.* 2006; **6**: 29444.
47. J.C. Arnault, S. Saada, M. Nesladek, O.A. Williams, K. Haenen, P. Bergonzo, E. Osawa. *Diam. Relat. Mater.* 2008; **17**: 1143.
48. F.J.H. Guillen, K. Janischowsky, W. Ebert, E. Kohn. *Phys. Status Solidi A*. 2004; **201**: 2553.
49. L.C. Nistor, J. Van Landuyt, V.G. Ralchenko, E.D. Obraztsova, A.A. Smolin. *Diam. Relat. Mater.* 1997; **6(1)**: 159.
50. D. Zhou, T.G. McCauley, L.C. Qin, A.R. Krauss, D.M. Guren. *J. Appl. Phys.* 1998; **83**: 540.
51. D.M. Guren, S. Liu, A.R. Krauss, X. Pan. *Appl. Phys. Lett.* 1994; **64**: 1502.
52. D.M. Gruen. *Annu. Rev. Mater. Sci.* 1999; **29**: 211.
53. K. Subramanian, W.P. Kang, J.L. Davidson, W.H. Hofmeister. *J. Vac. Sci. Technol. B*. 2005; **23(2)**: 786.
54. D.T. Tran, W.S. Huang, J. Asmussen, T.A. Grotjohn, D.K. Reinhard. *New Diam. Front. C Tech.* 2006; **16(6)**: 281.
55. A. Gaydaychuk, S. Linnik. *Int. J. Refract. Met. H.* 2019; **85**: 105057.
56. W. Müller-Sebert, C. Wild, P. Koidl, N. Herres, J. Wagner, T. Eckermann. *Mat. Sci. Eng. B*. 1992; **11(1-4)**: 173.
57. X. T. Zhou, Q. Li, F. Y. Meng, I. Bello, C. S. Lee, S. T. Lee, Y. Lifshitz. *Appl. Phys. Lett.* 2002; **80**: 3307.
58. T. Sharda, M. Umeno, T. Soga, T. Jimbo. *Appl. Phys. Lett.* 2000; **77**: 4304.
59. K. Subramanian, W.P. Kang, J.L. Davidson, W.H. Hofmeister. *Diam. Relat. Mater.* 2005; **14**: 404.
60. R. Erz, W. Dotter, D. Jung, H. Ehrhardt. *Diam. Relat. Mater.* 1993; **2**: 449.
61. K. Teii, H. Ito, M. Hori, T. Takeo, T. Goto. *J. Appl. Phys.* 2000; **87**: 4572.
62. D.M. Gruen, X. Pan, A.R. Krauss, S. Liu, J. Luo, C.M. Foster. *J. Vac. Sci. Technol. A*. 1994; **12**: 1491.
63. W. Kulisch, C. Petkov, E. Petkov, C. Popov, P.N. Gibson, M. Veres, R. Merz, B. Merz, J.P. Reithmaier. *Phys. Status Solidi A*. 2012; **209(9)**: 1664.
64. X.F. Ding, X.Sun, W.J. Wang, H.M. Zhang, H.N. Gao. *Adv. Mater. Res.*, 2014; **1053**: 402.
65. K.K. Hirakuri, T. Kobayashi, E. Nakamura, N. Mutsukura, G. Friedbacher, Y. Machi. *Vacuum*. 2001; **63(3)**: 449.
66. L. Yang, Y. Tang, C. Zhang, L. Zhang, I. Onyeka, Q. Yang, R. Feng, A. Hirose. *Surf. Coat. Tech.* 2001; **206**: 1971.
67. Q. Yang, S. Yang, Y.S. Li, X. Lu, A. Hirose. *Diam. Relat. Mater.* 2007; **16**: 730.
68. H. Sternschulte, T. Bauer, M. Schreck, B. Stritzke. *Diam. Relat. Mater.* 2006; **15**: 542.
69. J.E. Butler, Y.A. Mankelevich, A. Cheesman, Jie Ma, MNR Ashfold. *J. Phys.: Condens. Matter*. 2009; **21**: 364201.
70. J.E. Butler, R. L. Woodin, Thin film diamond growth mechanisms. In: A.H. Lettington, J.W. Steeds(eds), *Thin Film Diamond*. Springer, Dordrecht; 1994
71. S.A. Rakha, Y. Guojun& C. Jianqing. *J. Exp. Nanosci.* 2012; **7(4)**: 378.
72. J. Birrell, J.E. Gerbi, O.A. Auciello, J.A. Carlisle. *J. Phys-Condens. Mat.* 2006; **18**: S1771.
73. S. Bohr, R. Haubner, B. Lux. *Appl. Phys. Lett.* 1996; **68**: 1075.
74. T. Liu and D. Raabe, *Appl. Phys. Lett.*, 2009; **94**: 021119.
75. R. Locher, C. Wild, N. Herres, D. Behr, P. Koidl. *Appl. Phys. Lett.* 1994; **65**: 34.
76. I. J. Ford. *J. Appl. Phys.* 1995; **78**: 510.
77. M. P. D'Evelyn, J. D. Graham, L. R. Martin. *Diam. Relat. Mater.* 2001; **10**: 1627.
78. C.J. Tang, A.J. Neves A.J.S. Fernandes. *Diam. Relat. Mater.* 2004; **13**: 203.
79. L.P. Gu, J. Grácio, J.L. Ribeiro. *Phys. Status Solidi A*. 2009; **206(12)**: 2816.
80. L. C. Chen, P. D. Kichambare, K. H. Chen, J.-J. Wu, J. R. Yang, S. T. Lin. *J. Appl. Phys.* 2001; **89**: 753.
81. Beckmann, W. Kulisch, H. J. Frenck, R. Kassing. *Diam. Relat. Mater.* 1992; **1**: 164.
82. Y. Muranaka, H. Yamashita, H. Miyadera. *J. Appl. Phys.* 1991; **69**: 8145.
83. K. Ushizawa, K. Watanabe, T. Ando, I. Sakaguchi, M. Nishitani-Gamo, Y. Sato, H. Kanda, *Diam. Relat. Mater.* 1998; **7**: 1719.
84. Y. Einaga, J.S. Foord, G.M. Swain, *MRS Bull.*, 2014; **39**: 525-532.
85. Y.V. Pleskov, *Advances in Electrochemical Science and Engineering*, Wiley-VCH Verlag GmbH & Co. KGaA; 2003: 209-269.
86. C.A.M.-H. Enric Brillas, *Synthetic Diamond Films: Preparation, Electrochemistry, Characterization and Applications*, John Wiley and Sons; 2011.
87. Y.E.A. Fujishima, T.R. Rao, D.A. Tryk, *Diamond Electrochemistry*, Elsevier; 2005.
88. S. Koizumi, T. Teraji, H. Kanda, *Diam. Relat. Mater.* 2000; **9**: 935.
89. T. Kociniewski, M.-A. Pinault, J. Barjon, F. Jomard, J. Chevallier, C. Saguy, *Diam. Relat. Mater.* 2007; **16**: 815.
90. Y. Mukuda, T. Watanabe, A. Ueda, Y. Nishibayashi, Y. Einaga, *Electrochim. Acta*, 2015; **179**: 599-60368.
91. N. Temahuki, R. Gillet, V. Sallet, F. Jomard, E. Chikoidze, Y. Dumont, M.-A. Pinault-Thaury, J. Barjon, *Phys. Status Solidi A*, 2017; **214**: 1700466.
92. O. Maida, S. Tada, H. Nishio, T. Ito, *J. Cryst. Growth*, 2015; **424**: 33.
93. F. Lloret, K. J. Sankaran, J. Millán-Barba, D. Desta, R. Rouzbahani, P. Pobedinskas, M. Gutierrez, Hans-Gerd Boyen, K. Haenen, *Nanomaterials (Basel)*. 2020; **10(6)**: 1024.

	<p>Shri Jitendra Nuwad graduated from MDS University and joined BARC in 2002. He is involved in indigenous development of diamond-based radiation detectors for their applications under extreme radiochemical environments. His research work is focused on CVD synthesis of diamond films and related materials; their characterization and applications. His expertise also includes material characterization by electron microscopy technique and development of indigenous experimental facilities. He has developed a process for conversion of natural diamond scrap into pure micron and sub-micron sized diamond powders. The research works carried out has been published in national and international journals. Currently he is pursuing M.Sc. in Chemistry from Mumbai University by Research.</p>
	<p>Dr. Dheeraj Jain did his post-graduation from University of Rajasthan and joined BARC in 2004. His research works include (i) synthesis and characterization of thorium and uranium-based nuclear fuels and related materials and their thermal and thermo-physical characterization, (ii) development of CVD diamond-based radiation detectors and related technologies and (iii) development of indigenous thermo-analytical equipment. He obtained his PhD from Homi Bhabha National Institute and is also involved in teaching. His work has been published in more than 65 research papers and 3 book chapters.</p>
	<p>Dr. V. Sudarsan joined Chemistry Division of BARC in the year 1994 after graduating from 37th batch of BARC training school. He received his Ph. D degree in Chemistry from Mumbai University in the year 2002 for his work on structural aspects of inorganic glasses. Subsequently he worked for a period of two years at the University of Victoria, British Columbia, Canada in the area of structural aspects and luminescence of lanthanide ions doped nanoparticles of inorganic hosts. Currently he is working on optical properties of nanoparticles and glassy materials.</p>

Growth and Characterization of amorphous Molybdenum Germanium (a-MoGe) and amorphous Rhenium Zirconium (a-Re₆Zr) superconducting thin films using Pulsed Laser Deposition (PLD) technique

Somak Basistha^a, Vivas Bagwe^a, John Jesudasan^a, Gorakhnath Chaurasiya^b, Soumyajit Mandal^a,
Surajit Dutta^a, Pratap Raychaudhuri^a

^aDepartment of Condensed Matter Physics and Material Science, Tata Institute of Fundamental Research,
Homi Bhabha Road, Colaba, Mumbai 400005, India.

^bSchool of Physical Sciences, UM-DAE Center for Excellence in Basic Sciences, University of Mumbai,
Kalina Campus, Santacruz (E), Mumbai 400098, India.

*Corresponding author Email: somak.basistha@tifr.res.in

Abstract

We report on the growth and characterization of superconducting a-MoGe and a-Re₆Zr thin films, which are type-II, transition metal superconductors, on a thermally oxidized Si-SiO₂ substrate. We grow the films, at room temperature using pulsed laser deposition (PLD) technique. The superconducting transition temperature (T_c), the normal state resistance (R_N), the upper critical field (H_{c2}), the zero-field penetration depth (λ) and the carrier density (n) were measured as a function of thickness. X-ray analysis showed amorphous nature of the films and the stoichiometry of Mo:Ge as 3:1, while Re:Zr was 6:1. For the MoGe thin films, the T_c ranged from 7.5 K in a 20 nm film, to about 1.6K for a film of thickness around 2 nm. R_N was between 256 Ω to around 2500 Ω , increasing with decreasing film thickness. H_{c2} spanned from 14.8 T for a 20 nm film, to about 6.9 T for a 3 nm film. λ of the films ranged from 530 nm for the 20 nm film, to about 1160 nm for a 2 nm thick MoGe film. The n increased with decrease in film thickness being $3.5 \times 10^{29} \text{ m}^{-3}$ for a 40 nm film, to about $1.3 \times 10^{30} \text{ m}^{-3}$ for a 3 nm film. We observe a change in sign of the Hall coefficient in films around 9-11 nm and argue that this is possibly due to the hybridization of the d-orbitals responsible for electron conduction in our system. In the Re₆Zr thin films, the T_c ranged from 5.9 K in a 40 nm film, to about 2.3 K for a film of thickness around 3 nm. R_N was between 240 Ω to around 2700 Ω , increasing with decreasing film thickness and λ of the films changed marginally for films with thickness decreasing down to 8 nm. The n increased with decrease in film thickness being $8.67 \times 10^{29} \text{ m}^{-3}$ for a 40 nm film, to about $1.7 \times 10^{30} \text{ m}^{-3}$ for an 8 nm film. Magneto-transport measurements point towards a rich magnetic field-temperature phase diagram, while the penetration depth measurements indicate a s-wave coupling for both the superconductors.

Keywords: Amorphous thin film, pulsed laser deposition, superconductivity

1. Introduction

Amongst the various thin film deposition techniques, one of the most used is the Pulsed Laser Deposition (PLD) technique [1]. It is a type of Physical Vapor Deposition, that is a conceptually simple technique, that involves focusing of an intense laser pulse, onto a target and in turn, removing (or ablating) a small portion of the target material in the form of a gas or plasma phase [2]. The ablated material, is then deposited on a substrate that acts as a platform upon which the film is grown. This technique has several advantages like preservation of stoichiometry from target to film, simplicity in setting up, and precise growth of multi-component systems from different target materials, over existing deposition techniques that makes it extremely useful [3]. Though, used for deposition of complex oxide compounds, during its early days of inception (1960s), in 1969, the first elemental metal was deposited using PLD (Schwartz et

al.), while by the 1990s PLD was systematically used for deposition of metallic alloys and multilayers (Gavigan et al., (1991); Singh et al., (1992); Krebs and Bremert, 1993) [4]. Over the last century, solid state physicists have been concentrating on crystals and matters exhibiting perfect crystalline symmetry. This holds true for superconductors too, where for decades, mostly crystalline superconductors were studied. However, in the last 50 years or so, there has been a growing interest in perturbations and distortions to these perfect systems [5]. The same interest has peaked in case of superconductors which are amorphous in nature. The amorphous phase can be considered the most disordered phase of a solid. The first amorphous superconductor was prepared by Buckel and Hilsch in 1954. They evaporated Bi in high vacuum and deposited onto a substrate at liquid Helium temperature [6, 7]. The first systematic study of amorphous superconductors was done by Collver and Hammond, on 4d and 5d

transition metal alloys [8]. The characterizing features of amorphous superconductors are increased value of T_c in the amorphous state, as compared to the crystalline phase for some transition metal superconductors, large value of resistivity in the normal state, higher value of $2\Delta/k T_c$ as compared to the BCS theory which has the value 3.52 for a weak coupling BCS superconductor. A large value of H_{c2} , indicating a small coherence length, along with a large value of $dH_{c2}/dT|_{T=T_c}$ consistent with a large value of normal state resistivity and also the density of states at the Fermi level [9]. Due to their very short electronic mean free paths these materials form good model systems to study the role of disorder on superconductivity [10-19]. Presence of novel vortex phases in these amorphous superconductors has been an area of growing interest [20-22]. From the viewpoint of applications, amorphous superconductors have been used for fabricating superconducting detectors [23-25] and vortex memory devices [26]. Although, a-MoGe is not a new system being studied, literature survey tells that a-MoGe thin films have been prepared using multitarget/co-sputtering or sputtering from a pre-fabricated target alloy [27-31]. We have used PLD to grow these films [32-34]. The reason behind this was to get high quality and homogenous films with stoichiometry being same as that of the target pellet. Also, amorphous superconductors have very low pinning strength, implying their vortex lattice [35-37] is very soft, thereby making them ideal candidates to study the BKT-HNY phase transition [38]. Re_6Zr , the second superconductor we report here, is a non-centrosymmetric (NCS) in the bulk form with a T_c of 6.7K in its crystalline structure. It has a α -Mn cubic structure favoring a time reversal symmetry (TRS) breaking with singlet-triplet mixing [39, 40]. Although bulk measurements on both single crystals and polycrystals showed the existence of a fully gapped single band [41-43], muon spin rotation measurements indicated signatures of TRS breaking. Point contact Andreev reflection measurements also showed presence of a multi-gapped structure [44], pointing towards unconventional superconductivity close to the surface. From these observations we attempt to synthesize thin films of this superconductor where the surface to bulk ratio can be controlled.

In this paper we report on the growth techniques of a-MoGe and a- Re_6Zr thin films using PLD and subsequent characterization of the structural and superconducting properties. The a-MoGe films used in this study were 3 nm to 40 nm thick, and grown on oxidized silicon substrates, starting from a $Mo_{70}Ge_{30}$ target. The T_c of the films varied from 4.6K (3 nm film) to 7.5K (40 nm film), which is also the bulk T_c . We synthesized a- Re_6Zr films up to a thickness(t)

of 120 nm on the same substrate as used for a-MoGe. All such films exhibited superconductivity for thicknesses $3 \text{ nm} \leq t \leq 120 \text{ nm}$, with the T_c approaching 5.9 K for $t \geq 40 \text{ nm}$. We also perform penetration depth, magnetoresistance and Hall measurements in the normal state and employ free electron gas analysis [45] to calculate the Fermi vector, mean free path to estimate the disorder in the films.

2. Experimental Details

2.1 Growth of the MoGe target material

The films were synthesized from a home grown MoGe target. A commercially available Molybdenum rod was taken along with small pieces of Germanium. The components were taken in stoichiometric amounts (Mo:Ge \rightarrow 3:1) and placed on a copper hearth. This hearth is water-cooled and plays the role of an anode in the arc-melting procedure employed to make the MoGe target buttons [46]. The hearth along with the starting materials are loaded onto a chamber in the tetra-arc furnace. The furnace is equipped with a combination of high vacuum rotary and turbo pumps, which bring down the pressure inside the chamber to $\sim 10^{-6}$ mbar. The chamber was flushed three times with gaseous Argon to drive out any impurities that might have been left. The arcs, made of Tungsten, acting as cathodes, are ignited by sending a current of $\sim 50 \text{ A}$. When the temperature of the chamber rises to $\sim 3000 \text{ K}$, the materials kept on the hearth start melting. The chamber is heated for about 10 minutes and then rapidly cooled to achieve an amorphous material. The end product takes a dome shape, with a concave upper surface. The alloy obtained is then flipped upside down, placed on the hearth re-melted again. The process is carried out a total of four times to ensure homogeneity. Two such targets were made of diameter around 18 mm and thickness around 3.4 - 3.5 mm. Subsequently, the top surface was polished with fine emery paper to obtain a flat, smooth ablating surface.

2.2 Growth of the Re_6Zr target material

Re_6Zr films of different thicknesses were grown on surface oxidized Si (100) substrates by PLD. The target material was made using the same arc-melting technique, as was employed for making the MoGe target. Stoichiometric ratio of 6:1 (Re:Zr) was taken in the form of Rhenium powder (99.99% purity) and 99.999% Zirconium shots, both from Alfa Aesar. Rhenium powder was first arc-melted to form small Rhenium shots in a mono arc furnace. Then the shots were taken along with the Zirconium shots and melted to form a button ($\sim 1.1 \text{ cm}$ diameter) in a tetra-arc furnace. The top surface was then polished with emery paper to make it suitable for ablation.

2.3 Synthesis of the films

Both the thin films of MoGe and Re_6Zr were grown on surface oxidized Si (100) substrate (oxide layer thickness ~ 200 nm) using PLD by ablation of the target. A 248 nm excimer laser was used for deposition of the films at room temperature. The deposition was carried out at a base pressure of $\sim 7 \times 10^{-7}$ mbar which is brought about by a combination of high vacuum rotary and turbo pumps. For a metallic thin film, comparatively high energy density is needed to maintain the stoichiometry, close to that of the target, when compared to oxide thin films, and as such the laser was focused in a tight spot, with a repetition rate of 10 Hz on the target, giving an effective energy density ~ 240 mJ/mm², per pulse. The growth rate on an average was 1 nm/100 pulse. Films with varying thickness were grown by changing the number of laser shots. The films used for magneto-transport and penetration depth measurements were capped with a 2 nm thick Si layer to prevent surface oxidation after it was found from initial MoGe thin films, made with the commercial target, that the films were prone to surface oxidation.

2.4 Structural characterization

In both the cases of a-MoGe and a- Re_6Zr , films with $t > 10$ nm, the thickness was directly measured using a AMBIOS XP2 Stylus Profilometer. For thinner samples, it was estimated from the number of laser pulses using the calibration from thicker samples. Scanning electron micrographs (SEM) reveal a featureless surface with low density of particulates. EDX performed gave the ratio of Mo:Ge and Re:Zr in the films. XRD analysis using a Cu K α source, gave a broad hump-shaped contour, indicating the amorphous nature of the films. Further analysis using transmission electron microscopy (TEM) showed concentric circular rings in the diffraction pattern which confirm the amorphous nature of the films. TEM was performed using a Tecnai 20-200 microscope with LaB₆ filament operated at 200 kV. For both a-MoGe as well as a- Re_6Zr , free-standing films were transferred on a Cu grid as follows. First the films were deposited on surface oxidized Si substrates coated with a PMMA layer. The PMMA was dissolved by dipping the substrate in acetone and the free-floating film on acetone was picked up on a Cu grid. It was verified that 20 nm films on PMMA coated substrate had the same T_c (within 0.1 K) as the films of same thickness on surface oxidized Si substrate.

2.5 High frequency electrodynamics and Magneto-transport measurements

Two-coil mutual inductance technique was employed for the penetration depth measurements. In this technique, the film grown in a circular geometry of 8 mm diameter

is sandwiched between a quadrupolar primary coil and a dipolar secondary coil such that the magnetic shielding response is given by the complex mutual inductance, $M = M' + iM''$ measured at 31 kHz. The penetration depth is then calculated numerically, using a theoretical model for the given two-coil setup. (more details can be found in ref.57) The measurements were done in a home-built He⁴ cryostat, which went down to 2 K. The electronics used for this are a pair of Stanford SR830 Lock-ins. The temperature dependence of resistivity (ρ), T_c and the carrier density (n) were measured through a conventional DC four probe technique, in a home-built variable temperature insert (VTI), up to a maximum field of 110 kOe. The current was sent via a Keithley 6220 precision current source and measured in Keithley 2182A nanovoltmeter. The films were patterned through a shadow mask into a Hall bar geometry. The current was passed across a 1.3 mm long and 0.35 mm wide bridge and the voltage was measured across it. The voltage developed was an average of the currents sent in two opposite directions across the film, to negate the Peltier effect occurring at the junction of the films and the Cu and Au wires used to make contacts on the film. The Hall voltage was deduced from reversed sweeps of an externally applied magnetic field, ranging up to 11 T, after subtracting the resistive contribution.

3. Results

3.1 a-MoGe thin films

Fig 1(a) shows the x-ray diffraction (XRD) $\theta - 2\theta$ scans for a-MoGe films. For the thin films, we observe a broad hump around the main peaks between 2θ of 35° to 45° . The peaks coming in the data are those from the substrate used (surface oxidised Si/SiO₂), as they match with the XRD data of the substrate alone. High resolution TEM image on a 20 nm thick film (Fig. 1(b)) shows a uniform and featureless film surface along with diffuse ring patterns for electron diffraction measurement, pointing towards the amorphous nature of the film. Scanning Electron Microscope (SEM) images (Fig 1(c)) point out to a featureless film surface with very low density of particulates. Energy dispersive X-ray (EDX) analysis of the films show the stoichiometric ratio of Mo to Ge in the films to be approximately 3:1.

We observe from Fig. 2 the results of the magneto-transport (R-T) and exclusion of the magnetic field (M-T) experiments for the a-MoGe films. Figs. 2(a) and 2(b) show the temperature variation of the resistance and also the sheet resistance (R_s) with different film thicknesses (t). The films show a weak negative temperature coefficient along with large normal state resistivity (ρ_N) (inset of Fig. 2(d)) point towards the behaviour of a bad metal. Fig 2(b) shows a magnified view of the resistive transition, which

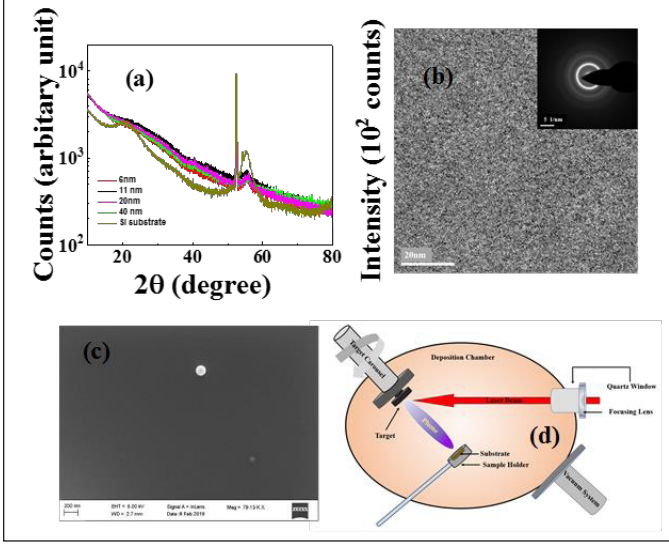


Fig. 1: (a) X-ray diffraction θ - 2θ scans of the a -MoGe films and the Si/SiO₂ substrate (b) High resolution TEM image of 20nm thick film and electron diffraction pattern of the selected area (inset). (c) SEM topographic image of the same film; two particulates are visible within the scan range of the otherwise clean surface. (d) Schematic of the PLD chamber.

are reasonably sharp, indicating a single phase of the films. Fig 2(c) shows the magnetic shielding response measured using a 2-coil mutual inductance setup for thin films. The superconducting transition temperature (T_c), is defined as the temperature where the resistance drops to 0.05% of its value in the normal state (measured at 9 K as a standard) from the resistance vs temperature measurements. While from the 2-coil measurements, it is defined as the temperature where M' drops to 99% of its normal state value. From both these definitions, we get almost the same value of the T_c for a given film. Fig. 2(d) captures the variation of T_c with thickness. For bulk samples (20 nm and of higher thickness) it saturates to about 7.5 K, where with decreasing thickness, we see a systematic reduction to about 6 nm, till which the decrease is relatively gradual, but below it, the T_c decreases drastically to 1.84 K for a film of thickness 2 nm. Figs. 2(e)-(f) show the results of the Hall measurements performed at 25 K. In Fig. 2(e) we plot the dependence of the Hall resistance for different film thicknesses, while Fig. 2(f) shows the variation of carrier density with thickness of the films. It is interesting to note that the type of carriers for the 11 nm, 20 nm and 40 nm are holes, whereas the carrier type for the 3 nm and the 6 nm films are electrons. The carrier density, n was obtained from the Hall coefficient,

$$R_H = \frac{\rho_{xy}}{H}, \text{ using the relation, } n = \frac{1}{eR_H}.$$

Figs. 3(a)-(b) show the magnetic field variation of the resistance of the 3 nm and 20 nm MoGe films, observed at different temperatures, with the magnetic field being

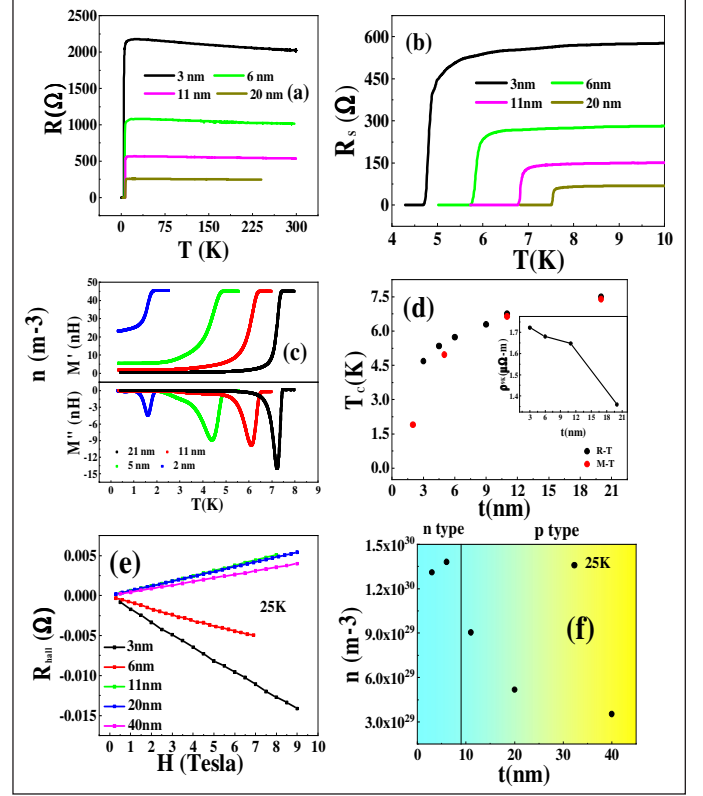


Fig. 2: (a) Variation of resistance for a -MoGe films with different thicknesses. (b) Expanded view of the temperature dependence of sheet resistance (R_s) close to the superconducting transition. R_s at 9K is taken as the normal state sheet resistance. (c) The real and imaginary parts of the magnetic shielding response $M = M' + iM''$, as a function of temperature, for different film thicknesses. (d) Variation of T_c with film thickness (t) as measured from R-T and M-T. Variation of normal state resistivity (ρ^{nk}) with thickness is given in the inset. (e) Hall resistance (R_{xy}) as a function of magnetic field variation for different t , taken at 25K. (f) Carrier density (n), obtained from R_{xy} as a function of t .

applied perpendicular to the film plane. The upper critical field, H_{c2} is defined as the magnetic field, where the resistance reaches 90% of its normal state value. $H_{c2}(0)$ and the Ginzburg-Landau coherence length, $\xi_{GL}(0)$ is then determined using the dirty limit formula [47].

$$H_{c2}(0) = 0.693 * T_c \left(\frac{dH_{c2}}{dT} \right)_{T_c} \text{ and } \xi_{GL}(0) = \left(\frac{\Phi_0}{2\pi H_{c2}} \right)^{1/2} \quad (1)$$

The $H_{c2}(0)$ ranges from ~ 14.8 T for the 20nm film and decreases systematically to 6.9 T for the film of 3nm. The corresponding $\xi_{GL}(0)$ ranges from 4.8-6.9 nm (Fig. 3(d)). Figs 3(e)-(f) shows the variation of the zero-field penetration depth λ^{-2} with temperature, as a function of film thickness and the consequent fitting with the dirty limit BCS expression [48],

$$\frac{\lambda^{-2}(T)}{\lambda^{-2}(0)} = \frac{\Delta(T)}{\Delta(0)} \tanh \left[\frac{\Delta(T)}{2k_B T} \right] \quad (2)$$

using $\Delta(0)$ and $\lambda(0)$ as fit parameters and assuming a BCS temperature variation of $\Delta(T)$). It is interesting to note that $\lambda(0)$ doesn't show appreciable variation with thickness till down to 5 nm. The ratio of the λ , obtained from experiments as $T \rightarrow 0$, to that obtained from the fitting is close to 1 upto 5 nm film thickness, while decreasing rapidly for the 2 nm film, due to combined effects of increasing disorder coupled with quantum and classical phase fluctuations [49].

3.2 a- Re_6Zr thin films

Fig 4(a) shows the x-ray diffraction (XRD) θ - 2θ scans for a- Re_6Zr films. For the thin films, we observe a broad hump around the main peaks between 2θ of 40° to

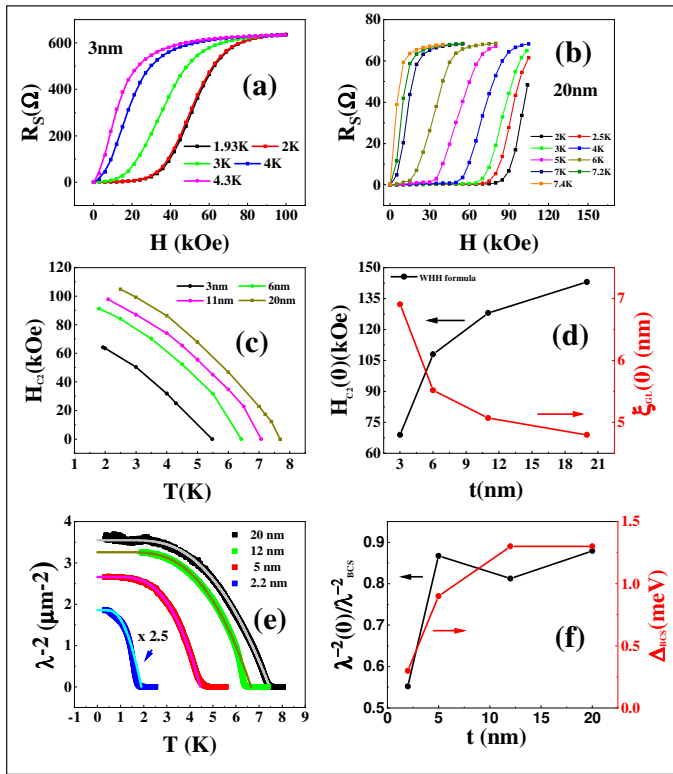


Fig. 3: For a-MoGe variation of R_s with magnetic field for two film thickness, (a) 3 nm and (b) 20 nm. (c) Variation of H_{c2} with temperature, for different film thickness. (d) Variation of $H_{c2}(0)$ and $\xi_{GL}(0)$, (calculated using eqn. 1) with film thickness. (e) Temperature variation of λ^{-2} for films of different thickness; the solid lines are fits with dirty limit BCS expression (eqn.2), (f) variation of $\lambda^{-2}(T \rightarrow 0)/\lambda_{BCS}^{-2}(0)$ and $\Delta_{BCS}(0)$ with different film thickness.

50° . High resolution TEM image on a 40 nm thick film (Fig. 4(b)) shows a uniform and featureless film surface along with diffuse ring patterns for electron diffraction measurement, pointing towards the amorphous nature of the film. AFM measurement shows smooth films with no granularity with a surface roughness of ~ 1 -1.5 nm (Figs. 4(c)-(d)). Energy dispersive X-ray (EDX) analysis of the films show the stoichiometric ratio of Re to Zr in

the films to be approximately 6:1. We perform transport measurements on the a- Re_6Zr thin films, and the results are as follows.

Figs. 5(a)-(b) show the temperature variation of the resistance (sheet resistance for the heating curve 5(b)) with temperature for different film thicknesses. Like a-MoGe, we observe a weak negative temperature coefficient of

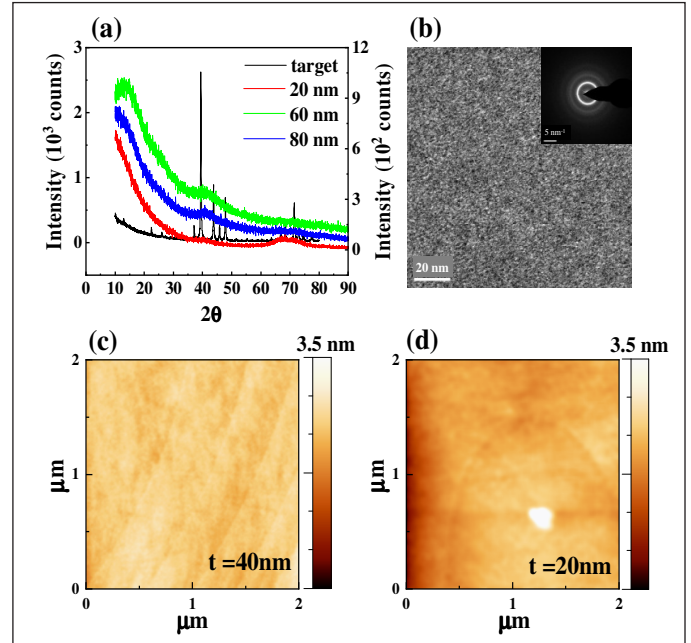


Fig. 4: (a) X-ray diffraction θ - 2θ scans of the Re_6Zr target (left axis) and a- Re_6Zr films (right axis). (b) High resolution TEM image of 40 nm thick film and representative selective area electron diffraction pattern (inset). (c) and (d) AFM topographic image of two a- Re_6Zr films; one particulate can be observed within the field of view in the 20 nm sample.

the resistance coupled with large normal state resistivity $N(\rho)$ from 2-3 $\mu\Omega$ (at 9 K, inset of Fig. 5(d)), pointing to the nature of a bad metal, in the normal state of the superconductor. Fig 5(c) shows the magnetic field screening response with different thickness. Fig 5(d) shows the variation of T_c with thickness. It remains at a constant value of 5.86 K for thicknesses from 120 nm, down to 40 nm (the bulk regime), whereby there is a decrease downwards with decreasing thickness. Down to 8 nm, the decrease in T_c is gradual but for thickness < 8 nm, there is a sharp decrease, with the 3 nm film having a T_c of 2.3 K. In figs. 5(e)-(f) we have the Hall resistance and the carrier density as a function of thickness, measured at 25 K. Unlike the case of a-MoGe, here we don't see a change in the sign of the Hall resistance as we go down with thickness. The sign of Hall resistance is negative for the a- Re_6Zr films, indicating the majority carrier type to be electrons. Following the calculations of Hall coefficient, as done for a-MoGe films, one can estimate the carrier density for the a- Re_6Zr films.

Figs. 6(a)-(b) show the magnetic field variation of R_s for film of thickness 40 nm and 5 nm, measured at different temperatures. One interesting aspect, not shown by the a-MoGe films down to 3 nm, is the crossover of the magnetoresistance curves around 72 kOe for the 5 nm

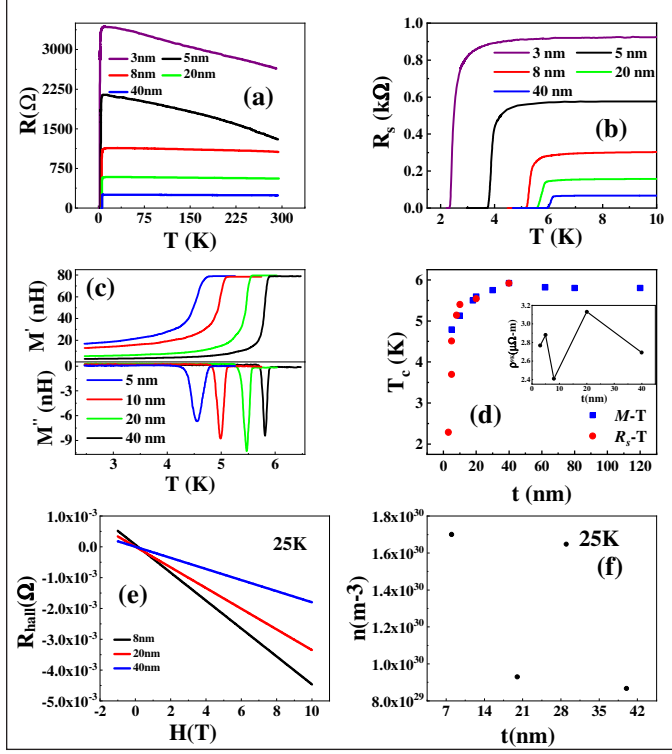


Fig. 5: (a) Variation of resistance for a- Re_0Zr films with different thicknesses. (b) Expanded view of the temperature dependence of sheet resistance (R_s) close to the superconducting transition. R_s at 9 K is taken as the normal state sheet resistance. (c) The real and imaginary parts of the magnetic shielding response $M = M' + iM''$, as a function of temperature, for different film thicknesses. (d) Variation of T_c with film thickness (t) as measured from R - T and M - T . Variation of normal state resistivity (ρ^{9K}) with thickness is given in the inset. (e) Hall resistance (R_{xy}) as a function of magnetic field variation for different t , taken at 25 K. (f) Carrier density (n), obtained from R_{xy} as a function of t .

film. This crossover reflects the weak negative temperature coefficient of resistance in the normal state. Like in the case of a-MoGe, the H_{c2} is defined as the field, where R_s reaches 90% of its normal state value. Fig. 6(c) shows the variation of H_{c2} with temperature, for films of different thickness. We determine $H_{c2}(0)$ and the Ginzburg-Landau coherence length, $\xi_{GL}(0)$ using eq. (1), where $H_{c2}(0) \sim 11$ T for the 40 nm thick film and decreases to 6.5 T at 5 nm. The corresponding $\xi_{GL}(0)$ ranged between 5.5 - 7.1 nm (Fig. 6(d)). Figure 6(e) shows variation of λ^{-2} as a function of temperature for films of different thickness. The data is fitted with the dirty limit BCS expression (eq. (2)) with fit parameters $\Delta(0)$ and $\lambda(0)$ parameters (plotted in Fig. 6(f)) and assuming a BCS temperature variation of $\Delta(T)$. It is interesting to note that

$\lambda(0)$ doesn't show appreciable variation with thickness. Unlike the variation of λ^{-2} for the 2nm a-MoGe film, due to combined effects of disorder and phase fluctuations, we don't see any such signature for the 5nm film.

4. Discussions

We have seen from penetration depth measurements and reports from tunneling experiments [50,51] that

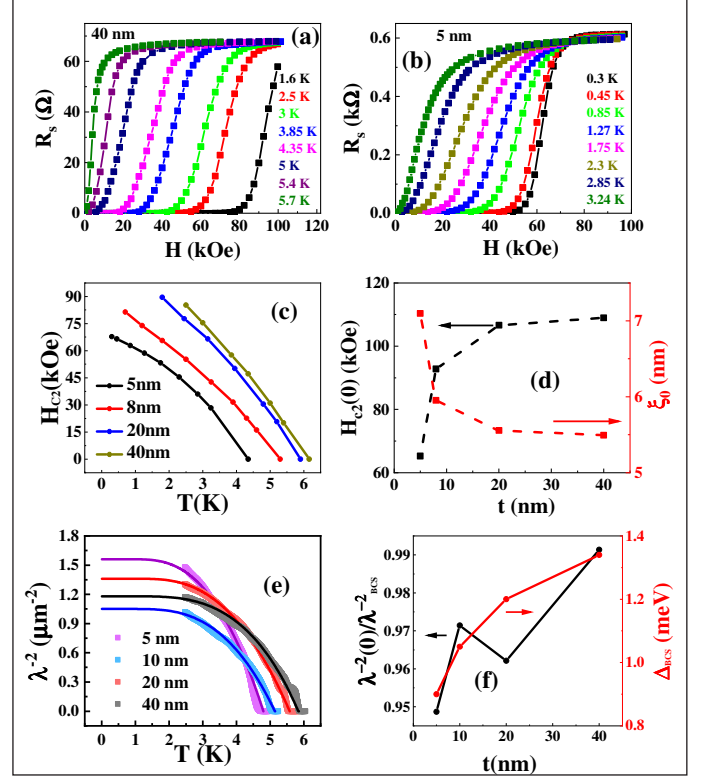


Fig. 6: Variation of R_s Re_0Zr with magnetic field for two film thickness, (a) 40 nm and (b) 5 nm. (c) Variation of H_{c2} with temperature, for different film thickness. (d) Variation of $H_{c2}(0)$ and $\xi_{GL}(0)$, (calculated using eqn. 1) with film thickness. (e) Temperature variation of λ^{-2} for films of different thickness; the solid lines are fits with dirty limit BCS expression (eqn.2). (f) Variation of $\lambda^{-2}(T \rightarrow 0)/\lambda_{BCS}^{-2}(0)$ and $\Delta_{BCS}(0)$ with different film thickness

thin films of both a-MoGe and a- Re_0Zr behave like a BCS superconductor. We now try to find the mechanism for the variation of transition temperature with thickness in the two systems. Following the model of Simonin[52], based on the Ginzburg-Landau theory one gets a description between the correlation of film thickness with T_c , which goes as

$$T_c = T_{Co} \left(1 - \frac{d_c}{d} \right) \quad (3)$$

where T_{Co} is the bulk T_c and d_c is the critical film thickness, below which superconductivity disappears. Using least square fitting method, we obtain for a-MoGe, T_{Co} as 7.82 K and T_c as 1.49 nm as shown in Fig 7(a).

This is in good match with the T_c of the bulk films (20nm and higher), while for the 2nm thick film, T_c goes down to 1.84 K, pointing towards the disappearance of superconductivity as one goes to 2nm and lower. The same analysis, when employed for the a-Re₆Zr films, gives T_{C0} as 6.17 K and T_C as 1.69 nm, shown in Fig 8(a). The bulk films (40 nm-120 nm) all show a T_C of around 5.85 K, while going down in thickness to 3 nm, T_c is reduced to 2.29 K. The thin films of both a-MoGe and a-Re₆Zr both are in the strong disorder limit, as ascertained from the dirty limit BCS fitting of the penetration depth and the mean free path (l) calculation, from the Hall data, using free electron gas relations, as shown in Figs 7(c) and 8(c). The electronic mean free path is given by

$$l = \frac{m v_F}{n \rho_n e^2}, \quad v_F = \frac{\hbar k_F}{m} = \frac{\hbar}{m} (3\pi^2 n)^{1/3} \quad (4)$$

where m is the electron mass, e is the electron charge, and $v_F(k_F)$ is the Fermi velocity (wave-vector). We obtain the electronic mean free path, $l \sim 0.7$ - 1.7 \AA for the a-MoGe films, while for the a-Re₆Zr films, l was more or less a constant around 0.5 \AA (assuming the effective mass of the electron to be the free electron mass). The corresponding value of $k_F l \sim 1$ for both sets of films, suggests that the films are strongly disordered.

Destruction of superconductivity occurs via two different, although not always mutually exclusive, routes. One is the fermionic mechanism[53,16], where with increasing disorder, the effective screening between the two electrons forming a Cooper pair, weakens, with the electron-electron Coulomb repulsion gaining precedence over the phonon mediated pairing, thereby leading to a decrease in the amplitude of the order parameter and hence causing a decrease in T_c . The theory of this effect for thin films was given by Finkelstein, which predicts a correlation between T_c and the sheet resistance R_s given by [16],

$$\frac{T_c}{T_{c0}} = \exp(\gamma) \left(\frac{1-X}{1+X} \right)^{1/\sqrt{2r}}, \quad r = \frac{e^2}{2\pi^2 \hbar} R_s, \quad (5)$$

$$X = \frac{\sqrt{r/2}}{r + \frac{1}{4}}, \quad \gamma = \ln(\hbar/\tau T_{c0} k_B)$$

Here T_{c0} is the limiting value of T_c for large thickness. In Fig. 7(b) and 8(b) we show that we can fit our data with eqn. (5) reasonably well, with $T_{c0} \sim 7.8 \text{ K}$ and $\gamma \approx 8.72$ for the a-MoGe thin films and $T_{c0} \sim 6.5 \text{ K}$ and $\gamma \approx 8$ for the a-Re₆Zr thin films respectively. The value of γ is comparable to that obtained for α -MoSi[25] and a-MoGe [54] films, made from sputtered targets. The second mechanism is the destruction of superconductivity from thermal phase

fluctuations. Quantitatively this is estimated by comparing the values of the superfluid stiffness, J , which is given by (in SI units)[55, 56],

$$J = \frac{\hbar^2 n_s a}{4m}, \quad n_s = \frac{m}{\mu_0 e^2 \lambda^2} \quad (6)$$

where μ_0 is the permeability of vacuum and $a = \min\{t, \xi_{GL}(0)\}$. Phase fluctuations start playing an important role when $J(0) \lesssim \Delta(0)$. It has been shown recently that in a-MoGe films, that there is a crossover from the first mechanism to the second [49] when the thickness becomes $\sim 2 \text{ nm}$ (Fig 7(d)). For the a-Re₆Zr films, down to 5nm, $J(0)$ is larger than $\Delta(0)$ (Fig 8(d)), and therefore we don't expect phase fluctuations to play a dominant role in the destruction of superconductivity. The possibility of the crossover still remains an open question that will have to be addressed in more detail in the future.

Regarding the reversal of the sign of the Hall coefficient, for the a-MoGe films, one possible explanation [58-60] is the hybridization of the s-d orbitals and hence the distortion of the E-k dispersion curve in amorphous transition metals. Weir *et al.* showed that in a transition metal, following some model Hamiltonian, a free electron (s) band hybridizes with tightly bound d-orbitals. As a result, the dispersion curve is distorted into a S shape and depending on the curve where the slope is taken v_F comes out to be positive and negative, thereby making the charge carriers holes or electrons. This leads us to an assertion that the Fermi-level of the a-MoGe system might be thickness or disorder dependent. Dependence of R_H

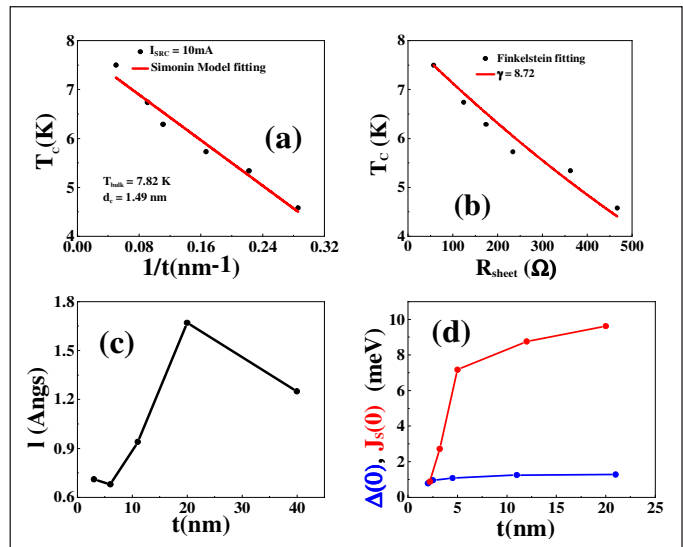


Fig.7: (a) Variation of T_c with $1/t$, for the a-MoGe films and fitting with the Simonin model using eq. 3; (b) Variation of R_s with T_c and fitting with Finkelstein model, following eq. 5. (c) Variation of electronic mean free path (l) with t (using eq. 4); (d) Comparison of $\Delta(0)$ (blue circle) and $J_s(0)$ (red circle) for a-MoGe films of different thickness

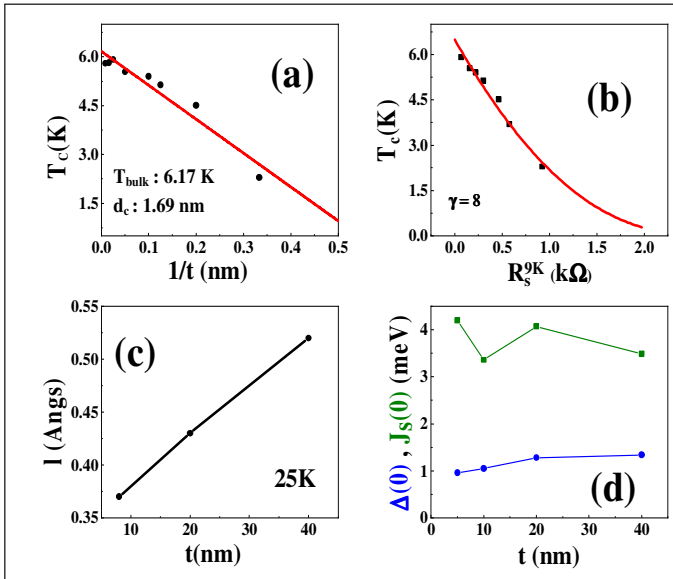


Fig. 8: (a) Variation of T_c with $1/t$, for the a - Re_0Zr films and fitting with the Simonin model using eq. 3; (b) Variation of R_s with T_c and fitting with Finkelstein model, following eq. 5. (c) Variation of electronic mean free path (l) with t (using eq. 4); (d) Comparison of $\Delta(0)$ (blue circle) and $J_s(0)$ (green circle) for a - Re_0Zr films of different thickness.

on thermopower[61] is another factor for sign reversal of the Hall coefficient. Fritsch *et al.* showed that according to the Ziman model, in the expression of the thermopower, a factor called γ defined as $\gamma = \frac{\partial \ln(E_F)}{\partial \ln(V)}$, is related to R_H as $R_H = \frac{\gamma}{|v|} (n|e|)^{-1}$, where V is the volume of the system and n is the carrier density. So, in a sense, dependence of Fermi level on film thickness can be a criterion in our system for the sign reversal.

5. Conclusions

In summary, we have successfully grown thin films of a - MoGe and a - Re_0Zr by pulsed laser deposition and carried out a comprehensive study of the superconducting and structural properties. Measurement of penetration depth and magneto-transport measurements show that both are Type II s-wave superconductors, with upper critical fields for the thick samples exceeding 100 kOe. The ability to grow high quality thin films can have potential applications in the field of superconducting single photon detectors (SNSPDs), where the films can be integrated into advanced optical structures like waveguides and cavities.

References

- David P. Norton, *Pulsed Laser Deposition of Complex Materials: Progress Toward Applications (Pages: 1-31)*, Chapter 1 of Pulsed Laser Deposition of Thin Films: Applications-Led Growth of Functional Materials, Editor(s): Robert Eason (John Wiley & Sons, Inc. 2007).
- J. Shen, Zheng Gai, J. Kirschner, *Growth and magnetism of metallic thin films and multilayers by pulsed-laser deposition*,

- Surface Science Reports **52** (2004) 163-218.
- Douglas H. Lowndes, D.B. Geohegan, A.A. Puretzsky, D.P. Norton, C.M. Rouleau, *Synthesis of Novel Thin-Film Materials by Pulsed Laser Deposition*, Science **273** (1996) 898-903.
- Hans-Ulrich Krebs, O. Bremert, *Pulsed laser deposition of thin metallic alloys*, Appl. Phys. Lett. **62**, 2341 (1993).
- G. Bergmann, *Amorphous Metals and their Superconductivity*, Physics Letters C, **27**, 4(1976), 159-185.
- W. Buckel, R. Hilsch, Z.Physik, **138**, 109, (1954).
- W. Buckel, R. Hilsch, Z.Physik, **146**, 27, (1956).
- M.M. Collver and R.H. Hammond, *Superconductivity in amorphous transition-metal alloy films*, Phys. Rev. Lett. **30**, 92 (1973).
- F.P. Missell, *Amorphous Superconductors*, INIS-BR-2297(V.1), 161-175
- M.M. Collver and R.H. Hammond, *Superconductivity in amorphous transition-metal alloy films*, Phys. Rev. Lett. **30**, 92 (1973).
- W. Liu, M. Kim, G. Sambandamurthy and N. P. Armitage, *Dynamical study of phase fluctuations and their critical slowing down in amorphous superconducting films*, Phys. Rev. B **84**, 024511 (2011).
- T. Proslir, J. A. Klug, J. W. Elam, H. Claus, N. G. Becker and M. J. Pellin, *Atomic layer deposition and superconducting properties of NbSi films*, J. Phys. Chem. C **115**, 9477 (2011).
- I. Shamass, O. Cohen, M. Ovadia, I. Gutman and D. Shahar, *Superconducting correlations in thin films of amorphous indium oxide on the insulating side of the disorder-tuned superconductor-insulator transition*, Phys. Rev. B **85**, 140507(R) (2012).
- M. D. Stewart, A. Yin, J. M. Xu, and J. M. Valles, *Superconducting Pair Correlations in an Amorphous Insulating Nanohoneycomb Film*, Science **318**, 1273 (2007).
- G. Bergmann, *Amorphous metals and their superconductivity*, Phys. Rep. **27**, 159 (1976)
- A.M. Finkel'shtein, *Superconducting transition temperature in amorphous films*, JETP Lett. **45**, 46 (1987).
- A. M. Finkel'shtein, *Suppression of superconductivity in homogeneously disordered systems*, Phys. B **197**, 636 (1994).
- Y. Ivry, C. S. Kim, A. E. Dane, D. De Fazio, A.N. McCaughan, K. A. Sunter, Q. Zhao and K. K. Berggren, *Universal scaling of the critical temperature for thin films near the superconducting-to-insulating transition*, Phys. Rev. B **90**, 214515 (2014).
- P. Spathis, H. Aubin, A. Pourret and K. Behnia, *Nernst effect in the phase-fluctuating superconductor InO_x* , EPL **83**, 57005 (2008).
- S. Okuma, Y. Imamoto, M. Morita, *Vortex Glass Transition and Quantum Vortex Liquid at Low Temperature in a Thick a - $\text{Mo}_x\text{Si}_{1-x}$ Film*, Phys. Rev. Lett. **86**, 3136 (2001).
- P. Berghuis, A. L. F. van der Slot and P. H. Kes, *Dislocation-mediated vortex-lattice melting in thin films of a - Nb_3Ge* , Phys. Rev. Lett. **65**, 2583 (1990).
- I. Guillamon, H. Suderow, A. Fernandez-Pacheco, J. Sese, R. Cordoba, J.M. De Teresa, M.R. Ibarra, S. Vieira, *Direct observation of melting in a two-dimensional superconducting vortex lattice*, Nat. Phys. **5**, 651 (2009).
- F. Marsili, V. B. Verma, J. A. Stern, S. Harrington, A. E. Lita, T. Gerrits, I. Vayshenker, B. Baek, M. D. Shaw, R. P. Mirin and S. W. Nam, *Detecting single infrared photons with 93% system efficiency*, Nat. Photon. **7**, 210 (2013).
- C. M. Natarajan, M. G. Tanner and R. H. Hadfield,

- Superconducting nanowire single-photon detectors: physics and applications*, Supercond. Sci. Technol. **25**, 63001 (2012).
25. A. Banerjee, L. J. Baker, A. Doye, M. Nord, R. M. Heath, K. Erotokritou, D. Bosworth, Z. H. Barber, I. MacLaren and R. H. Hadfield, *Characterisation of amorphous molybdenum silicide (MoSi) superconducting thin films and nanowires*, Supercond. Sci. Technol. **30**, 084010 (2017).
 26. K. Miyahara, M. Mukaida, M. Tokumitsu, S. Kubo and K. Hohkawa, *Abrikosov vortex memory with improved sensitivity and reduced write current levels*, IEEE Trans. Magn. **23**, 875 (1987).
 27. W.R. White, A. Kapitulnik, M.R. Beasley, *Collective vortex motion in a-MoGe superconducting thin films*, Phys. Rev. Lett. **70**, 670 (1993).
 28. A. Yazdani, W.R. White, M.R. Hahn, M. Gabay, M.R. Beasley, A. Kapitulnik, *Observation of Kosterlitz-Thouless-type melting of the disordered vortex lattice in thin films of a-MoGe*, Phys. Rev. Lett. **70**, 505 (1993).
 29. A. Yu. Rusanov, M.B.S. Hesselberth, J. Aarts, *Depairing currents in superconducting films of Nb and amorphous MoGe*, Phys. Rev. B **70**, 024510 (2004).
 30. M.L. Latimer, G.R. Berdiyrov, Z.L. Xiao, W.K. Kwok, F.M. Peeters, *Vortex interaction enhanced saturation number and caging effect in a superconducting film with a honeycomb array of nanoscale holes*, Phys. Rev. B **85**, 012505 (2012).
 31. M.C. Hellerqvist, D. Ephron, W.R. White, M.R. Beasley, A. Kapitulnik, *Vortex Dynamics in Two-Dimensional Amorphous $\text{Mo}_{77}\text{Ge}_{23}$ Films*, Phys. Rev. Lett. **76**, 4022 (1996).
 32. I.W. Boyd, *Thin Film growth by pulsed laser deposition*, Ceramics International, **22**, 5, 429-434, (1996).
 33. F. Gontad, A. Lorusso, L. Solombrino, I. Koutselas, N. Vainos, A. Perrone, *Growth of Niobium Thin Films on Si Substrates by Pulsed Nd:YAG Laser Deposition*, J. Mater. Sci. Technol. **31**, 8, 784-789 (2015).
 34. D. Chrisey (editor), G. Hubler (editor), *Pulsed Laser Deposition of Thin Films*, Wiley-Blackwell (1994).
 35. M. Tinkham, *Introduction to Superconductivity*, Dover Books (2004).
 36. A.A. Abrikosov, *Nobel Lecture: Type-II superconductors and the vortex lattice*, Rev. Mod. Phys. **76**, 975 (2004).
 37. A.A. Abrikosov, *On the Magnetic Properties of Superconductors of the Second Group*, JETP, **5**, 6, 1174 (1957).
 38. V.N. Ryzhov, E.E. Tareyeva, Y.D. Fomin, E.N. Tsiok, *Berezinskii-Kosterlitz-Thouless transition and two-dimensional melting*, Physics-Uspokhi, **60**, 9, 857-885 (2017).
 39. R. P. Singh, A. D. Hillier, B. Mazidian, J. Quintanilla, J. F. Annett, D. McK. Paul, G. Balakrishnan, and M. R. Lees, *Detection of Time-Reversal Symmetry Breaking in the Noncentrosymmetric Superconductor Re_6Zr Using Muon-Spin Spectroscopy*, Phys. Rev. Lett. **112**, 107002 (2014).
 40. S. K. Ghosh, M. Smidman, T. Shang, J. F. Annett, A. D. Hillier, J. Quintanilla and H. Yuan, *Recent progress on superconductors with time-reversal symmetry breaking*, J. Phys.: Condens. Matter **33**, 033001 (2021).
 41. D. A. Mayoh, J. A. T. Barker, R. P. Singh, G. Balakrishnan, D. McK. Paul, and M. R. Lees, *Superconducting and normal-state properties of the noncentrosymmetric superconductor Re_6Zr* , Phys. Rev. B **96**, 064521 (2017).
 42. K. Matano, R. Yatagai, S. Maeda, and G. Zheng, *Full-gap superconductivity in noncentrosymmetric Re_6Zr , $\text{Re}_{27}\text{Zr}_{57}$ and $\text{Re}_{24}\text{Zr}_{57}$* , Phys. Rev. B. **94**, 214513 (2016).
 43. G. M. Pang, Z. Y. Nie, A. Wang, D. Singh, W. Xie, W. B. Jiang, Y. Chen, R. P. Singh, M. Smidman, and H. Q. Yuan, *Fully gapped superconductivity in single crystals of noncentrosymmetric Re_6Zr with broken time-reversal symmetry*, Phys. Rev. B **97**, 224506 (2018).
 44. P. Parab, D. Singh, S. Haram, R. P. Singh and S. Bose, *Point contact Andreev reflection studies of a non-centrosymmetric superconductor Re_6Zr* , Sci. Rep. **9**, 2498 (2019).
 45. C. Kittel, *Introduction to Solid State Physics*, (John Wiley and Sons, Inc.) (2005).
 46. M. Szlawska, D. Kaczorowski, *Single-Crystal Growth of f-Electron Intermetallics in a Tetra-Arc Czochralski Furnace*, Acta Physica Polonica A, **124**, 2, (2013).
 47. N. R. Werthamer, E. Helfland and P. C. Honenberg, *Temperature and Purity Dependence of the Superconducting Critical Field, H_{c2} . III. Electron Spin and Spin-Orbit Effects*, Phys. Rev. **147**, 295 (1966).
 48. M. Tinkham, *Introduction to Superconductivity* (McGrawHill, Singapore, 1996).
 49. S. Mandal, S. Dutta, S. Basistha, I. Roy, J. Jesudasan, V. Bagwe, L. Benfatto, A. Thamizhavel, P. Raychaudhuri, *Destruction of superconductivity through phase fluctuations in ultrathin a-MoGe films*, Phys. Rev. B, **102**, 060501(R) (2020).
 50. I. Roy, S. Dutta, A. N. Roy Choudhury, S. Basistha, I. Maccari, S. Mandal, J. Jesudasan, V. Bagwe, C. Castellani, L. Benfatto and P. Raychaudhuri, *Melting of the Vortex Lattice through Intermediate Hexatic Fluid in a-MoGe Thin Film*, Phys. Rev. Lett. **122**, 047001 (2019).
 51. S. Dutta, V. Bagwe, G. Chaurasiya, A. Thamizhavel, R. Bapat, P. Raychaudhuri, S. Bose, *Superconductivity in amorphous Re_xZr ($x \sim 6$) thin films*, J. Alloys. Compd. **877**, 160258 (2021).
 52. J. Simonin, *Surface term in the superconductive Ginzburg-Landau free energy: Application to thin films*, Phys. Rev. B **33**, 7830(R) (1986).
 53. S. Maekawa, H. Fukuyama, *Localization Effects in Two-Dimensional Superconductors*, J. Phys. Soc. Jpn. **51**, 1380 (1982).
 54. J.M. Graybeal, M.R. Beasley, *Localization and interaction effects in ultrathin amorphous superconducting films*, Phys. Rev. B **29**, 4167(R) (1984).
 55. V.J. Emery, S.A. Kivelson, *Importance of phase fluctuations in superconductors with small superfluid density*, Nature **374**, 434 (1995).
 56. C. Gupta, P. Parab, S. Bose, *Superfluid density from magnetic penetration depth measurements in Nb-Cu 3D nano-composite films*, Sci. Rep. **10**, 18331 (2020).
 57. S.J. Turneaure, E.R. Ulm, T.R. Lemberger, *Numerical modelling of a two-coil apparatus for measuring the magnetic penetration depth in superconducting films and arrays*, J. Appl. Phys. **79**, 4221 (1996).
 58. G.F. Weir, M.A. Howson, B.L. Gallagher, G.J. Morgan, *Hybridization in amorphous metals*, Philos. Mag. B **47**(2), 163-176 (1983).
 59. B.L. Gallagher, D. Greig, M.A. Howson, *The temperature dependence of the Hall coefficient of metallic glasses: further evidence for electron-electron interaction effects*, J. Phys. F: Met. Phys. **14**, L225 (1984).
 60. L. Banyai, A. Aldea, *Theory of the Hall Effect in Disordered Systems: Impurity-Band Conduction*, Phys. Rev. **143**, 652 (1966)
 61. G. Fritsch, W. Dyckhoff, J. Willer, E. Luscher, *Thermopower of some amorphous transition metal-alloys*, Z. Physik. B Cond. Mat. **53**, 191-196 (1983).

	<p>Mr. Somak Basistha is a 5th year Int. PhD. student in the Department of Condensed Matter Physics and Materials Science, TIFR, working under the guidance of Prof. Pratap Raychaudhuri in the Superconductivity Lab. His research involves investigating the electrodynamics of disordered and 2D superconducting thin films. Currently he is working on broadband microwave spectroscopy on amorphous superconducting thin films.</p>
	<p>Mr. Vivas Bagwe is a scientific officer in the Superconductivity Lab, TIFR. He holds a Diploma in Electronics and Radio Engineering from St. Xavier's Technical Institute, Mahim, Mumbai. His research interest revolves around thin film (Re_zr) growth along with growth of single crystals like $NbSe_2$.</p>
	<p>Mr. John Jesudasan is a scientific officer in the Superconductivity Lab, TIFR. He holds a Diploma in Electronic and Radio Engineering from St. Xavier's Technical Institute, Mahim, Mumbai. He specialises in the growth and basic characterization of superconducting thin films like $YbCO$, NbN, $MoGe$ using sputtering, pulsed laser deposition and a plethora of other techniques.</p>
	<p>Mr. Gorakhnath Chaurasiya is a 2nd year Ph.D. student in the University of Mumbai-Department of Atomic Energy Centre for Excellence in Basic Science (UM-DAE CEBS), Mumbai, working under the guidance of Prof. Sangita Bose. His research topic is the study of electro-dynamical response in superconducting thin films.</p>
	<p>Mr. Soumyajit Mandal is a 5th year PhD. student in the Department of Condensed Matter Physics and Materials Science, TIFR, working under the guidance of Prof. Pratap Raychaudhuri in the Superconductivity Lab. His research involves penetration depth measurements and broadband microwave spectroscopy of superconducting thin films at low temperatures.</p>
	<p>Mr. Surajit Dutta is a 5th year Ph.D. student in the Department of Condensed Matter Physics and Materials Science, TIFR, working under the guidance of Prof. Pratap Raychaudhuri in the Superconductivity Lab. His research involves magnetotransport measurements and scanning tunnelling microscopy on superconducting thin films at low temperatures.</p>
	<p>Prof. Pratap Raychaudhuri is the principal investigator of the Superconductivity Lab and a Professor (H) in TIFR. He is the winner of the Shanti Swarup Bhatnagar Prize in 2014, and is an Elected Fellow of the Indian Academy of Science, Bangalore (2015), and a member of the IUPA commission for Low Temperature Physics (C5). His professional interest lies in super-conductivity, magnetism, thin films and low temperature scanning tunnelling microscopy.</p>

Quantum transport under the influence of transverse magnetic field in coaxially-gated carbon nanotube field effect transistor

Tapender Singh¹ and Padmnabh Rai^{1,2,*}

¹Department of Physics & Astronomical Science, Central University of Himachal Pradesh, Dharamshala, Kangra-176206, HP, India

²School of Physical Sciences, UM-DAE Centre for Excellence in Basic Sciences, University of Mumbai, Kalina, Santacruz (E), Mumbai-400098, India

*Corresponding author E-mail: padmnabh.raai@cbs.ac.in

Abstract

Charge carriers transport characteristics of coaxially-gated single-walled carbon nanotube field effect transistors (SWNTFET) have been investigated in presence of transverse magnetic field by simulation using non-equilibrium Green function (NEGF) method. It is found that the shape and position of energy band get modified as a result of strain introduced under application of magnetic field. The band bending at higher magnetic field leads to the band gap reduction, which in-turn transformation of semiconducting carbon nanotube into metallic. The band gap reduction made available sufficient number of density of states, which are responsible for rapid enhancement in thermionic and tunneling current through increased carrier injections in the channel region. The modulation of carrier transport through transverse magnetic field in SWNTFET explores the possibility for usage in next generation photonic and electronic devices.

Key Words: SWNTFET, NEGF, Tunneling Current, Thermionic Current, Quantum Transport

1. Introduction

The quasi-1D symmetrical structure and outstanding electronic properties of semiconducting single-walled carbon nanotube (SWNT) made it a potential material at nanoscale regime [1-3]. Depending on their chirality nanotube can be metallic or semiconducting, therefore different structure having different electronic properties [2]. The lighter weight, smaller size, high aspects ratio, good tensile strength and mechanical properties of carbon nanotube (CNT) made them potentially useful as fillers in different materials (polymers, metallic surfaces and ceramics), transistors, sensors, membranes and capacitors [4-8]. Moreover, SWNT has also been explored in the field of chip-scale plasmonics, such as, launching and detection of surface plasmons polariton on nanoscale plasmonic waveguide [9,10].

The Electronic properties of SWNT can also be tuned by bending, twisting, mechanical distortion and application of magnetic field [11-13]. Since the band gap is inversely proportional to diameter of semiconducting SWNT [2]. The external magnetic field modulates the electronic properties of SWNT by altering the band gap, which is found to be oscillatory function of magnetic field [14]. The magnetic field can be applied either parallel or perpendicular to axis of nanotube and is impacting significantly on the energy band diagram [13-15]. There is band-gap opening in case of metallic SWNT for magnetic field parallel to the axis of nanotube. However, the band gap is found to be suppressed in case of

semiconducting single-walled carbon nanotube (SWNT) for perpendicular field [13-20]. Thus, the conductivity of SWNT can be modulated by magnetic field irrespective of the nature (semiconducting or metallic) of nanotube.

In this work, it has been explored the effect of transverse magnetic field on (17,0) single-walled carbon nanotube field effect transistor (SWNTFET). The carrier transport is discussed by taking in account of quantum effect and is presented in terms of energy position resolved spectrum for both ballistic and non-ballistic transport. The non-ballistic carrier transport is studied by considering the inelastic phonon scattering. The non-equilibrium Green's function (NEGF) method was used to calculate the transport characteristics of SWNTFET, where p_z -orbital based tight binding Hamiltonian (H) was used to describe the interaction between carbon atoms [21].

2. Theory and Simulation

The external magnetic field is considered as a prominent perturbation to influence the transport properties of SWNT. The external magnetic field \vec{B} is expressed in terms of the vector potential as [20].

$$\vec{A} = \left(0, \frac{L\vec{B}}{2\pi} \sin \frac{2\pi x}{L}\right) \quad (1)$$

where, $L = |\vec{C}_h|$ is the circumference of chiral vector. The vector potential modifies the momentum operator in the Hamiltonian as \vec{p} to $(\vec{p} - e\vec{A}/c)$ [19].

$$\gamma(\vec{\sigma} \cdot \vec{k})\Psi(\vec{r}) = \varepsilon\Psi(\vec{r}) \quad (2)$$

where, γ , $\vec{\sigma}$, \vec{k} are the band parameter, Pauli matrices and wave vector respectively [15].

$$\vec{k} = -i\vec{\nabla} + \frac{e}{c\hbar}\vec{A} \quad (3)$$

The ε - k dispersion relation in presence of transverse magnetic field is expressed as [14].

$$\varepsilon(k) = \pm \frac{\Delta}{g_{\delta}(\phi)} [(kR)^2 + \delta^2]^{1/2} \quad (4)$$

where, Δ is the band gap, $\phi = (\pi R^2 B / \phi_0)$ R is the radius of SWNT and $\phi_0 = (h/e)$ is quantum of magnetic flux and $g_{\delta}(\phi) > 1$ (diverges as $\phi \rightarrow \infty$). $g_{\delta}(\phi) = 1 + (36/5)\phi^2 - (396/25)\phi^4 + \dots$, which holds for $\phi \leq 1/4$. At larger field $\phi > 1/4$, the band gap suppresses exponentially by a factor of $g_{1/3}(\phi) = \exp(4\phi)$ [14]. Thus, the band gap gets suppressed in presence of magnetic field by a factor $g_{\delta}(\phi)$. The energy band diagram of SWNT is calculated by self-consistent potential method [22,23]. The density of carriers is determined by using the electron and hole correlation functions, which is expressed in terms of Green's function [22,23].

$$G(E) = [(E + i0^+)I - H - \Sigma_1 - \Sigma_2 - \Sigma_{\text{int}}]^{-1} \quad (5)$$

where, E is the energy, Σ_1, Σ_2 and Σ_{int} are the self-energy interaction matrices for source, drain and scattering interaction. The effect of source and drain contacts on nanotube channel is described by self-energy matrices [23-25]. To study the carrier transport characteristics, SWNT is considered as a channel in coaxial gated device. The integrated current flow from source to drain is determined by the equation [24]

$$I_{DS} = \frac{4e}{h} \int T(E) [f(E - E_{FS}) - f(E - E_{FD})] dE \quad (6)$$

where, e , h and $T(E)$ are the electron charge, Planck constant and transmission coefficient respectively.

The schematic diagram of n-i-n coaxially gated (17,0) SWNTFET structure is shown in Fig. 1. Source and drain doping concentration (N_d) is considered as $8.75 \times 10^8 \text{ m}^{-1}$ (n-i-n device), thickness of oxide layer (t_{ox}) is 3 nm, dielectric constant of material (k) is 16 and length of channel is taken 18 nm for the simulation. The external magnetic field pushes the barrier closer and consequent to change in the band gap of nanotube. The presence of external biasing (either gate or drain) disturbs the equilibrium by pushing the electrons from one end to other (source and drain) and

resulted into net flow of current. Therefore, it is required to understand the impact of magnetic field on energy band diagram of SWNT in presence of external biasing.

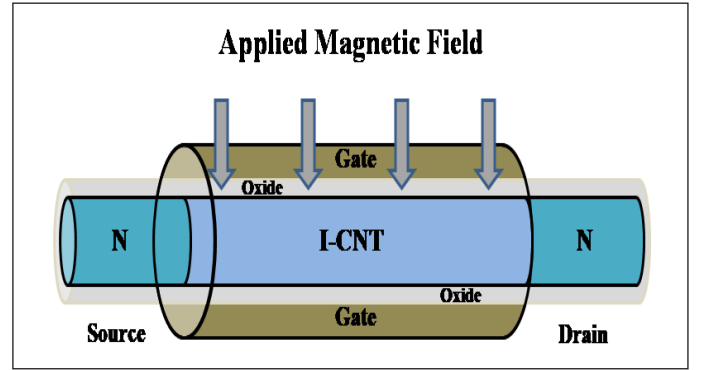


Fig. 1: Schematic diagram of coaxially gated (17,0) SWNTFET for simulation study. The magnetic field direction is shown by solid arrow, which is transverse to nanotube axis.

Band gap reduction and change in shape of band is observed at higher values of transverse external magnetic field. The effect of magnetic field on the energy band diagram of (17,0) CNTFET at different gate voltages is shown in Fig. 2.

3. Results and Discussion

The change in shape and position of band are observed with gate bias (V_{GS}) at different transverse magnetic field. It is found that the sub-band energy shift down with an increase in gate voltage (Fig. 2(a), (d) and (g)). At high gate voltage, the gate field pushes down the sub-bands in channel, which results in lowering the height of potential barrier between source and channel conduction bands [26]. The influence of magnetic field on energy band profile of CNTFET biased at fixed drain (V_{DS}) and gate voltage is presented in Fig. 2(a)-(c) and band gap reduction is observed. The band gap decreases due to perturbation potential introduced by magnetic field. Such coupling of gate potential with perturbation potential deforms the lattice structure of nanotube, which resulted into shape change of conduction and valence bands [27].

At low gate field, there is shift in sub-bands energy with increase in magnetic field. However, there is no significant change in shape of energy bands as depicted in Fig. 2(a)-(c). With increase in gate field, the potential barrier is dropped down and the presence of high magnetic field favored more number of scatterer inside the channel region, which affects the transport of carriers and shapes of bands [28]. The tunneling states inside channel disappeared in the presence of high gate field. Thus, the electrons overcome the top of barrier through thermionic emission (TE) mechanism [29].

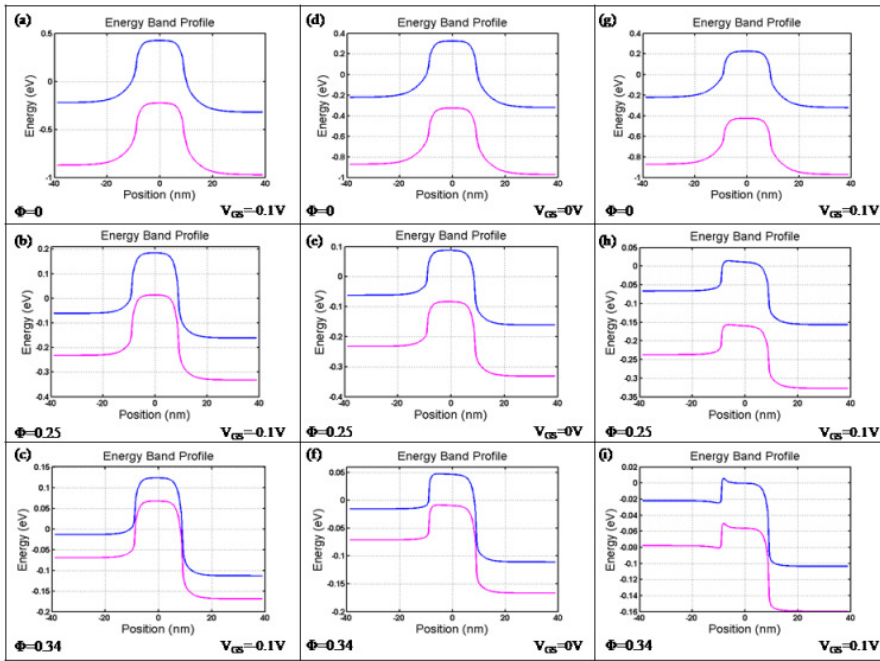


Fig. 2: Plot of first conduction and valence sub-band of (17,0) SWNTFET in presence of transverse magnetic field at $V_{DS} = 0.1V$.

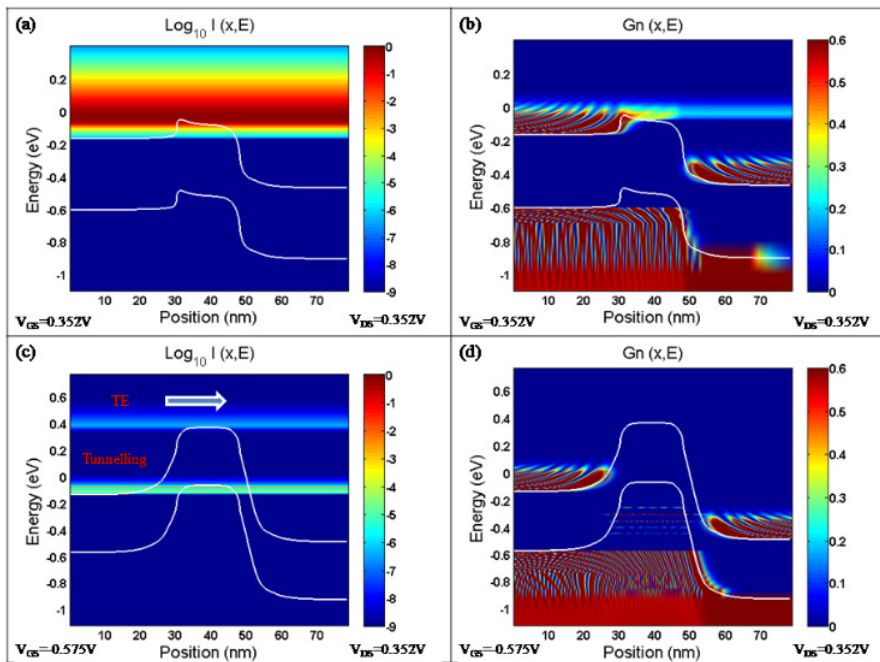


Fig. 3: Energy position resolved current-spectrum and energy-density diagram for (17,0) SWNTFET at (a)-(b) $V_{GS} = 0.352 V$, $V_{DS} = 0.352 V$, (c)-(d) $V_{GS} = -0.575 V$, $V_{DS} = 0.352 V$ and $\phi = 0.25$

The consequence of transverse magnetic field on TE and tunneling current (ballistic) is presented in the Fig. 3(a) and (c), respectively and their respective energy position resolved band diagram is shown in Fig. 3(b) and (d), respectively. A drastic change in TE and tunneling current is observed under external magnetic field. The

TE current starts to appear along with tunneling current for negative gate voltage (Fig. 3(c)). The band gap reductions with increased magnitude of magnetic field push down the potential barrier and therefore provide an opportunity for electron to surpass the barrier. The reduction of threshold voltage, $V_{th} = (E_g / 2e)$ (where, E_g is the band gap of SWNT and $V_{th} = 0.323V$ for biasing condition) due to suppression of band gap leads to more number of electrons injection in channel region [30].

Light brighter line above the top of conduction band (CB) barrier (Fig. 3(b)) represents the flow of electrons from the source to the drain. Influence of magnetic field on electron tunneling current is shown in Fig. 3(c)-(d). It is observed that TE current starts to appear along with tunneling current in the presence of magnetic field. There exists a finite density of states beneath the CB band edge due to the appearance of the tunneling states (formed due to the longitudinal confinement in the effective potential well) and are responsible for tunneling current [28]. This is due to the alignment of source CB with channel valence band (VB) as a consequence of the negative gate biasing in the presence of magnetic field (Fig. 3(d)). Tunneling of electron from source to drain side through these discrete states starts to appear as a tunneling current [28,31,32]. However, band gap reductions at higher values of magnetic field reduced the threshold voltage, which causes the electron concentration to increase. Therefore, few of them (electrons) have a chance to get through the barrier and consequences into appearance of TE current along with tunneling current. Since potential

barrier has noteworthy consequences on performance of the MOSFET-like devices having doped contacts region as a source and drain [31,32]. In Fig. 3, it is noticed that in case of ballistic transport the carrier injected from the source arrive at the drain terminal without losing any energy which is in good agreement with reported values [23,32].

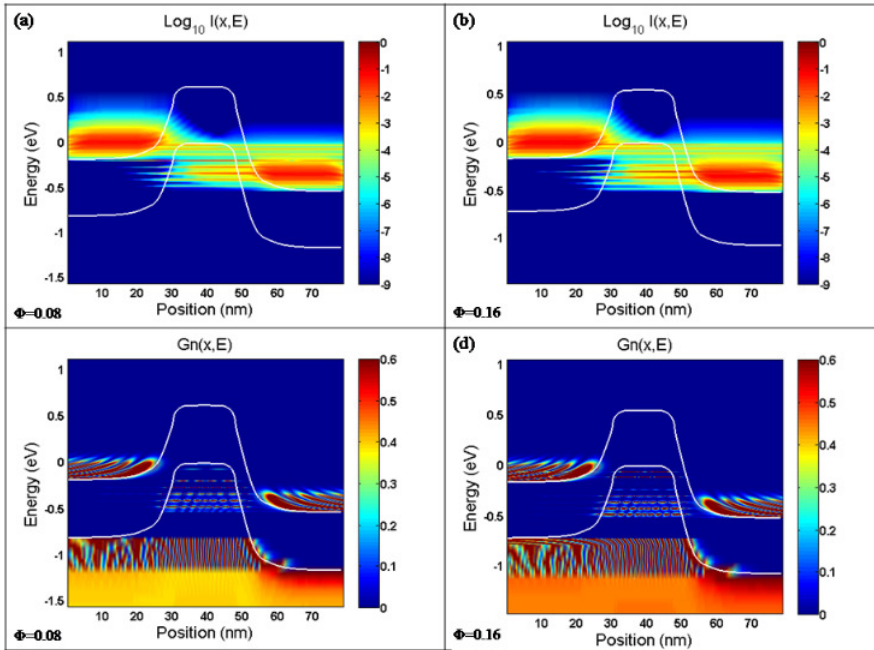


Fig. 4: Energy position resolved (a)-(b) current-spectrum (c)-(d) electron-density profile of (17,0) SWNTFET for $\phi = 0.08$ and $\phi = 0.16$ respectively at $V_{GS} = -0.575$ V, $V_{DS} = 0.352$ V at different magnetic field for non-coherent transport.

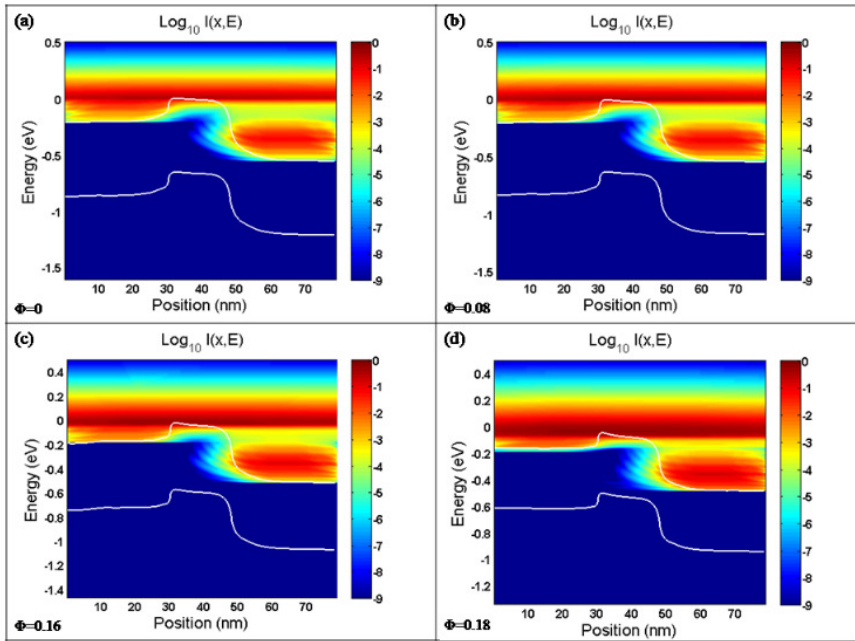


Fig. 5: Energy position resolved current-spectrum of SWNTFET for (a) $\phi = 0$, (b) $\phi = 0.08$, (c) $\phi = 0.16$ and (d) $\phi = 0.18$ at $V_{GS} = 0.352$ V, $V_{DS} = 0.352$ V.

The non-ballistic (dissipative) carrier transport is studied by modifying the respective source and drain self-energy matrices [23,24,28]. Since scattering have significant importance on transport properties of SWNT [23,28]. The effect of scattering is studied by considering electron-phonon interaction as a prominent perturbation in the Hamiltonian term [23]. The energy position resolved

tunneling current spectrum is shown in Fig. 4 (a) and 4 (b) and their respective electron density profile is presented in Fig. 4 (c) and 4 (d) under different magnetic field.

It is observed that tunneling is the dominant mechanism of carrier transport in non-coherent transport (Fig. 4). The electrons tunnel from source to drain through the tunneling sites inside the channel [21,28]. The interrupted (half line) line below the source CB (Fig. 4 (a) and (b)) represents the fraction of electrons which travels via emitting a phonon of corresponding energy and continuous line represent the number of electrons which tunnel through the discrete quantized states without losing its energy [28]. Increase in the number of phonon emission line is observed for higher value of magnetic field ($\phi = 0.16$) (Fig. 4(b)).

Influence of magnetic field on TE current in presence of magnetic field is shown in Fig. 5 and their respective electron-density profile is displayed in Fig. 6. It is observed that there is a rapid increase in TE current with rise in magnetic field (Fig. 5(a)-(d)).

The reduction of threshold voltage pushes more number of electrons above the potential barrier and results in an increase of TE current (Fig.5). A half thick line (along the drain) below TE current represents those numbers of carriers which relax to low lying energy level after phonon emission [33]. Because some of the electrons do not have enough energy to reflect back due to increased strength of scattering, therefore they tends to occupy the low lying energy level along the drain side [28,33]. It is observed that there is large

number of carrier relaxation at higher value of magnetic field (Fig. 5(d)). A small bright line is observed above the top of channel, because sufficient amount of carriers are not able to pass the potential barrier at $\phi = 0$ (Fig. 6 (a)). The increased strength of magnetic field causes the VB and CB come closer, which result in thickening of the electron transport line (Fig. 6(d)) due to excitation of more number

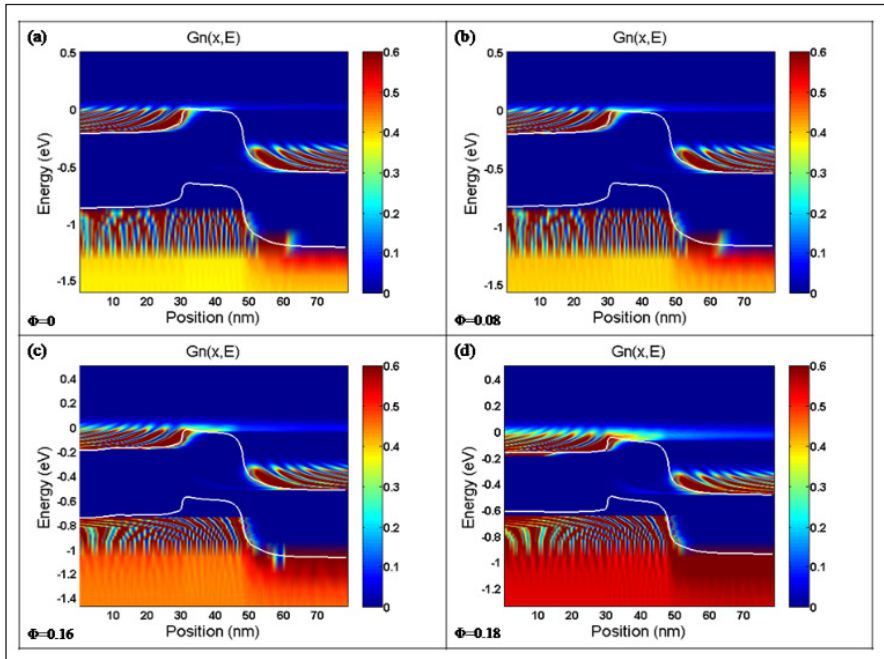


Fig. 6: Energy position resolved electron-density spectrum for (a) $\phi = 0$, (b) $\phi = 0.08$, (c) $\phi = 0.16$ and (d) $\phi = 0.18$ at $V_{GS} = 0.352$ V and $V_{DS} = 0.352$ V.

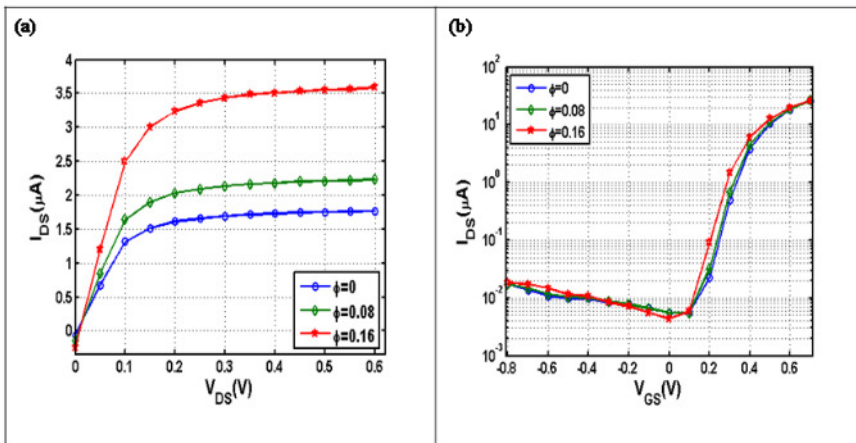


Fig. 7: (a) Output characteristics at $V_{GS} = 0.352$ V and (b) Transfer characteristics at $V_{DS} = 0.352$ V of (17,0) SWNTFET device in presence of magnetic field.

of charge carriers.

The effect of scattering reduces the current by emitting the phonon of corresponding energy [28,33]. Some of the electrons tunnel without losing the energy but few of them having chance to reflect back due to the increased number of collision inside the channel. Thus the occurrence of larger number of scattering event results in decrease of drain current [28].

Impact of magnetic field on output and transfer characteristics of n-i-n SWNTFET device is shown in Fig. 7. Increase in drain current is observed in output and transfer characteristics at higher magnitude of magnetic field. The

band gap reduction (in presence of magnetic field) causes more number of states to be occupied in (fs-fd) region above the top of barrier, which leads to increase in drain current in the presence of magnetic field (Fig. 7(a)) [32]. The drain current first increases with V_{DS} and then get saturated at higher drain biasing. However, a small change in drain current is observed at positive gate voltage region in case of transfer characteristics under influence of magnetic field (Fig. 7(b)). It is noticed that drain current represent an enhancement with increasing V_{GS} and get diminished at $V_{GS} = 0$ V, further, there is advancement in it due to the involvement of tunneling conduction mechanism at negative gate biasing region.

4. Conclusion

In conclusion, the influence of magnetic field on ballistic and non-ballistic carrier transport of (17,0) SWNTFET n-i-n device is studied by NEGF method. The device characteristic was altered by external magnetic field. The band gap reduction was the dominant factor to influence the transport properties under transverse magnetic field. The shift in bands position and shape change has been observed due to the gate potential coupling with perturbation potential introduced by an applied magnetic field. Increase

in TE and tunneling current is observed with increased strength of the magnetic field. It was observed that magnetic field pushes down the barrier which result in the formation of tunneling sites inside the channel region, causing tunneling current to increase and also enhances the TE current. Due to participation of more number of density of states there is increases in the drain current for both output and transfer characteristics. More number of carrier relaxations (TE) is seen with increased strength of magnetic field. Therefore, a large number of carriers get accumulated towards the drain side representing the large number of phonon emissions with increased strength of the magnetic field.

References

1. P. Avouris, Z. Chen, V. Perebeinos, Nat. Nanotechnol. 2 (2007) 605.
2. P. R. Bandaru, J. Nanosci. Nanotechnol. 7 (2007) 1239.
3. P. Avouris, M. Freitag, V. Perebeinos, Nat. Photonics 2 (2008) 341.
4. C. Laurent, E. Flahaut, A. Peigney, Carbon 48 (2010) 2994.
5. J. P. Salvetat, J. M. Bonard, N. H. Thomson, A. J. Kulik, L. Forro, W. Benoit, L. Zuppiroli, Appl. Phys. A 69 (1999) 255.
6. F. Li, H. M. Cheng, S. Bai, G. Su, Appl. Phys. Lett. 77 (2000) 316.
7. K. S. Ibrahim, Carbon Lett. 14 (2013) 131.
8. T. Singh, P. Rai, Mater. Res. Express 6 (2019) 116216.
9. P. Rai, N. Hartmann, J. Berthelot, J. Arocas, G. C. desFrancs, A. Hartschuh, A. Bouhelier, A. Bouhelierv, Phys. Rev. Lett. 111 (2013) 026804.
10. J. Berthelot, G. Bachelier, M. Song, P. Rai, G. C. Francs, A. Dereux, A. Bouhelier, Opt. Express 20 (2012) 10498.
11. A. Rochefort, P. Avouris, Phys. Rev. B 60 (1999) 13824.
12. X. Zhou, H. Chen, O. Y. Zhongcan, H. Chen, O. Y. Zhong-can, J. Phys. Condens. Matter 13 (2001) L635.
13. J. C. Charlier, X. Blasé, S. Roche, Rev. Mod. Phys. 79 (2007) 677.
14. H. W. Lee, D. S. Novikov, Phys. Rev. B 68 (2003) 155402.
15. H. Ajiki, T. Ando, J. Phys. Soc. Japan 62 (1993) 1255.
16. H. Ajiki, T. Ando, J. Phys. Soc. Japan 65 (1996) 505.
17. J. Jiang, J. Dong, D. Y. Xing, Phys. Rev. B 62 (2000) 13209.
18. S. Roche, G. Dresselhaus, M. S. Dresselhaus, R. Saito, Phys. Rev. B 62 (2000) 16092.
19. H. Ajiki, T. Ando, J. Phys. Soc. Japan 62 (1993) 2470.
20. R. Saito, G. Dresselhaus, M. S. Dresselhaus, Phys. Rev. B 50 (1994) 14698.
21. J. Guo, S. Datta, M. Lundstrom, Int. J. Multiscale Comput. Eng. 2 (2004) 257.
22. M. R. Aziziyan, V. Ahmadi, N. Moghadam, Appl. Phys. Lett. 100 (2012) 05111.
23. M. P. Anantram, M. Lundstrom, D. E. Nikonov, Proc. IEEE 96 (2008) 1511.
24. S. Datta, *Quantum Transport: Atom to Transistor*, Cambridge University Press, (2005).
25. J. Guo, M. Lundstrom, S. Datta, Appl. Phys. Lett. 80 (2002) 3192.
26. S. G. Shirazi, S. Mirzakuchaki, Appl. Phys. A 113 (2013) 447.
27. M. Lundstrom, *Fundamentals of Carrier Transport*, Cambridge University Press, (2009).
28. S. O. Koswatta, M. S. Lundstrom, M. P. Anantram, D. E. Nikonov, Appl. Phys. Lett. 87 (2005) 253107.
29. F. R. Pierret and W. N. Gerold, *Advanced Semiconductor Fundamentals*, Reading MA: Addison-Wesley 6 (1987).
30. S. K. Sinha, S. Chaudhury, Mater. Sci. Semicond. Process. 31 (2015) 43.
31. T. Singh, O. S. K. S. Sastri, P. Rai, AIP Adv. 8 (2018) 115214.
32. S. G. Shirazi, G. Karimi, S. Mirzakuchaki, ECS J. Solid State Sci. Technol. 5 (2016) M44.
33. S. O. Koswatta, S. Hasan, M. S. Lundstrom, IEEE Transact. Elect. Dev. 54 (2007) 2339.



Dr. Tapender Singh received B.Sc. degree in Science from Himachal Pradesh University, Shimla, India, in 2012. M.Sc. degree in condensed matter Physics from Central University of Himachal Pradesh, Dharamshala, India, in 2014. He has completed his Ph.D. degree from Central University of Himachal Pradesh, Dharamshala, India, in July 2020 and his research interests include nano-scale device simulations.



Dr. Padmnabh Rai is a Reader (F) in School of Physical Sciences at UM-DAE Centre for Excellence in Basic Sciences, Mumbai-400098 since March 2018. He received his M. Tech. and Ph. D. degree in Condensed Matter Physics from IIT Delhi in 2004 and IIT Bombay in 2009, respectively. Dr. Rai has served as an Assistant Professor (UGC) in Department Physics and Astronomical Sciences at Central University of Himachal Pradesh (HP) during July 2014 to March 2018. He has worked as postdoctoral fellow at National University Singapore, Singapore (December 2013 – May 2014), University of Bourgogne, France (October 2010 – September 2013) and Sunkyunkwan University, South Korea (October 2009 – August 2010). He was Research and Development manager in Diamond Division of Nozomi Technotron Pvt. Ltd., Singapore (January 2009 – August 2009). Dr. Rai is experienced in synthesizing carbon based materials (single crystal diamond, carbon nanotube and graphene). Carbon-based materials are being explored for photonics and plasmonics applications. Dr. Rai is also involved in teaching physics courses at graduate and undergraduate level. He has consulted industries to develop laboratory for growing single crystal diamond for gem and scientific applications. He has more than 35 research publications in international peer reviewed journals and books and 02 patents.

SOCIETY FOR MATERIALS CHEMISTRY (SMC)
(Reg. No. - Maharashtra, Mumbai/1229/2008/GBBSD)
c/o Chemistry Division
Bhabha Atomic Research Centre, Mumbai 400 085

APPLICATION FOR MEMBERSHIP

Please enroll me as a Life member of the *Society for Materials Chemistry (SMC)*. My particulars are as follows:

Name : _____

Educational Qualifications : _____

Field of Specialization : _____

Official Address : _____

Telephone No. (Off.) : _____

Residential Address : _____

Telephone No. (Res.) : _____

Address for Correspondence : Home/Office (Please tick one of the options)

E-mail Address : _____

Subscription Details

Mode of Payment : Cheque/DD/Cash
(Cheque/DD should be drawn in favor of "*Society for Materials Chemistry*" for Rs. 1000/- payable at Mumbai. For out-station *non-multi-city* cheques, please include Rs.50/- as additional charge for bank clearance.

Number :

Dated :

Drawn on Bank & Branch :

Amount :

Place:

Date:

Signature

Registration Number: _____

(To be allotted by SMC office)

Printed by:

Ebenezer Printing House

Unit No. 5 & 11, 2nd Floor, Hind Service Industries

Veer Savarkar Marg, Shivaji Park Sea-Face, Dadar (W), Mumbai - 400 028

Tel.: 2446 2632 / 2446 3872 Tel Fax: 2444 9765 E-mail: outworkeph@gmail.com

In this issue

Feature Articles		Page No.
1.	Recent advancements on graphene thin films <i>Monika Moun and Goutam Sheet</i>	121
2.	A Short Review on Corrosion Resistant Graphene Coating developed by Electrophoretic deposition technique <i>Swarnima Singh, Laxmidhar Besra, Bimal Prasad Singh, Sriparna Chatterjee</i>	130
3.	A Journey from Carbon Atom to Nanocrystalline Diamond <i>Jitendra Nuwad, Dheeraj Jain and V. Sudarsan</i>	138
4.	Growth and Characterization of amorphous Molybdenum Germanium (a-MoGe) and amorphous Rhenium Zirconium (a-Re₆Zr) superconducting thin films using Pulsed Laser Deposition (PLD) technique <i>Somak Basistha, Vivas Bagwe, John Jesudasan, Gorakhnath Chaurasiya, Soumyajit Mandal, Surajit Dutta, Pratap Raychaudhuri</i>	150
5.	Quantum transport under the influence of transverse magnetic field in coaxially-gated carbon nanotube field effect transistor <i>Tapender Singh and Padmnabh Rai</i>	160

Published by
Society for Materials Chemistry
C/o. Chemistry Division
Bhabha Atomic Research Centre, Trombay, Mumbai 40085
e-mail: socmatchem@gmail.com, Tel: 91-22-25592001